

Mineralogy of 100- μ g Powder Test Samples II: Evolved Procedures for the Initial Analysis of Regolith Materials of the Asteroid Itokawa

By

Tomoki NAKAMURA¹, Takaaki NOGUCHI², and Masahiko TANAKA³

Abstract: Applying a combined analytical method specialized for cosmic-dust research, we have characterized mineralogy of individual mineral particles in 2A and 2B powder test samples that were prepared for the second analysis competition of the Hayabusa mission. Thirty-eight mineral particles mostly less than 300 μ m in diameter and ten fine-grained mineral aggregates less than 200 μ m in diameter were picked out from the test samples. Individual samples were X-rayed using synchrotron radiation to have powder X-ray diffraction patterns for identification of constituent minerals. The relative abundances of major constituent minerals in individual samples were determined by applying the Rietveld refinement to diffraction patterns. The X-rayed samples were polished and analyzed by a scanning electron microscope (SEM) for imaging and an electron-probe microanalyzer (EPMA) for quantitative concentrations of thirteen elements. Finally, ten selected samples were thinned by ultramicrotomy, argon ion bombardment, or focused ion beam (FIB) method for detailed mineralogical characterization by transmission electron microscopy (TEM). Small plagioclase compositions are determined by analytical electron microscopy (AEM) using a cold sample stage. The bulk mineralogy, chemical composition, and nano-scale textures were all obtained from a single small particles less than 300 μ m and the total mass of each test sample we used for the present study was only 100 μ g. Therefore, we can accomplish complete mineral characterization using very small quantity of regolith materials of the asteroid Itokawa, when the initial analysis of the returned samples is undertaken.

The results showed that 2A powder sample consists mainly of olivine ($\text{Fa}_{15.1 \pm 0.6}$ on an average), low-Ca pyroxene ($\text{Fs}_{13.9 \pm 0.7}$ on an average), plagioclase, troilite, and kamacite with minor amounts of high-Ca pyroxene, taenite, chromite, Ca-phosphate, and alkali feldspar. The compositions and compositional variations of silicates and the minor element abundances in FeNi metals indicate that the 2A sample bears a close resemblance to H chondrites with petrologic type 4 to 5. Fe/Mg ratios of both olivine and low-Ca pyroxene in the 2A sample correspond to the lowest-end of Fe/Mg variation for H chondrites, suggesting that it is a sample of most reduced type of H chondrites. In addition, the 2A samples contain small amounts of artificial contamination such as quartz-calcite composites, Ni-free Mn-bearing iron metals, and carbonaceous particles like epoxy resin. These particles probably got mixed during preparation of the 2A sample powder from a meteorite. The 2B sample is coarse particles that are composed mainly of metallic phases such as kamacite. Olivine and low-Ca pyroxene are also contained, but metal/silicate ratio of the 2B test sample is apparently higher than that of the 2A test sample. However, Mg/Fe ratios of silicate ($\text{Fa}_{15.8 \pm 0.5}$ and $\text{Fs}_{14.4 \pm 0.7}$ on an average) and the presence of well-defined chondrules suggest that the 2B sample is also similar to H chondrites with petrologic type 4 to 5. All mineralogical characteristics, except for the mode of occurrence of FeNi metals, are very similar between 2A and 2B test samples. This may indicate that the two test samples were prepared from the same meteorite. The high metal/silicate ratio of the 2B test sample is therefore artifact, most probably the

1 Department of Earth and Planetary Sciences, Faculty of Sciences, Kyushu University, Hakozaki, Fukuoka 812-8581, Japan

2 Department of Materials and Biological Sciences, Ibaraki University, Bunkyo 2-1-1, Mito, Ibaraki 310-8512, Japan

3 WEBRAM, National Institute for Materials Science, SPring-8, Kouto Mikazuki-cho 1-1-1, Sayo-gun, Hyogo 679-5198, Japan

results of mechanical separation of magnetic components from a powder of an H chondrite.

1. INTRODUCTION

Surface materials of the asteroid Itokawa will be collected in 2005 and recovered to the Earth in the summer of 2007, only two years ahead from the present. The recovered samples will be powders consisting of particles ranging in size from submicron to submillimeter, analogous to cosmic dust and fine-grained constituents of brecciated regolith meteorites. Characterization of fine particles is extremely difficult and differs completely from that of coarse-grained crystalline meteorites. In addition, individual particles on the asteroidal regolith are not always fragments of the host asteroid, because many particles from other asteroids and comets are deposited there, as is commonly observed in many meteorites from the asteroidal regolith. Ultimately, individual particles in the powder regolith samples are different in origin. Therefore, the powder regolith samples need to be characterized on particle-basis, like characterization of cosmic dust such as micrometeorites and interplanetary dust particles. According to above principles of characterization, we set goals of the mineralogical investigation of the powder regolith samples: (1) evaluation of basic mineralogy of the host asteroid, and (2) identification of foreign particles coming from other planetary bodies. In the present paper, we have characterized powder test samples 2A and 2B to uncover these two essential properties.

As we claimed in the previous report (Nakamura and Noguchi, 2003), the amounts of the test samples allocated to us were very large, which is never expected for the initial characterization of the true sample recovered from the asteroid Itokawa. The most important point we think for the initial characterization is to characterize mineralogy using minimum quantity of the samples. From this viewpoint, only small amounts of test samples, less than 100 μg of each test sample, were used for our characterization and most parts of the samples were left unprocessed. Thus, the remaining samples can be provided for other scientific purposes. Our mineralogical techniques applied in the present investigation are those developed mainly for characterization of Antarctic micrometeorites (Nakamura et al., 1999; 2001a; 2001b; 2003; Noguchi and Nakamura, 2000; Noguchi et al., 2002; Nakashima et al., 2003). A main protocol of the analysis for a single particle consists of synchrotron X-ray diffraction technique for bulk mineralogy and transmission electron microscopy for detailed mineralogy.

2. SAMPLES AND EXPERIMENTAL PROCEDURES

2.1. Sample selection and preparation

2A test sample is a powder, consisting of a variety of minerals and mineral composites ranging in size from submicron to 300 μm . We have picked out twenty eight single particles from 50 to 300 μm in diameter showing different optical characteristics under a high-resolution stereomicroscope. These coarse particles are referred hereafter as 2AC1 to 2AC28. For very fine particles, we gathered them using a small amount of acetone-soluble resin on the top of a thin glass fiber to make a fine-grained mineral aggregate. Ten aggregates were prepared from the 2A test sample and referred hereafter as 2AF1 to 2AF10.

2B test sample is also a powder but consists of relatively coarse particles ranging from 100 to 800 μm in diameter. We selected 10 particles showing different optical characteristics and hereafter refer them as 2BC1 to 2BC10. Analyses of multiple disciplines were performed on these 48 particles, 38 from the 2A sample and 10 from the 2B sample, and the experimental procedures for each sample particle are summarized in Table 1.

2.2. Synchrotron X-ray diffraction analysis

Synchrotron radiation was applied for X-ray diffraction analysis of individual sample particles, because strong synchrotron X-rays, whose intensity is higher at least three orders of magnitudes than that of a normal X-ray generator, induce strong diffractions from small minerals in a sample particle. The experiment was performed at the beam line 3A of the Photon Factory, High energy accelerator research organization, Tsukuba, Japan. A gandolfi X-ray camera, which can obtain a powder X-ray pattern from a single mineral particle with diameters from 5 to 500 μm , was used for the analysis. The synchrotron X-ray was monochromated to

Table 1: Experimental procedures for each sample particle

	SR-XRD*	Rietveld analysis	OP [#]	SEM	EPMA	TEM	TEM	sample preparation
2AC1 ~ 2AC26	○		○	○	○			
2AC26	○		○	○	○			
2AC27 ~ 2AC28	○		○					
2AF1 ~ 2AF5	○	○	○			○		ultramicrotomy
2AF5 ~ 2AF10	○	○	○	○	○			
2BC1 ~ 2BC5	○		○	○	○			
2BC6 ~ 2BC7	○		○	○	○	○		Ar bombardment
2BC8 ~ 2BC9			○	○	○	○		Ar bombardment
2BC10			○			○		FIB

* synchrotron X-ray diffraction
optical microscope

2.161 +/- 0.002 Å using a monochromator and focused at the sample particle in the gandolfi camera using a focusing mirror. The wavelength of X-ray was precisely determined from a diffraction pattern of a standard Si particle. The monochromated X-ray gives sharp X-ray reflection peaks with very low background level. Each sample particle was mounted on a thin glass fiber with 5 µm in diameter with a very small amount of glue and exposed to synchrotron X-ray for 10 to 40 minutes, depending on the size of the particle.

The diffracted X-rays from samples are recorded on a high-resolution imaging plate (IP) set in the gandolfi camera. IP has a wide dynamic range of recordable X-ray intensity compared with films and shows a better linearity between X-ray intensity and blackness on the IP. We had used films in the previous report (Nakamura and Noguchi, 2003), but in the present report we successfully utilizes IP. After exposure to X-ray, IP was scanned by an IP reader BAS 2500 with angle resolution of 0.05°. The read data were converted to diffraction patterns and analyzed for integrated intensities and peak center positions of diffractions using an original software GanCon2 that we have developed.

2.3 Rietveld analysis

The relative abundances of the major four crystalline minerals, olivine, low-Ca pyroxene, plagioclase and troilite, in 2AF1 to 2AF10 samples were obtained through the Rietveld quantitative phase analysis of the powder X-ray diffraction data. In the multi-phase Rietveld refinement, the scale factors are in proportion to the amount of included crystalline phases. And the mass weight ratio is calculated from a following formula,

$$x_n = (s_n Z_n M_n V_n) / (\sum_i s_i Z_i M_i V_i)$$

Where x is the mass weight ratio, s is the scale factor, Z is the chemical number, M is the molecular weight and V is the unit cell volume. The mass weight ratio is determined by evaluation of s values with Rietveld method. The Rietveld structure refinement program, PFLS (Toraya, 1998), was used for Rietveld analysis and this program carries out the quantitative phase analysis, above-mentioned method, as structure refinements. In principle, when quantitative phase analysis by Rietveld method is carried out, all of the component minerals in the sample should be included in calculation. But in this analysis the minor minerals, such as kamacite or taenite, were neglected. Because the amounts of these minerals are little and if these minerals were included in refinement calculation, the refinement cycles had not been convergence and solutions could not be obtained. Starting crystal structure models for each mineral were obtained from references (Morimoto and Guven, 1970, Prewitt et al., 1976, Tokonami et al., 1972, Birle et al., 1968). Isotropic temperature factors, which were also adopted from the same references, were used and the values were fixed through out the refinements. The chemical compositions determined by EPMA analysis were used and these values also fixed through out refinements. The chemical compositions of each crystalline phase were assumed to be homogeneous. As concerns olivine, pyroxene and plagioclase, the scale factors, the lattice constants, the atomic positions and the peak profile parameters were refined. But in troilite case, the scale factor was only refined. The Rietveld least square cycles were also hard to

converge, when atomic or peak profile parameters of troilite were included in calculation because of the insufficiency of observed diffraction peaks. Absorption correction was carried out using the estimated absorption coefficient from that of olivine, which is the major component of these samples. The magnitude of errors is considered to be several percents because of the many assumptions such as neglect of minor minerals, neglect of variation of chemical composition of each mineral phase, use of estimated absorption coefficient and neglect of difference of crystal quality of each mineral phase and so on.

2.4. EPMA analysis

The X-rayed sample particles were embedded in a small amount of epoxy resin and polished using the micro-diamond paste, and analyzed by an EPMA (JEOL JXA-733 superprobe) equipped with a wave-length-dispersive X-ray spectrometer (WDS). WDS quantitative analyses were performed at 15 kV accelerating voltage and 10 nA beam current with a focused beam 2 μm in diameter. Quantitative chemical compositions of oxides SiO_2 , TiO_2 , Al_2O_3 , FeO , MnO , MgO , CaO , NaO , K_2O , Cr_2O_3 , NiO , P_2O_5 , and SO_3 for silicates and elements Ni, Fe, Mn, Co, Cr, S, and P for sulfides and metals were obtained via the ZAF correction method. Special care was taken for the analysis of FeNi metals. In the analysis of FeNi metals, Co concentrations were obtained through correction of Fe-K β contribution on Co-K α . The X-ray energy of Fe-K β is very close to that of Co-K α , therefore the contribution from Fe-K β need to be corrected especially for the minerals rich in Fe such as FeNi metals. We analyzed pure Fe metal and found that the contribution of Fe-K β from 100% Fe on Co abundance is 0.15 wt%. We corrected Co concentrations of FeNi metals in both 2A and 2B test samples according to the Fe content in the metals.

2.5. TEM observation

2.5.1. Sample preparation

Subsequent to X-ray diffraction analysis, selected samples were processed to have thin plates for TEM observation. Three methods for thinning were applied, ultramicrotomy, Ar ion bombardment, and focused Ga ion beam sputtering (Table 1). The former was applied for fine-grained samples of 2AF1 to 2AF5. The latter two methods were applied for metal-rich coarse 2B samples, 2BC6, 2BC7, 2BC8, 2BC9, and 2BC10.

Ultramicrotomy: A sample made of fine-grained mineral fragments bounded of acetone soluble resin were disaggregated on one sharp end of a rod made of consolidated EMBED 812 epoxy resin by a small drop of acetone. After disaggregation of the fine-grained fragments, the fragments were covered by a small drop of epoxy resin. The sample was cured at 70 $^{\circ}\text{C}$ for 48 hrs. Embedding was performed in a clean bench (class 100) set in a clean room (class 1000) at Ibaraki University to prevent contaminant mixing with the sample. The cured samples were microtomed by Leitz-Reichert Super Nova ultramicrotome. The thickness of each section was ~ 70 nm. Only one ultra-thin section among serial sections on a Cu grid was used to prevent multiple analyses of the same mineral grains. TEM observation of the ultramicrotomed sample revealed that one section contains more than 150 individual grains.

Ar ion bombardment: Conventional Ar bombardment method was used for coarse 2B test samples (Table 1). Four samples were prepared by using this method. Polished thin sections of the samples were demounted from glass slides after EPMA analysis. The demounted samples were attached to single-hole Mo grids by epoxy resin. Argon bombardment was performed by using GATAN model 600 ion milling machine. Accelerating voltage and current were 2.5 kV and 1.0 mA.

Focused Ga ion beam sputtering: FIB thinning system (Hitachi FB 2000) was applied for the TEM sample preparation of 2BC10 that consists mainly of FeNi metal. The FIB is an appropriate method for thinning a sample with a variety of mineralogy. Gallium ion beam with accelerating voltage 30 KeV and beam current 9.5 μA has exposed on a thin sample slice that was placed on a single-hole Mo grid. The thickness of the sample slice before FIB sputtering was 20 μm and that of the sputtered sample was approximately 100 nm with an area of 10 x 10 μm . The thinning takes 5 hours to complete.

2.5.2. Transmission electron microscopy

TEM observation was performed by using JEOL JEM-2000FX II with accelerating voltage 200 KeV. Along with high-resolution imaging and electron diffraction analysis, quantitative elemental analysis was performed by EDAX DX4 energy-dispersive X-ray spectrometer. Although the analysis was based on Cliff-Lorimer approximation, the effects by absorption were considered by regarding k factors. K factors have been already determined by one of the authors (T. Noguchi) using many mineral standards. For K factors of silicate analysis, we determined 12 factors. K factors for Na, Mg, Al, Cl, K, Ca, and Fe were determined by using ultramicrotomed mineral standards. K factors for S, Ti, Cr, Mn, and Ni were determined by using ion thinned mineral standards. K factors for Fe-Ni metals and sulfides were determined by using ultramicrotomed mineral standard.

For the analysis of feldspar minerals in the fine-grained 2AF series samples, we used liquid nitrogen cooled analytical stage, Gatan model 633. The sample was cooled to -173 °C during observation and analysis of feldspars. As shown later, the cooling greatly lessens the compositional change of feldspars during analysis and the decomposition rates of crystal structures during observation under high magnifications.

3. RESULTS OF ANALYSIS

The results of SEM observation, EPMA analysis, and X-ray diffraction analysis of all sample particles except for 2BC10, which was examined only by TEM, are summarized in Appendix so as to show textural, mineralogical, and compositional characteristics of individual samples.

3.1. 2A test sample - host mineralogy

Coarse particles, 2AC1 to 2AC28, show a variety of mineralogical properties. Only 8 particles are dominated by a single phase (see Appendix): olivine (2AC10, 2AC24, and 2AC25), troilite (2AC7 and 2AC8), kamacite (2AC1 and 2AC15), and taenite (2AC18). The presence of the single-phase particles indicates that the largest crystal size of these minerals exceeds 100 μm . The other 20 particles are composites of several kinds of minerals. Among 28 sample particles, most abundant mineral is olivine and next is low-Ca pyroxene. Olivine has a homogeneous Fe/Mg ratio with Fa 15.1 ± 0.6 (Fig. 1a). CaO and MnO concentrations in olivine are less than 0.1 wt% and from 0.4 to 0.6 wt%, respectively (Fig. 2a). Low-Ca pyroxene also has a homogeneous Fe/Mg ratio with Fs 13.9 ± 0.7 (Fig. 1b). But Ca/(Mg+Fe) ratio is not homogenized between grains (Fig. 3a). Both MnO and Cr₂O₃ concentrations in low-Ca pyroxene varies from < 0.1 to 0.8 wt% (Fig. 4a). TiO₂ and Al₂O₃ concentrations are both less than 0.4 wt% (Fig. 5a).

High-Ca pyroxene and plagioclase are also contained in the 2A samples. Wo content varies from 12 to 48, while Mg/Fe ratio is relatively constant (Fig. 3a). MnO concentration is similar to that of low-Ca pyroxene, but Cr₂O₃ is higher than that of low-Ca pyroxene (Fig. 6a). TiO₂, Al₂O₃, and Na₂O concentrations are from 0.3 to 1.4, from 1.3 to 5.5, and < 1.1, respectively. Plagioclase is contained in many 2A test particles based on the X-ray diffraction patterns, but only a few samples have regions more than 10 μm rich in plagioclase. In such a region, tiny grains of olivine, pyroxene, and FeNi metal are present together with plagioclase. Therefore, chemical composition of plagioclase is difficult to obtain by EPMA analysis and thus it is determined by AEM method using a cold sample stage, as shown later.

Troilite and FeNi metals occur in abundance in the 2A test samples. They are commonly present with silicates. Troilite is the only sulfide contained in the 2A sample. FeNi metals are kamacite with Ni content up to 6 wt% and taenite with Ni from 33 to 50 wt% (Fig. 7a). Chromite, typically less than 10 μm but occasionally up to 30 μm , occurs together with troilite and FeNi metals in samples such as 2AC8, and 2AC20. Calcium phosphate from 10 to 20 μm in size also occurs in samples 2AC14 and 2AC19. 2AC4 shows signatures of melting (Appendix 2AC4). The sample contains many small gas bubbles indicative melting of silicates. X-ray diffraction patterns of this sample indicates the presence of magnetite (Appendix 2AC4). This suggests that the sample was melted at elevated oxygen fugacity and thus it may be a fragment of the fusion crust that was formed during atmospheric entry of the test-sample meteorite.

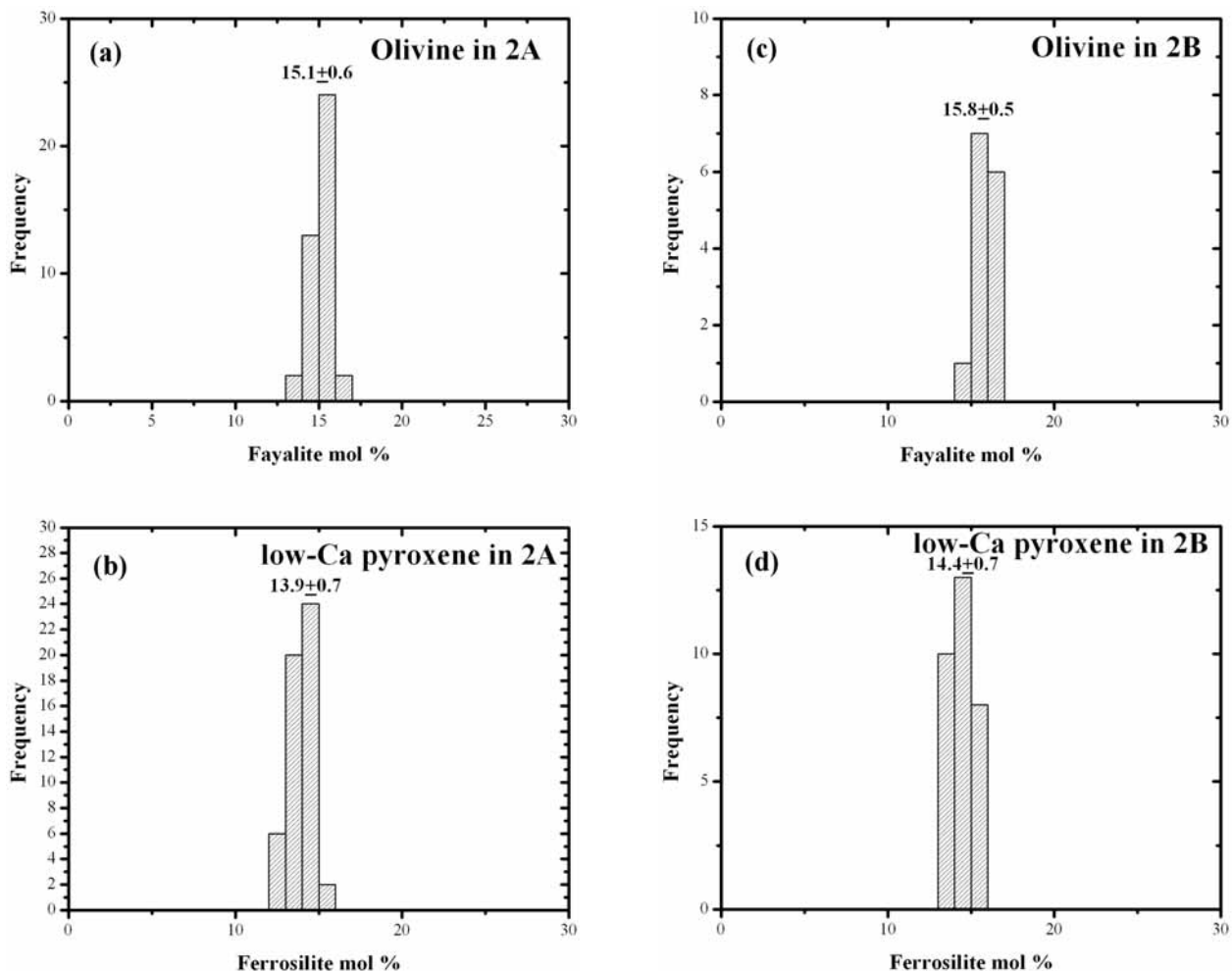


Figure 1. Histograms showing distributions of Fs and Fa contents. (a) Fa of olivine in the 2A sample. (b) Fs of low-Ca pyroxene in the 2A sample. (c) Fa of olivine in the 2B sample. (d) Fs of low-Ca pyroxene in the 2B sample.

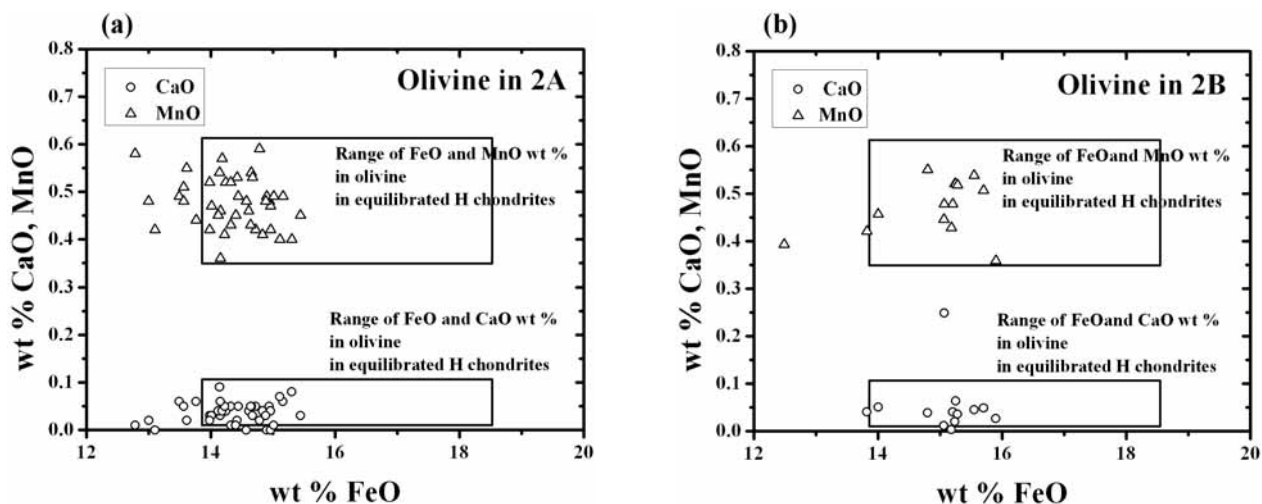


Figure 2. CaO and MnO concentrations in olivine in the 2A sample (a) and that in the 2B sample (b).

Samples being composed of fine particles, 2AF1 to 2AF10, show X-ray diffraction patterns similar to each other (see Appendices 2AF1 to 2AF10). Major phases are olivine, low-Ca pyroxene, plagioclase, and troilite. Based on the intensity ratio of some strong diffractions of low-Ca pyroxene between 38 and 45 diffraction angle (see Appendix section in Nakamura et al.,

2001b), low-Ca clinopyroxene are overabundant compared with orthopyroxene. FeNi metals are rare in fine-grained 2AF samples, compared with coarse 2AC samples. This is probably because metals are ductile and hard to be grinded during preparation of test samples. In order to obtain the relative abundance of major constituent minerals, olivine, low-Ca clinopyroxene, plagioclase, and troilite, Rietveld analysis was performed on the X-ray diffraction data of 2AF1 to 2AF10. Figure 8 shows the results of the Rietveld refinement of the 2AF6 sample and Table 2 shows the results of quantitative phase analysis of 2AF1 to 2AF10. The magnitude of errors is considered to be several percents. Samples, 2AF1 to 2AF10, show X-ray diffraction patterns similar to each other, and accordingly the relative mineral abundance is basically similar to each other (Table 2). All sample particles contain major minerals in the order of olivine > low-Ca clinopyroxene > plagioclase >> troilite. The results demonstrate that the Rietveld analysis is an appropriate method to obtain the relative mineral abundance and, in our knowledge, this is the first report of application of the Rietveld refinement to the fine-grained extraterrestrial material.

Table 2. The results of quantitative phase analysis of olivine, low-Ca pyroxene, plagioclase and troilite, by Rietveld analysis

Sample No.	Olivine	Low-Ca Pyroxene	Plagioclase	Troilite	(wt%)
2AF1	60.8	24.0	13.1	2.1	
2AF2	46.3	31.6	18.1	4.0	
2AF3	61.6	23.2	14.9	0.3	
2AF4	58.8	26.4	12.6	2.3	
2AF5	52.2	32.6	13.8	1.5	
2AF6	70.5	17.1	11.5	0.9	
2AF7	50.5	30.5	16.5	2.6	
2AF8	54.3	29.2	14.6	1.8	
2AF9	56.5	27.2	14.0	2.3	
2AF10	52.0	32.8	12.3	2.9	

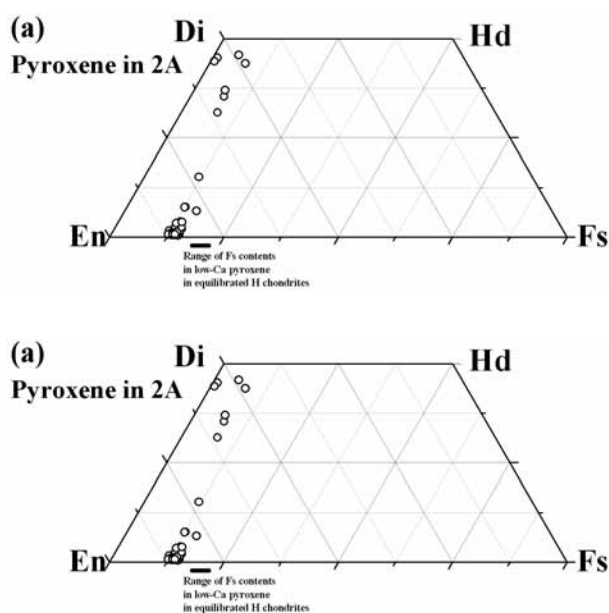


Figure 3. Pyroxene compositions of the 2A sample (a) and the 2B sample (b).

TEM observation was performed on 5 samples, 2AF1 to 2AF5. Detailed TEM observation was performed on one sample 2AF2, because bulk mineralogy of these five samples was basically the same, as was revealed by X-ray diffraction analysis, and because more than 150 mineral grains could be investigated using only one sample. Low-Ca pyroxene is composed of areas of both ortho- and clinopyroxene (Fig. 9a). Weak intensities of diffraction spots from orthopyroxene suggest that clinopyroxene is

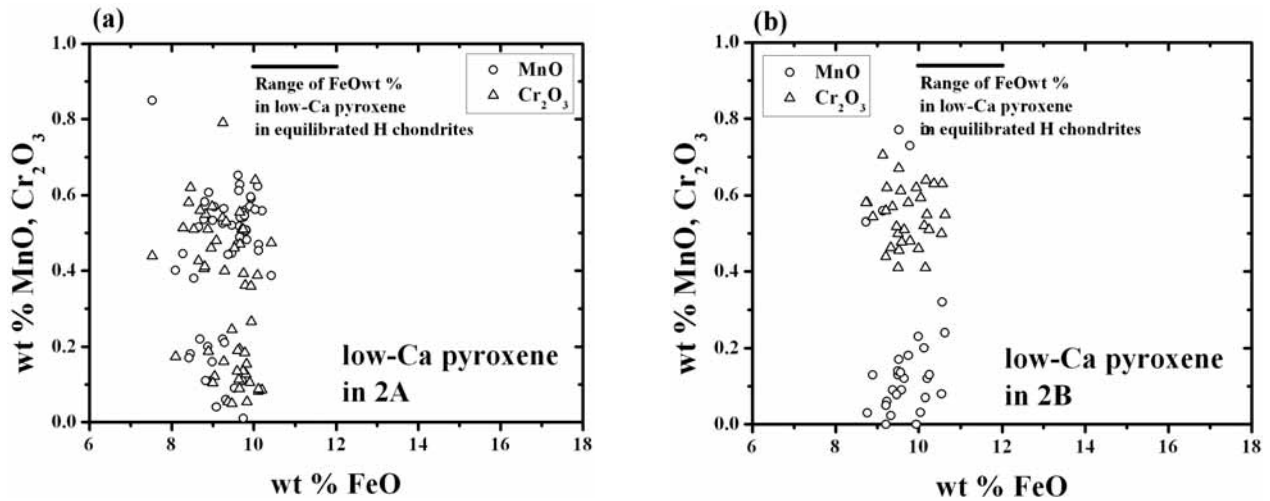


Figure 4. MnO and Cr₂O₃ concentrations in low-Ca pyroxene in the 2A sample (a) and the 2B sample (b).

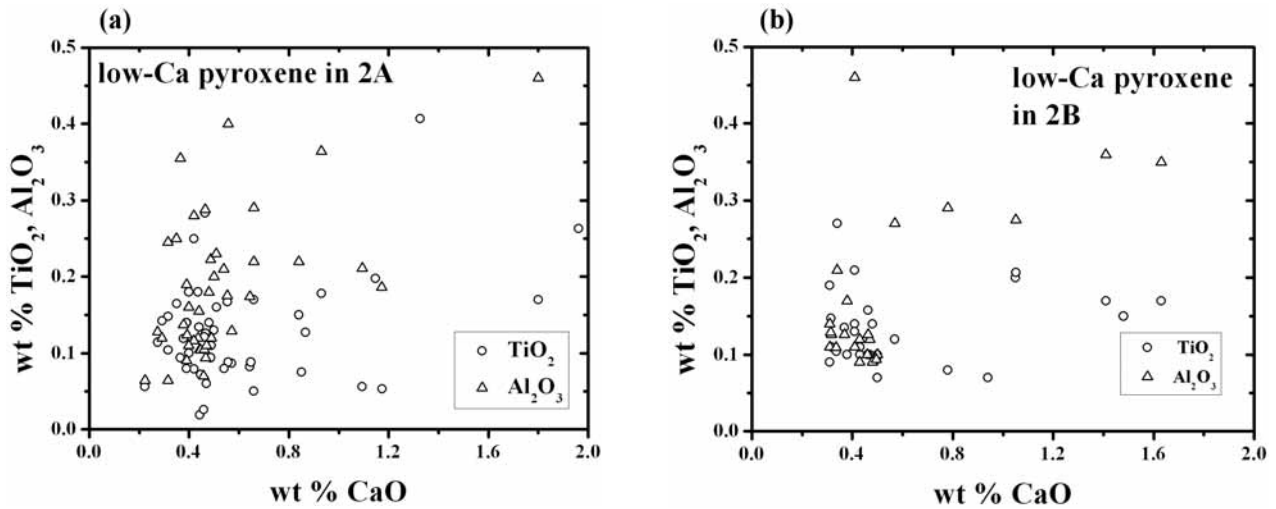


Figure 5. TiO₂ and Al₂O₃ concentrations in low-Ca pyroxene in the 2A sample (a) and the 2B sample (b).

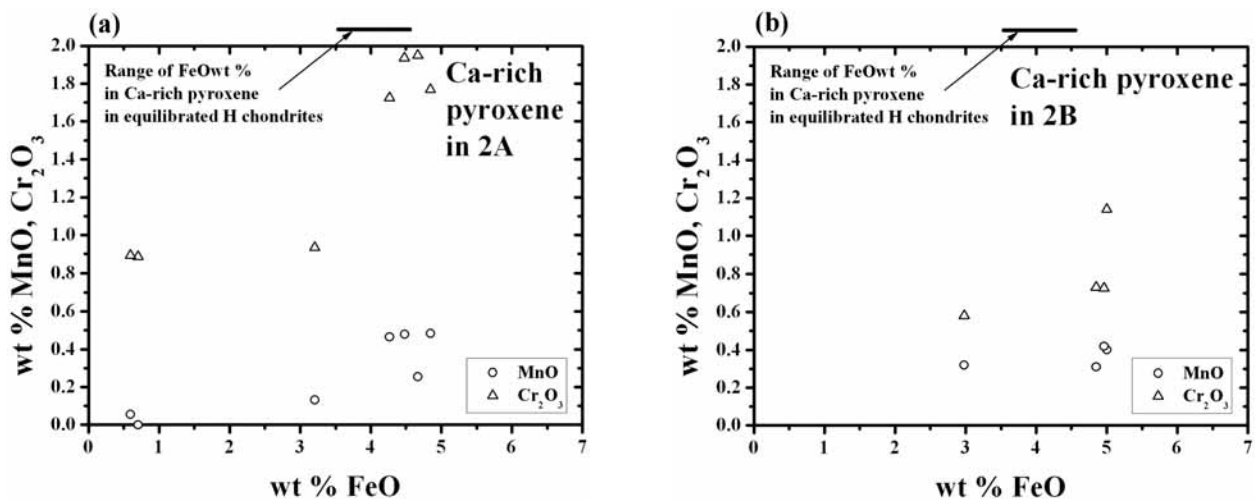


Figure 6. MnO and Cr₂O₃ concentrations in high-Ca pyroxene in the 2A sample (a) and the 2B sample (b).

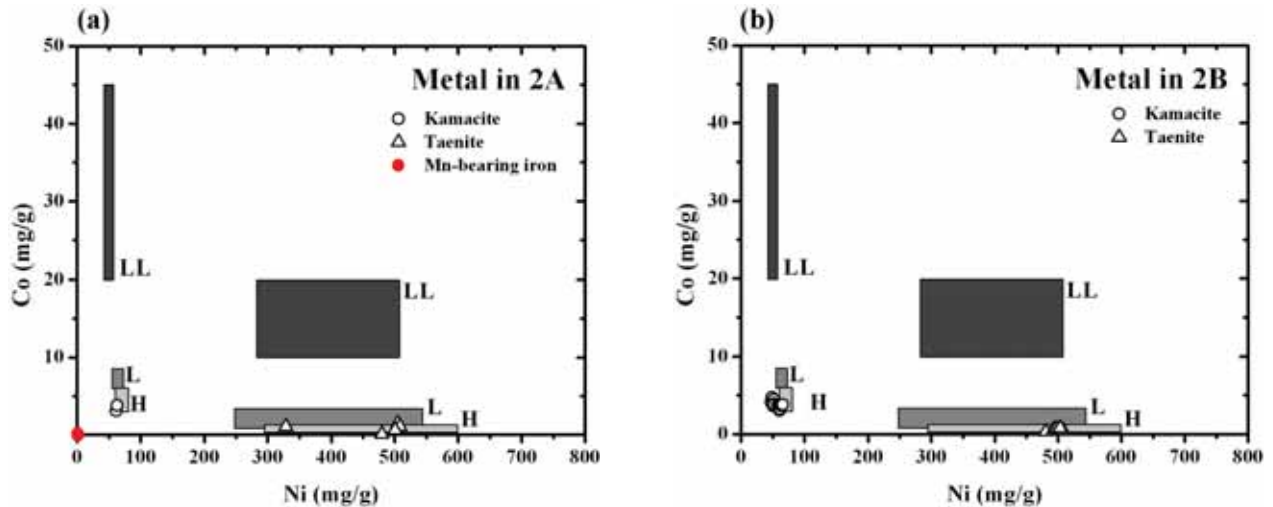


Figure 7. Co and Ni concentrations in FeNi metals in the 2A sample (a) and the 2B sample (b).

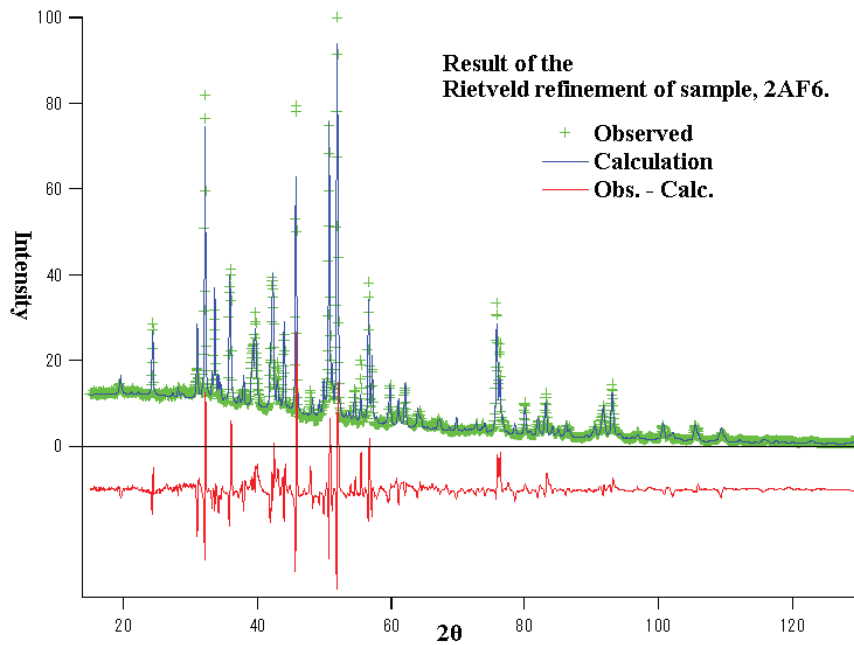


Figure 8. The result of Rietveld analysis of sample of 2AF6. The green cross is observed intensity, the blue line is calculated intensity and the red line is error. Some errors are still remained around strong diffraction peaks but the observed and calculated diffraction patterns are basically corresponded.

more abundant than orthopyroxene. Plagioclase is less than several microns diameter. AEM analysis showed that most plagioclase has compositions between $An_9Ab_{86}Or_5$ and $An_{13}Ab_{83}Or_4$, but there are also some alkali feldspar enriched in potassium with compositions from $An_1Ab_{33}Or_{66}$ to $An_0Ab_{47}Or_{53}$ (Fig. 10). Alkali feldspar (Fig. 9b) coexists with albitic plagioclase. Troilite is often observed, but kamacite is rare (Fig. 9c). Chromite occurs in both olivine and low-Ca pyroxene (Fig. 9d). Iron hydroxides lepidocrosite was found in a vein where 6-line ferrihydrite occurs together with lepidocrosite (Figs. 9e and f). The presence of iron hydroxides suggests that the 2A test sample is a “find” meteorite.

Optical microscope observation showed that olivine and low-Ca pyroxene crystals in both 2AC and 2AF samples such as 2AC18 (major phases are olivine and low-Ca pyroxene), 2AC22 (olivine and low-Ca pyroxene), 2AC23 (olivine and low-Ca pyroxene), 2AC24 (olivine), 2AF8, 2AF9, and 2AF10 exhibit wavy extinction, indicative of shock effects.

3.2. 2A test sample -mineralogy of contaminants

2A test sample contains very small amounts of strange materials that are never expected to occur in primitive chondritic meteorites. It is important to describe the mineralogy of these strange materials, because in the analysis of a real asteroidal sample they are “xenolith” materials coming from other planetary bodies.

Quartz-calcite composite: this strange material is detected in the four samples 2AC26, 2AC27, 2AC28, and 2AF2. The former three samples are dominated by quartz-calcite composite as is indicated by X-ray diffraction analysis (see Appendices 2AC26, 2AC27, and 2AC28), while the latter sample contains several tiny quartz particles that are detected only by TEM observation. SEM observation of 2AC26 indicates that the quartz-calcite composite also contains small amounts of dolomite CaMgCO_3 , sillimanite Al_2SiO_5 , corundum Al_2O_3 , and carbonaceous materials (Appendix 2AC26). Sillimanite crystals occur in the form of lath-like acicular morphology. X-ray diffraction patterns of 2AC27 and 2AC28 are very similar to that of 2AC26, suggesting the same mineralogy. The quartz-calcite composite is probably a constituent of terrestrial metamorphic rocks. TEM observation of 2AF2 showed that the sample contains a single quartz crystal (Fig. 9g). It may be a fragment of larger quartz-calcite composites such as 2AC26.

Ni-free Mn-bearing Fe metal: the sample of 2AC15 is a particle of Fe metal (Appendix 2AC15). The features set this Fe metal apart from metals in other sample particles are the complete absence of both Ni and Co and the presence of approximately 1 wt% of Mn. These compositional features have never been observed in FeNi metals in primitive chondritic meteorites. A nickel-cobalt diagram of FeNi metals in the 2A test sample (Fig. 7a) indicates that only Fe metal of 2AC15 is plotted on the origin (free of Ni and Co), out of the compositional trend of other FeNi metals. In addition, small amounts of magnetite are also present together with Fe metal based on the X-ray diffraction pattern (Appendix 2AC15). The presence of Mn and the coexistence of magnetite suggest that 2AC15 is a piece of factory-produced Fe metal, probably a fragment of some metallic tools.

Carbonaceous materials: the samples of 2AC2 and 2AC6 consist mostly of carbonaceous material. Interesting feature of the samples is that small grains of silicates and sulfides stick to surface of the carbonaceous materials (Appendices 2AC2 and 2AC6). X-ray diffraction analysis uncovers that the carbonaceous materials are amorphous and small silicates are olivine, low-Ca pyroxene, and plagioclase. Individual mineral particles are too small to be analyzed by EPMA. But the silicate mineralogy is similar to that of the other sample particles based on the X-ray diffraction patterns. Under an optical microscope, the carbonaceous materials are pale yellow similar to the color of epoxy resin. Therefore, the two samples 2AC2 and 2AC6 are probably pieces of epoxy resin that has cemented the test-sample meteorite.

3.3. 2B test sample

2B test sample consists of relatively coarse particles and all particles show magnetism. X-ray diffraction analysis showed that 2BC1, 2BC2, and 2BC3 samples are dominated by FeNi metals, but rest of the samples contain silicates and sulfides as well as FeNi metals (see appendices 2BC1, 2BC2, and 2BC3). Both kamacite and taenite occur and the former contains Ni up to 7 wt%, while the latter contains Ni approximately 50 wt% (Fig. 7b). Cobalt concentrations in kamacite (~ 0.5 wt %) is higher than those in taenite (~ 0.2 wt %) (Fig. 7b). The anti-correlation of Ni and Co in metals is consistent with the properties of metallic grains in ordinary chondrites, especially equilibrated H chondrites (Fig. 7b). Troilite is also abundant. Chromite up to 20 μm in diameter occurs in 2BC4 and 2BC5. Compositional features of both major and minor elements in chromite again match those of chondrites, especially equilibrated H chondrites (Figs. 11a, b, and c). Calcium phosphate up to 20 μm is present in 2BC7 and 2BC8 samples. Most of them are whitlockite. Varieties and occurrence of metals, sulfide, and accessory minerals are similar to those of the 2A test sample.

X-ray diffraction analysis indicates that major silicates in the 2B sample are olivine, low-Ca pyroxene, and plagioclase (see Appendix). High-Ca pyroxenes such as augite and pigeonite also occur, but less abundant. Many silicate crystals are included in FeNi metals. Important textural evidence was found in a sample of 2BC9, where a well-defined radial pyroxene chondrule is present in contact to a large FeNi metal (Appendix 2BC9 and Fig. 12). Blebs of troilite occur in the periphery of the chondrule. The presence of the chondrule suggests that the 2B sample is a chondrite, in spite of metal-rich mineralogy.

Olivine in the 2B sample has a homogeneous Fe/Mg ratio with an average Fa content of 15.8 ± 0.5 (Fig. 1c). CaO and MnO concentrations in olivine are less than 0.1 wt% and from 0.4 to 0.6 wt%, respectively (Fig. 2b). Low-Ca pyroxene also has a homogeneous Fe/Mg ratio with Fs 14.4 ± 0.7 (Fig. 1d). The average Fe/Mg ratios of both olivine and low-Ca pyroxene of the 2B sample are in agreement with those of 2A sample within 1-sigma variation. Ca/(Mg+Fe) ratio of low-Ca pyroxene is not homogenized between grains (Fig. 3b). Both MnO and Cr₂O₃ concentrations varies from < 0.1 to 0.8 wt% (Fig. 4b). TiO₂ and Al₂O₃ concentrations are both less than 0.5 wt% (Fig. 5b). Minor element concentrations in olivine and low-Ca pyroxene in the 2B sample are also similar to those of the 2A sample. High-Ca pyroxene and plagioclase occur in minor amounts in the 2B samples. Wo content varies up to 47 with constant Mg/Fe ratios (Fig. 3b). Both MnO and Cr₂O₃ concentrations are similar to those of low-Ca pyroxene (Fig. 6b). TiO₂, Al₂O₃, and Na₂O concentrations range from 0.3 to 1.0, from 0.5 to 3.0, and < 1.0, respectively. Based on the X-ray diffraction patterns, plagioclase occurs in many 2B samples such as 2BC7. Grain size of plagioclase is less than 5 μm , similar to the plagioclase in the 2A samples.

TEM analysis was carried out on samples of 2BC6, 2BC7, 2BC8, 2BC9, and 2BC10. Intensive observation was done on 2BC7, 2BC8, and 2BC9 thin sections prepared by Ar ion bombardment and a 2BC10 thin section prepared by FIB method. Olivine in 2BC7 contains abundant dislocations with the density is $3.8 \times 10^9 \text{ cm}^{-2}$ (Fig. 13a). Their straight and parallel occurrences are typical for olivine grains in shocked meteorites. Low-Ca pyroxene is a mixture of ortho- and clinopyroxene (Fig. 13b). Some low-Ca pyroxenes contain numerous stacking faults and unit dislocations, suggesting that they are impacted (Fig. 13c). Like 2A samples, both sodic plagioclase (Fig. 13d) and alkali feldspar (Fig. 13e) occur. Both feldspars are very small ranging in size from 0.5 to 3 μm . The sodic plagioclase shows albite twin (Fig. 13d), while the alkali feldspar and coexisting plagioclase shows albite-Carlsbad twin (Fig. 13e). High-Ca pyroxene pigeonite in both 2BC8 and 2BC9 samples contain exsolution lamellae of augite (Figs. 13f and g). High-resolution imaging shows that an augite lamella has coherent boundaries to the host pigeonite (Figs. 13h and i). In contrast to the 2BC7, 2BC8, and 2BC9 samples, 2BC10 sample consists predominantly of elongated domains of FeNi metals (Fig. 13j).

4. DISCUSSION

A combination of multidiscipline analyses revealed that whole- and local-scale mineralogy of individual test sample particles. The procedures used in the present study are basically similar to those used in the previous technical report for the Hayabusa mission (Nakamura and Noguchi, 2003), but the procedures have evolved in the last four years through the study of cosmic dust. The main achievements are (1) application of Rietveld refinements to determination of the relative mineral abundance from synchrotron X-ray diffraction data, and (2) sample preparation techniques for TEM including ultramicrotomy for fine-grained aggregates and FIB method for single particles.

2A sample particles have mineralogy quite similar to H chondrites with petrologic type late 4 to early 5. Evidence for H chondrite classification is (1) Fe/Mg ratios of olivine and low-Ca pyroxene (Fig. 14), (2) CaO and MnO concentrations in olivine (Fig. 2a), and (3) Co and Ni distributions in FeNi metals (Fig. 7a). The Fe/Mg ratios of both olivine and low-Ca pyroxene in the 2A sample correspond to the lowest-end of the Fe/Mg variations for H chondrites (Fig. 14), suggesting that it is a sample of most reduced type of H chondrites. Evidence for the petrologic type 4-5 classification is (1) well equilibration of Fe/Mg ratios of both olivine and low- and high-Ca pyroxene, (2) the presence of crystalline plagioclase with several microns in size, (3) the presence of taenite with Ni concentration higher than 20 wt%, and (4) the variation of Wo contents in high-Ca pyroxenes. The former three criteria are well-known classification scheme defined by Van Schmus and Wood, but the last one is derived from TEM observation (Noguchi et al., 1992; Noguchi, 2005, unpublished data). One sigma variations of Wo contents in high-Ca pyroxene decrease with an increase of petrologic type (Fig. 15). The variation of the pyroxenes in the 2A test samples is plotted in a region where many type 4 and 5 ordinary chondrites are plotted (Fig. 15, also see 3a), which verifies the classification of the 2A sample to petrologic type 4-5. However, high abundance of low-Ca clinopyroxene is inconsistent with the petrologic 4-5 classification. This can be explained due to mechanical conversion from orthopyroxene to clinopyroxene under high pressures during shock metamorphism.

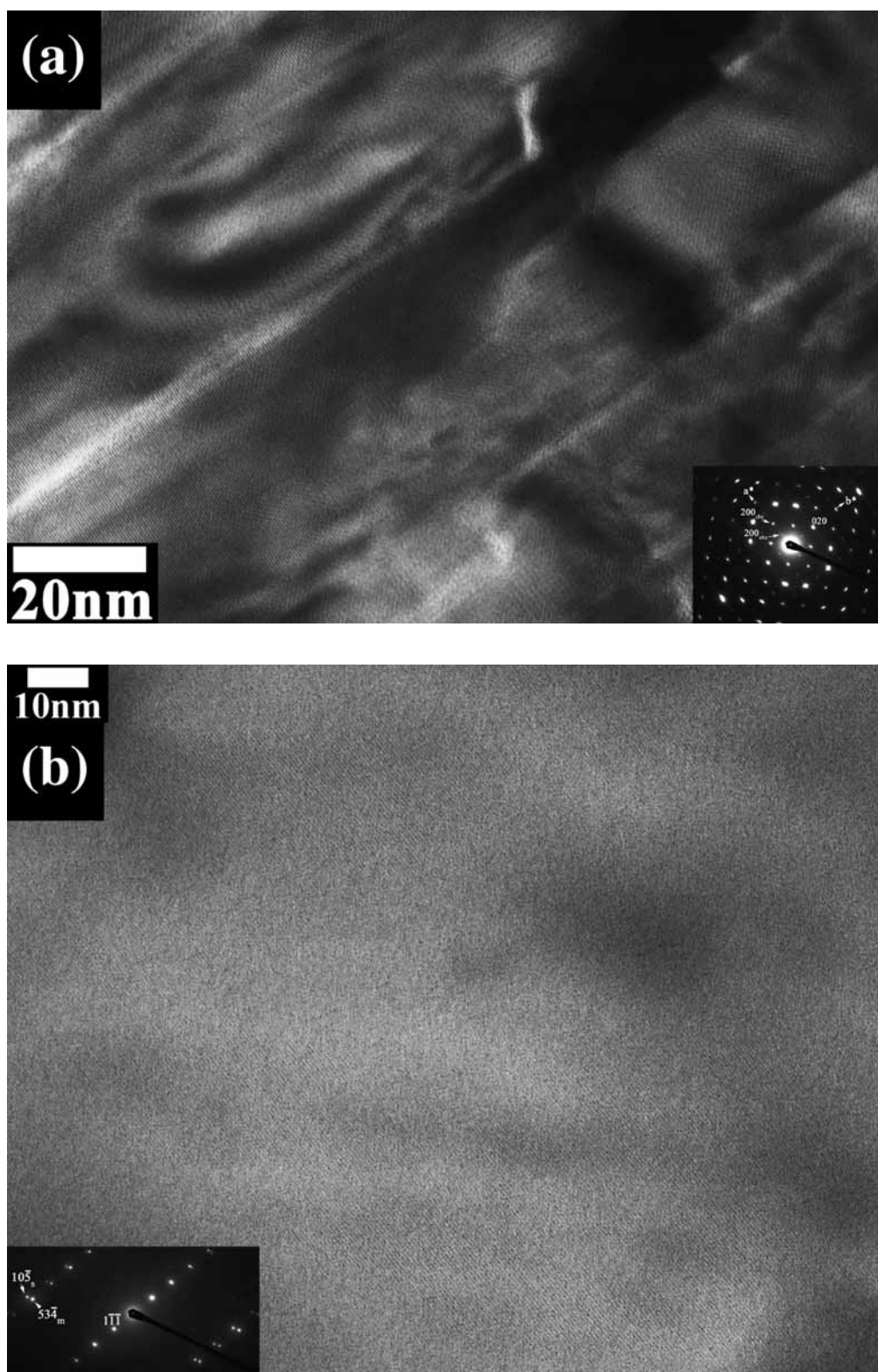
The presence of shock-induced wavy extinction of olivine and low-Ca pyroxene is consistent with the interpretation.

2A test sample contains a variety of contaminants: quartz-calcite composites (Appendix 2AC26), Ni-free Mn-bearing Fe metal (Appendix 2AC15), and carbonaceous materials (Appendix 2AC6). The quartz-calcite composites are unstable during thermal metamorphism on the H4-5 parent body and moreover such composites have never been reported even in chondritic regolith breccias. The Ni-free Mn-bearing Fe metal is also a strange component, as is clearly shown in a Co-Ni diagram (Fig. 7a). The Co and Ni contents of this metallic particle are out of regions for typical equilibrated H chondrites (e. g., Brearley and Jones, 1998). The carbonaceous materials show yellow in color and ductile properties, which differs black and brittle carbonaceous materials occasionally present in chondrites with low petrologic types. All these considerations suggest that the three kinds of materials are probably artificial contaminants.

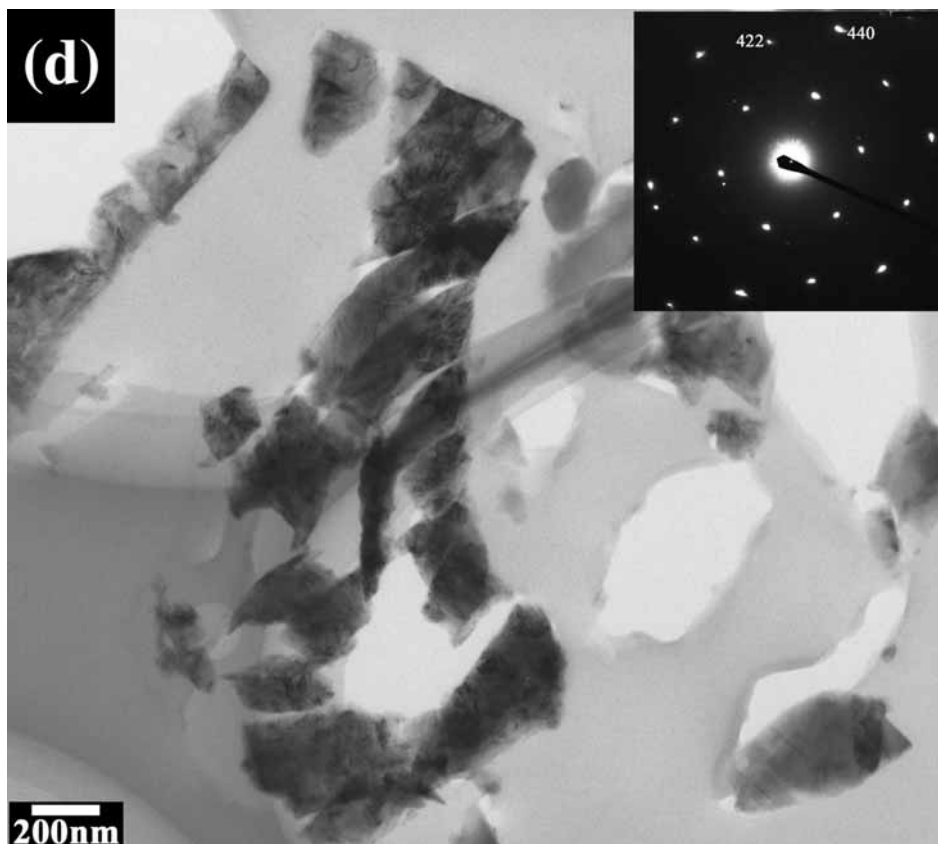
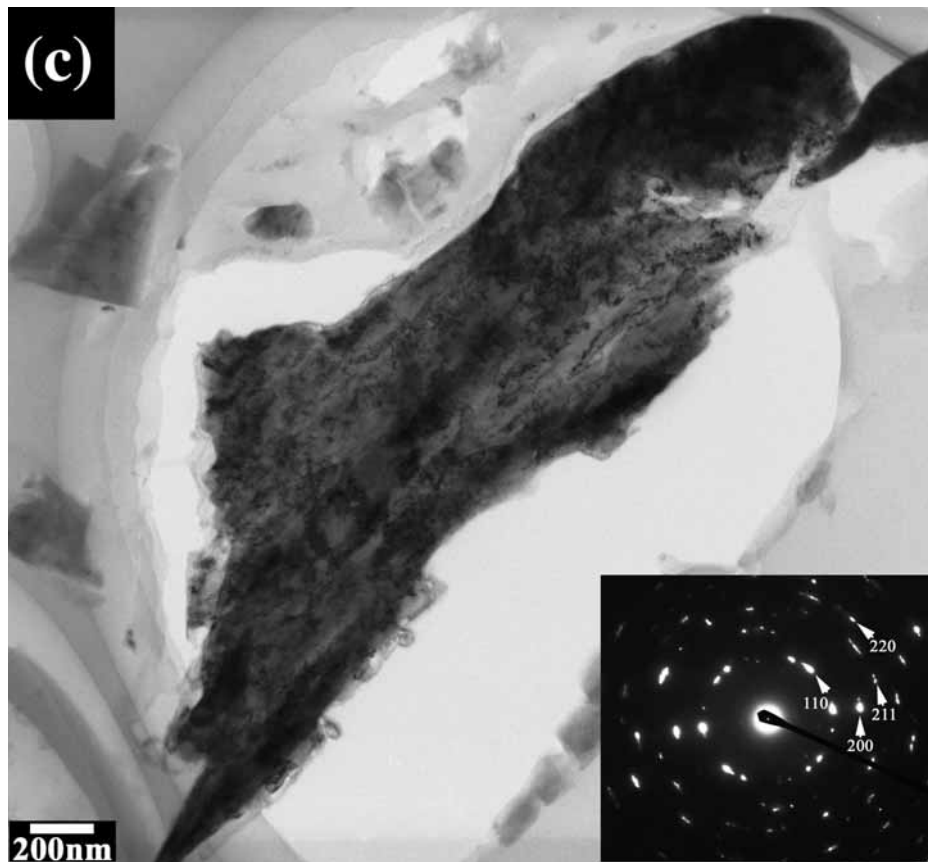
2B test sample completely differs from the 2A test sample in appearance: the former is larger, magnetic, and dull in color. However, the mineralogy is very similar between the two test samples, including minor and major element concentrations of olivine, low- and high-Ca pyroxene, FeNi metals, sulfide, and chromite. The only difference is that 2B sample is richer in metals than 2A sample. Therefore, we suggest that 2A and 2B test samples may be prepared from the same meteorite and that 2B sample may be a concentrate of metallic particles. The similarity in mineralogy between the two test samples suggests that 2B test sample is also H chondrite with petrologic type 4-5. The Wo variation of low- and high-Ca pyroxene in 2B sample is similar to that in 2A sample (Figs. 3b and 15). In addition, pigeonite in 2B sample exsolved augite lamellae with thickness of < 50 nm (Figs. 13f and g). The augite lamellae were formed during thermal metamorphism of the meteorite parent body and thus the occurrence and thickness of the lamellae reflect thermal regime of the host pigeonite. TEM observation of pigeonites in ALH77208 H4 and Jilin H5 chondrite (Noguchi et al., 1992; Noguchi, 2005, unpublished data) indicates that the pigeonites contain augite exsolution lamellae with thickness of < 50 and < 200 nm, respectively (Figs. 16a and b). The occurrence and thickness of the augite lamellae in the 2B test samples are similar to those in the two H chondrites, confirming the classification of the 2B sample to H chondrites with petrologic type 4-5.

Primitive achondrites such as acaplucoites and lodoranites are next candidate for source materials of both 2A and 2B samples, although the possibility is quite low considering some mineralogical features of primitive achondrites as discussed below. Primitive achondrites, acaplucoites and lodoranites, consist of olivine, low- and high-Ca pyroxene, plagioclase, FeNi metals, like 2A and 2B test samples. Their textures are basically granular except for rare relict chondrules in acaplucoites. It is difficult to reconstruct original textures before crushing of 2A and 2B test samples, but, at least the 2B test sample seems to have contained some chondrules based on SEM observation of textures of some 2B sample particles.

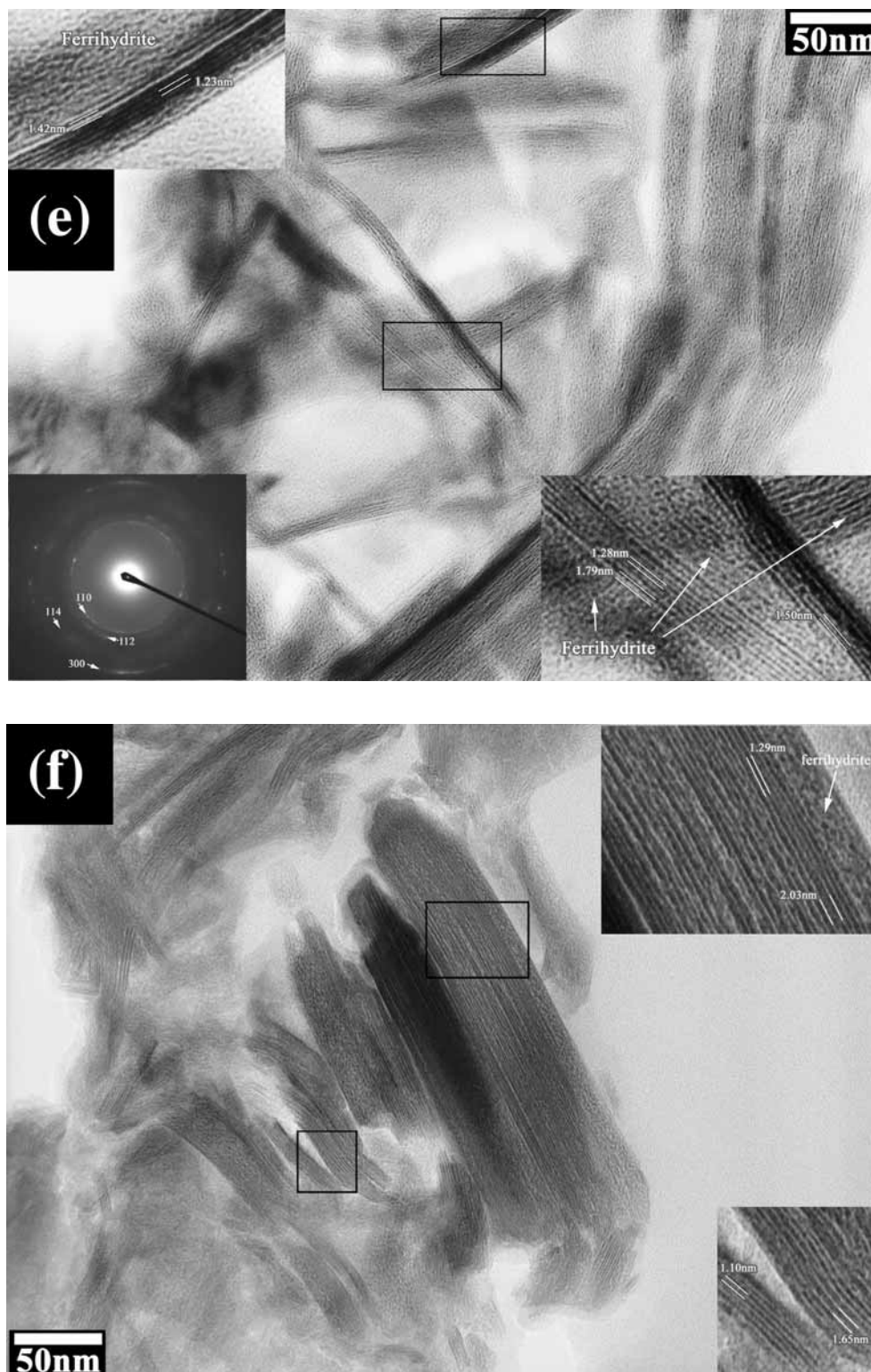
Averages Fe/Mg ratios of olivine and low-Ca pyroxene are $Fa_{15.1}$ and $Fs_{13.9}$, respectively, for the 2A test sample and $Fa_{15.8}$ and $Fs_{14.4}$, respectively, for the 2B test sample. On the other hand, in acaplucoites, compositional ranges of olivine and low-Ca pyroxene are $Fa_{4.2-13.3}$ and $Fs_{6.5-12.6}$, respectively (McCoy et al., 1996; 1997a, b). Their compositions are more magnesian than both 2A and 2B test samples. In lodoranites, these minerals are more magnesian than acaplucoites and show reverse zoning due to reduction during thermal metamorphism. No ferromagnesian mineral with such reduction was not found in both 2A and 2B samples. In addition, grain size of plagioclase correlates with intensity of thermal metamorphism. Plagioclase crystals in both 2A and 2B samples are very small less than 5 μm in diameter, which is far smaller than plagioclase in acaplucoites (more than 100 μm in diameter: McCoy et al. 1996). This indicates that thermal effects on plagioclase in both 2A and 2B test samples much weaker than those in acaplucoites. These data strongly suggest that both 2A and 2B samples are not fragments of primitive achondrites. Another supporting evidence of this interpretation is relative mineral abundances between olivine and low-Ca pyroxene in the 2A sample obtained by the Rietveld method. As shown in Table 2, olivine is always more abundant than low-Ca pyroxene in the 2A test sample, which is contrary to the case of acaplucoites (McCoy et al. 1996).



Figures 9(a) and (b)



Figures 9(c) and (d)



Figures 9(e) and (f)



Figure 9(g)

Figure 9. TEM images of 2AF2 sample particle. (a) High-resolution image of a low-Ca pyroxene fragment in 2AF2 sample down to the c^* direction. Selected area electron diffraction (SAED) pattern of this area shows that this low-Ca pyroxene is composed of areas of both ortho- and clino- low-Ca pyroxene (ortho- and clinobronzite based on AEM data). Weak intensities of diffraction spots from orthobronzite suggest that clinobronzite is more abundant than orthobronzite. (b) High-resolution image of an alkali feldspar fragment in 2AF2 sample. We encountered several such feldspar grains. In this case, EDS analysis shows that it has compositional variation from $An_{0.8}Ab_{32.9}Or_{66.2}$ to $An_{0.0}Ab_{47.0}Or_{53.0}$. SAED pattern shows that there are diffraction spots from both triclinic and monoclinic forms. However, there are no remarkable exsolution lamellae shown in perthite. Photomicrograph shows that there are modulations in this feldspar. They were probably caused by incomplete transformation from orthoclase to microcline. (c) Bright-field image of a kamacite fragment in 2AF2 sample. Kamacite is quite rare in 2AF2 sample. Only this fragment was discovered among the observation of 150 individual grains. SAED pattern of this fragment clearly shows that this kamacite grain was deformed during ultramicrotomy. (d) Bright-field image of a chromite fragment in 2AF2 sample. The occurrence of chromite as a single mineral fragment is rare. Most of them occur as inclusions in ferromagnesian silicates. (e) One fragment contains 0.5-micrometer vein. SAED pattern of this vein has four discontinuous diffraction rings. All of them coincide with diffraction peaks of 6-line ferrihydrite. However, high-resolution images of the vein (insets) revealed that the vein contains thin (< 20 nm) fibrous minerals. Their fringes are various from 1.23 to 1.79 nm. It is clear that these fibrous minerals are not ferrihydrite. They may be mixtures of lepidocrosite and clay minerals. And the interstices of these fibrous minerals are filled by ferrihydrite. (f) Another high-resolution image of the same vein shown in Fig. 9e. In this photomicrograph, Fe-predominant mineral grains partially keep tabular shapes. High-resolution images (insets) show that ferrihydrite replaces the tabular mineral. (g) We found one silica mineral grain in 2AF2 sample. SAED pattern of the grain shows that it is alpha-quartz.

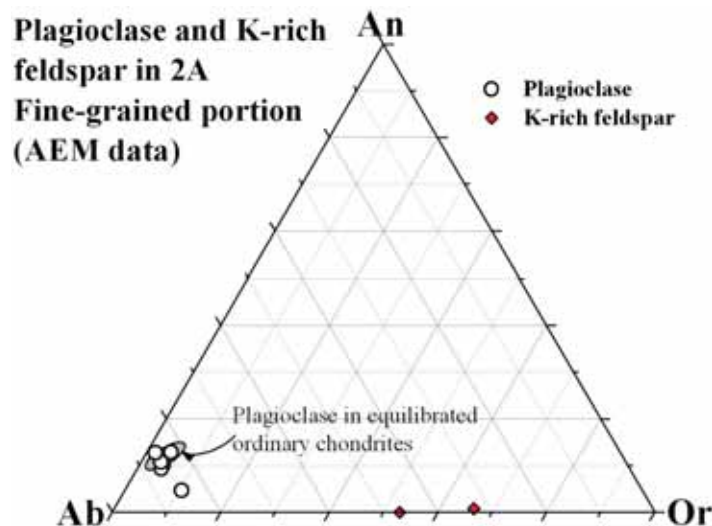


Figure 10. Plagioclase compositions of the 2AF2 sample, showing the presence of both sodic plagioclase and alkali feldspar.

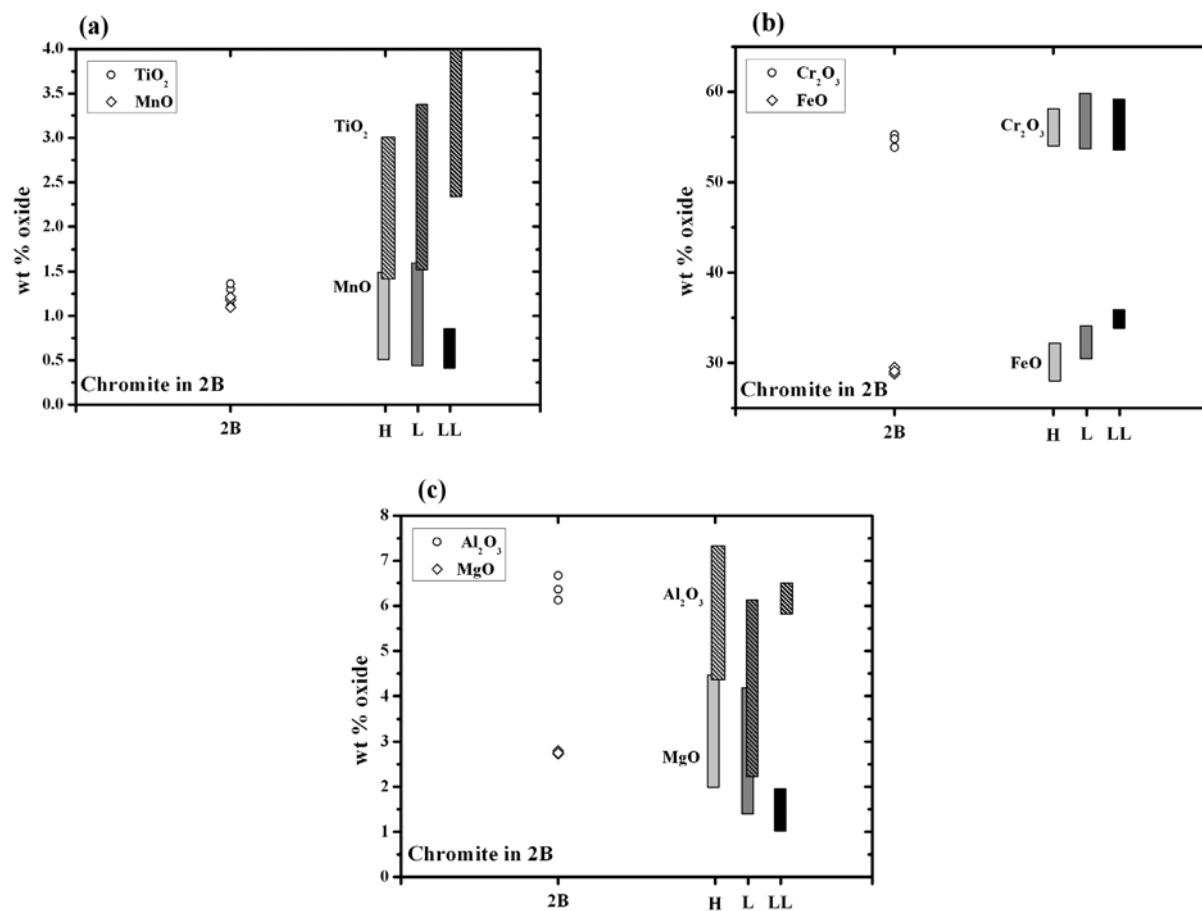


Figure 11. Major and minor element concentrations in chromite in the 2B sample. TiO₂ and MnO contents (a), Cr₂O₃ and FeO contents (b), and Al₂O₃ and MgO contents (c).

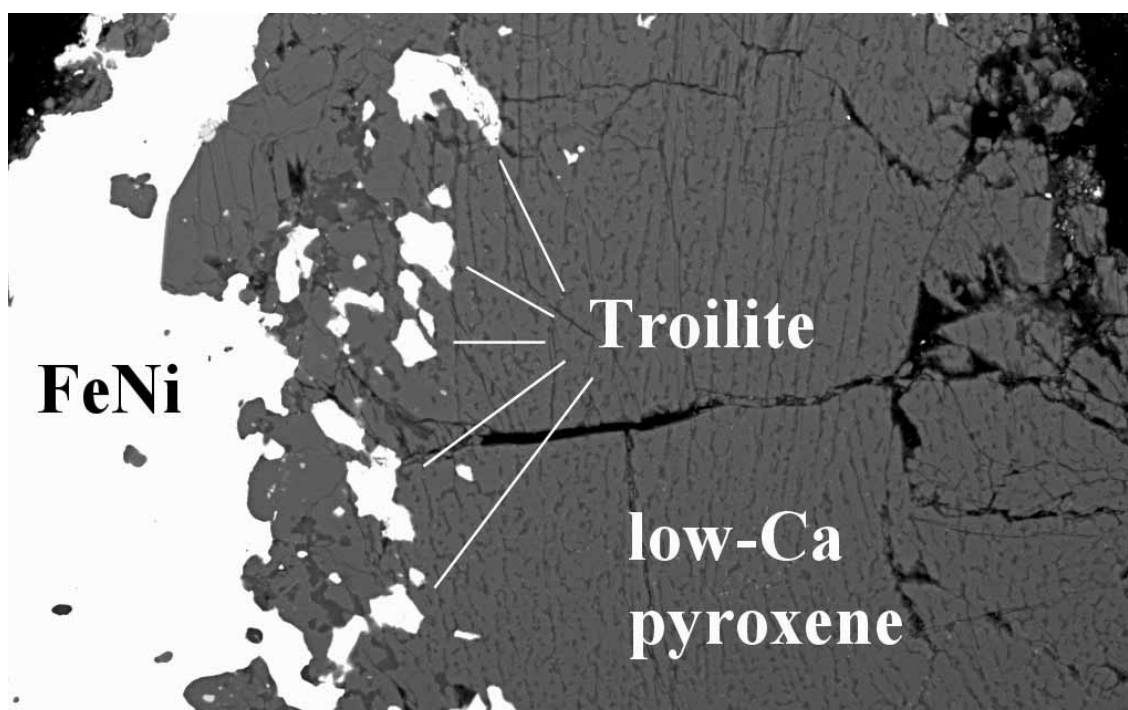
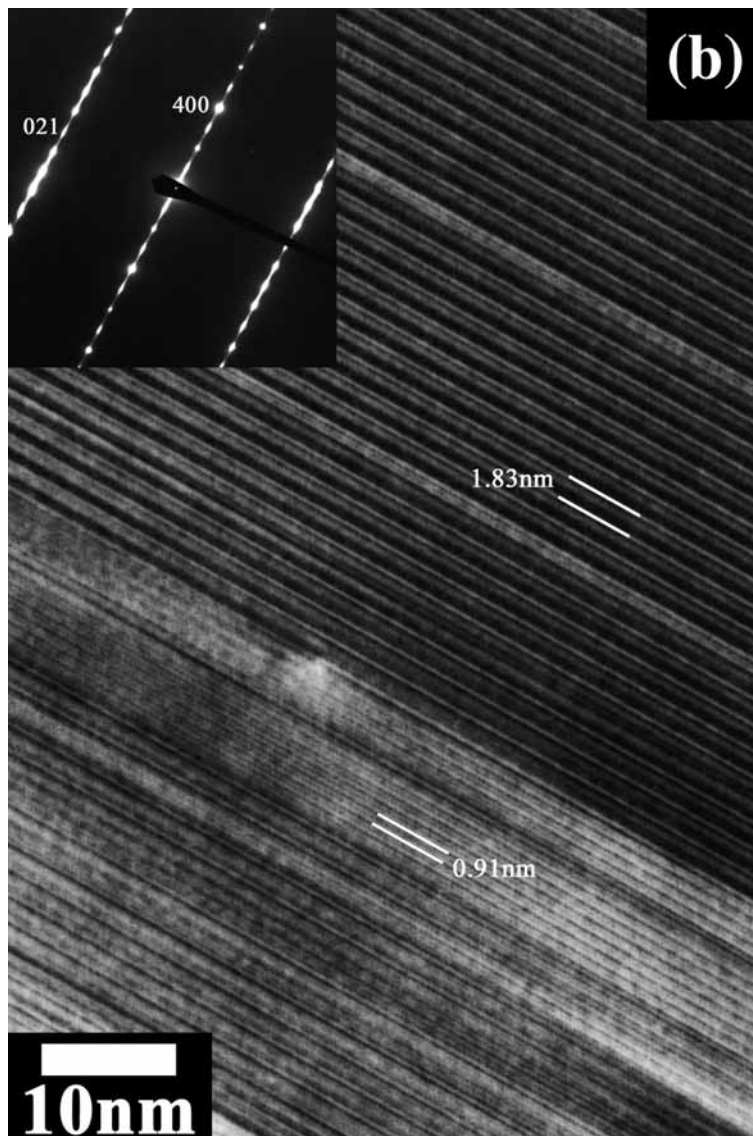
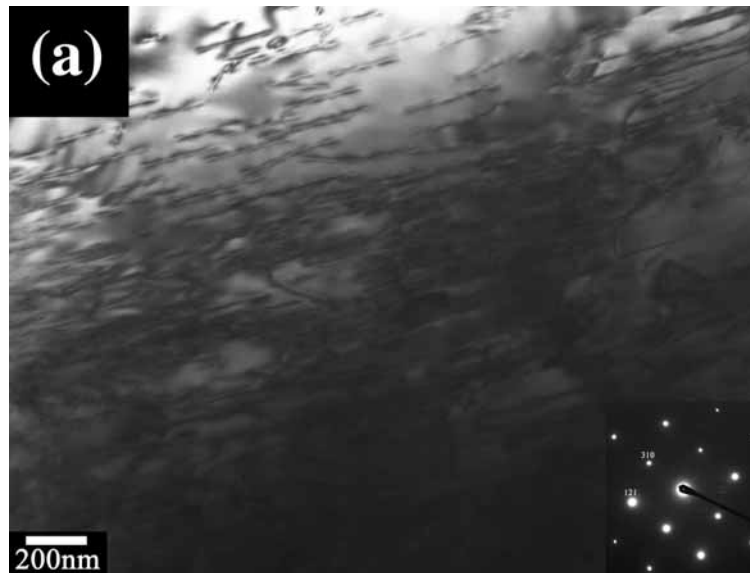
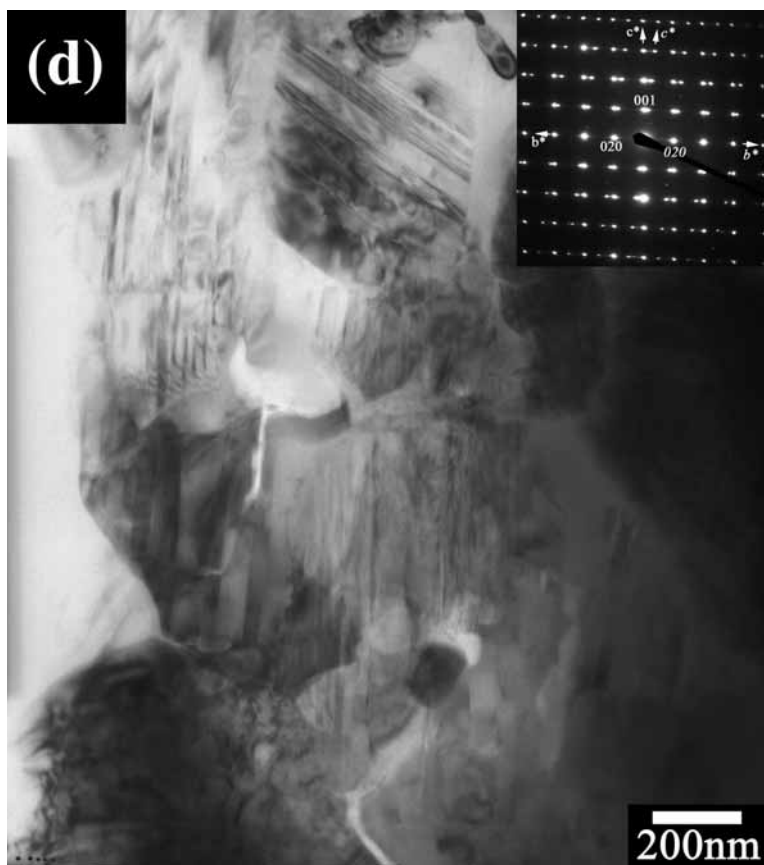
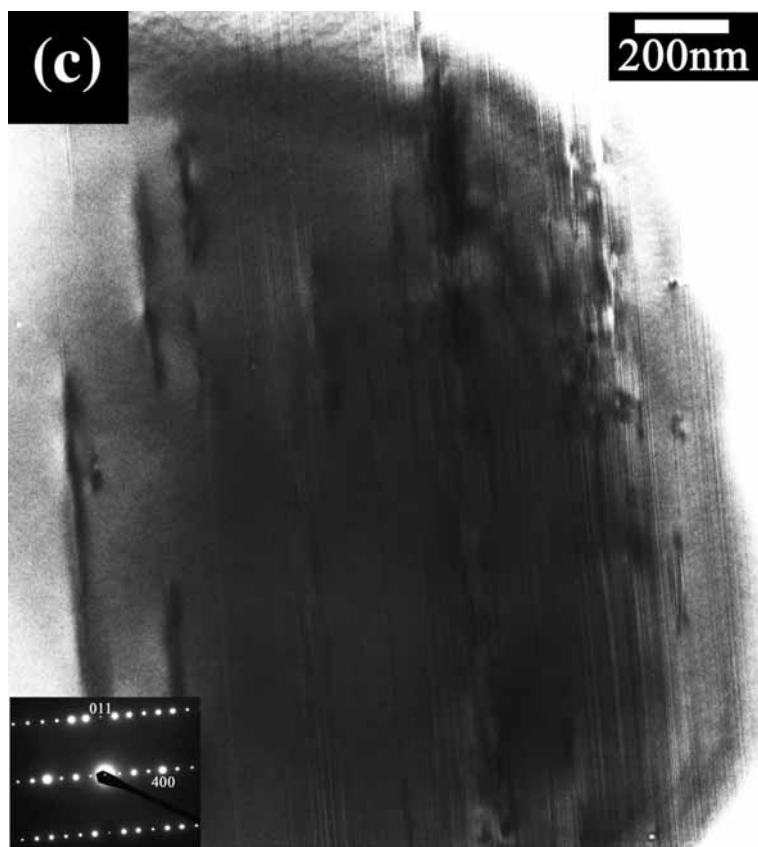


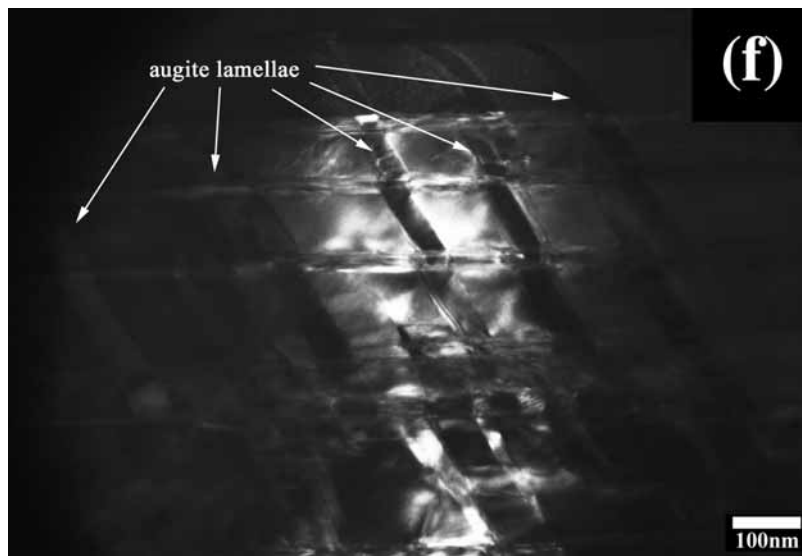
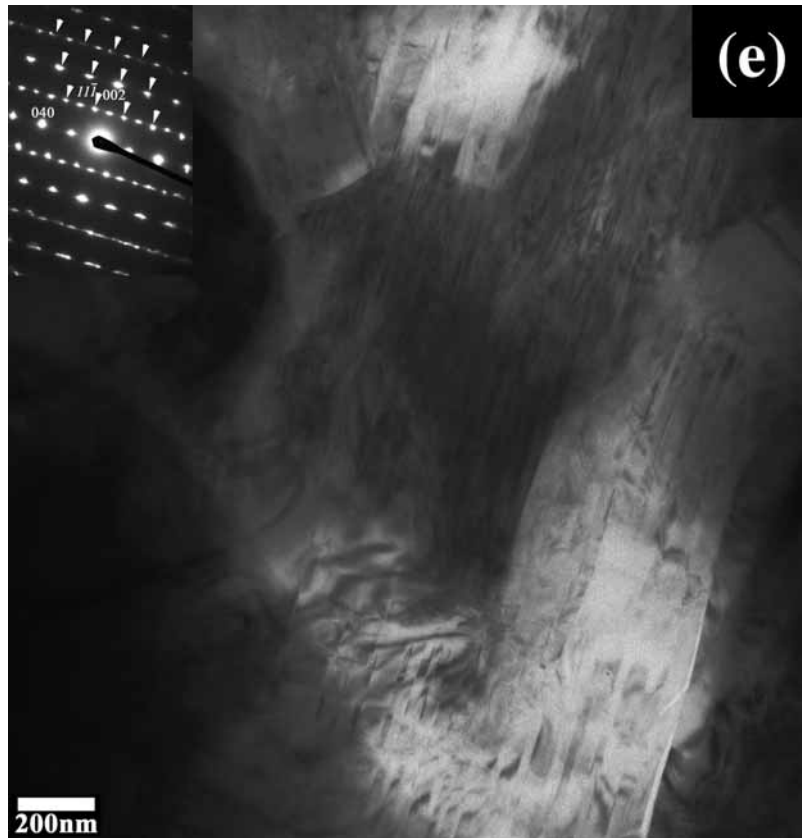
Figure 12. An enlarged view of a radial pyroxene chondrule in the 2B sample. Many troilite inclusions occur at the outer portions of the chondrule. A whole view of this chondrule is shown in Appendix 2BC9.



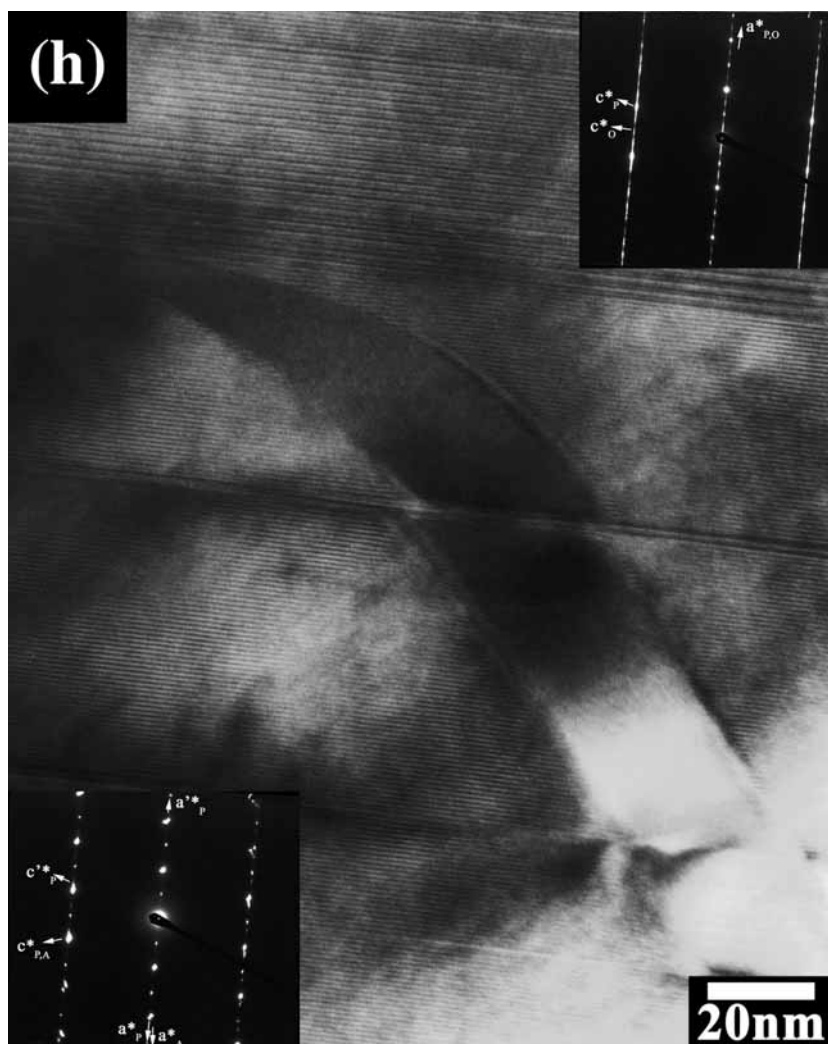
Figures 13(a) and (b)



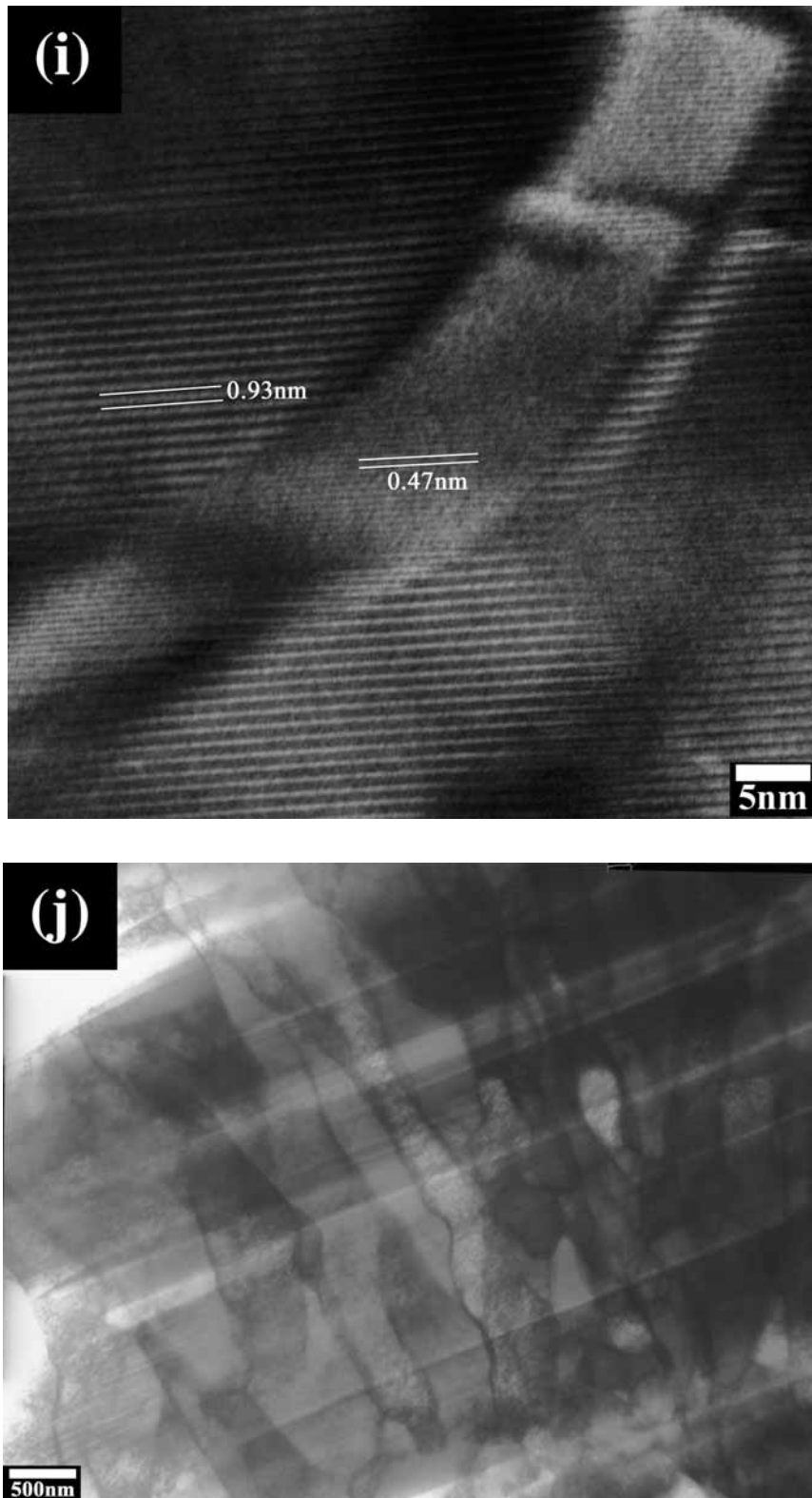
Figures 13(c) and (d)



Figures 13(e) and (f)



Figures 13(g) and (h)



Figures 13(i) and (j)

Figure 13. (a) Olivine in this sample contains abundant dislocations. Their straight and parallel occurrences are typical for olivine grains in shocked meteorites. Dislocation density of this grain is $3.8 \times 10^9 \text{ cm}^{-2}$. (b) High-resolution image of low-Ca pyroxene in 2BC7 sample. Low-Ca pyroxene of this sample is composed of abundant areas with orthorhombic structure and less abundant monoclinic structure. There is also some stacking disorder between the boundaries between ortho- and monoclinic- areas. (c) TEM image of a low-Ca pyroxene grain in 2BC9 sample. SAED pattern of this grain clearly shows that the majority of the grain is composed of orthopyroxene although TEM image shows that it contains abundant stacking disorder between ortho- and clino-areas. Some unit dislocations are also observed. (d) Bright-field image of sodic plagioclase grains in the interstices of low-Ca pyroxene and olivine large grains in 2BC7 sample. Sodic

plagioclase is 0.5 to 3 micrometer across. SAED pattern of a sodic plagioclase at the center of this photomicrograph shows albite twin. (e) There are alkali feldspar grains as well as sodic plagioclase among the interstices of coarse low-Ca pyroxene and olivine in 2BC7 sample. Their sizes are also from 0.5 to 3 micrometer across. SAED pattern of the alkali feldspar shows that it is microcline. The SAED pattern is composed of superimposed diffractions along [100] and [101] having the albite-Carlsbad twin relationship. (f) Dark-field image of augite lamellae-bearing pigeonite ($g=102_p$) in BC9 sample. Thin (< 50 nm) augite lamellae were also observed in pigeonite. It is remarkable that augite lamellae continue although the host pigeonite is twinned. It means that augite lamellae exsolved before twinning of pigeonite. The twinning of pigeonite is probably related transformation from pigeonite to orthopyroxene during thermal metamorphism. (g) Dark field-image of augite lamellae-bearing pigeonite in 2BC8 sample ($g=402_A$). Many bright augite lamellae with thickness < 20 nm can be seen. They are continuous although there are some stacking disorder and twins in the host pigeonite. (h) High-resolution image of lamellae-bearing pigeonite and low-Ca pyroxene in BC9 sample. Upper SAED pattern shows that low-Ca pyroxene is composed of a mixture of orthorhombic and monoclinic structures. In pigeonite, an augite lamella has coherent boundaries between host pigeonite. The lamella has a sigmoidal shape. The augite lamella is intermitted by stacking disorders in pigeonite. (i) High-resolution image of an augite lamella and the host pigeonite in 2BC8 sample. The boundaries between the lamella and the host are coherent although the direction of elongation of the lamella gradually changes. (j) Low magnification TEM image of a metallic grain in a fragment of 2BC10. This sample was prepared by FIB method. This metallic region is composed of elongated kamacite grains. Their high aspect ratios suggest that these grains experienced deformation probably due to shock. Grain boundaries of each kamacite grain are not thinned preferentially as often encountered when using conventional ion bombardment method.

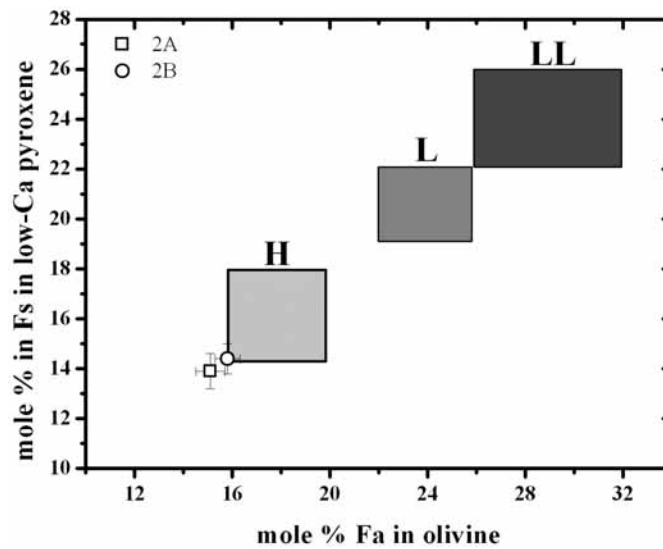


Figure 14. A correlation of Fs content in low-Ca pyroxene and Fa contents in olivine in ordinary chondrites. Fs and Fa contents of both 2A and 2B samples are located at the lowest-end of H chondrite compositional region.

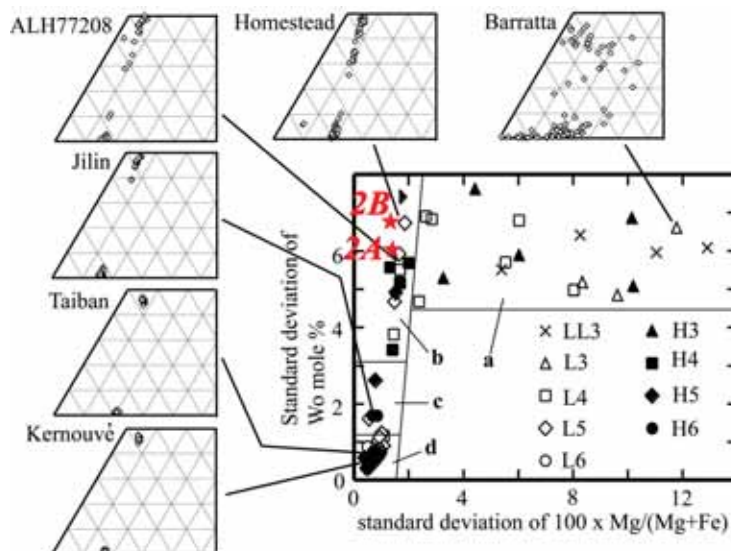


Figure 15. A correlation between variations of Wo contents and variations of Fs contents in high-Ca pyroxene in H and L chondrites with various petrologic types. Regions a, b, c, and d correspond to petrologic type 3-4, 4-5, 5-6, and 6, respectively. High-Ca pyroxenes in both 2A and 2B samples are plotted in the region of petrologic type 4-5.

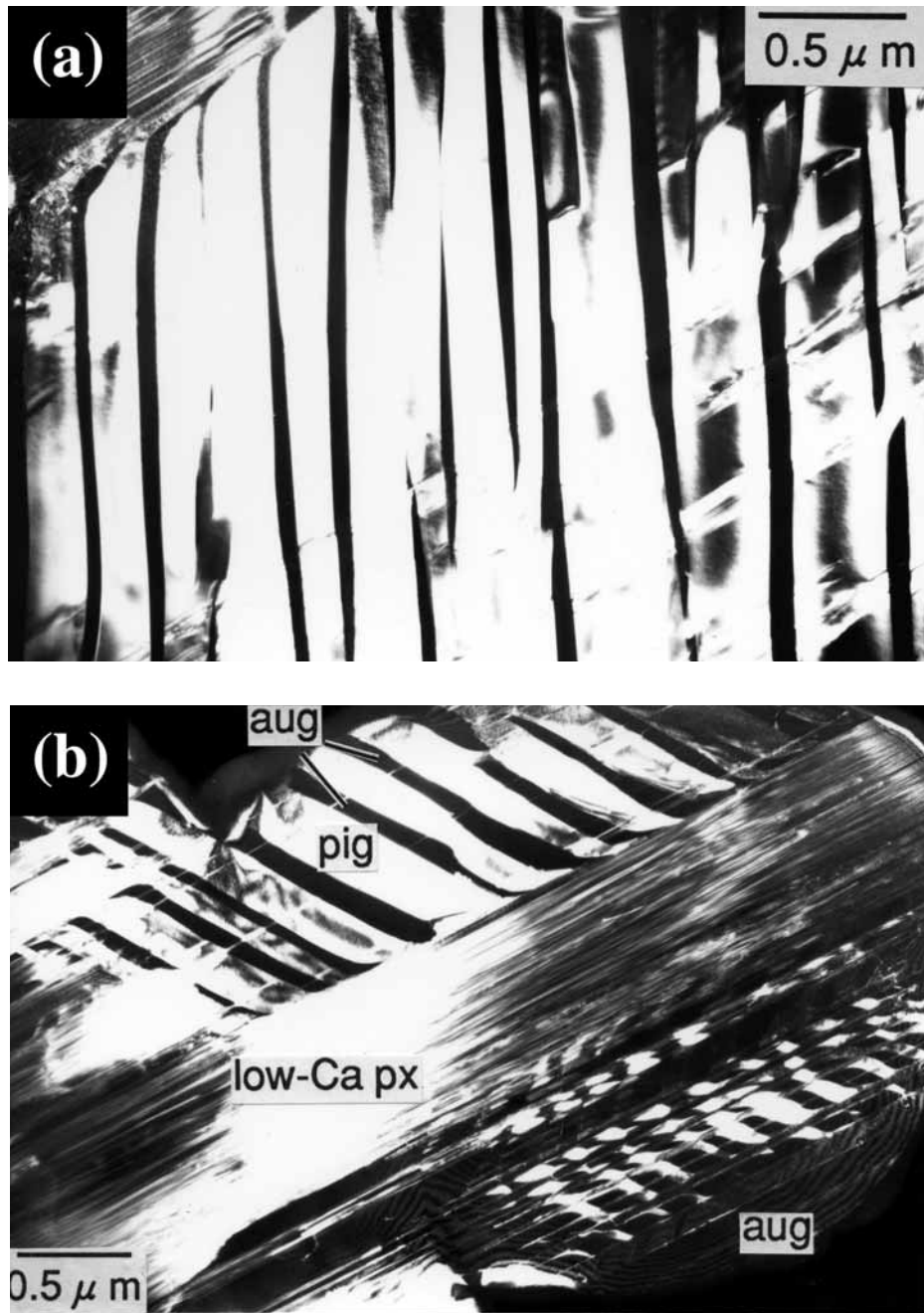


Figure 16. (a) Dark-field image of augite lamellae-bearing pigeonite in ALH 77208 H4 chondrite. The thickness of the lamellae is < 50 nm. The lamellae are continuous although there are some stacking disorder and twins in the host pigeonite. (b) Dark-field image of low-Ca pyroxene core and augite lamellae-bearing rims in Jilin H5 chondrite. Low-Ca pyroxene core is composed of orthorhombic areas with a lesser amount of monoclinic areas. Pigeonite is twinned and augite lamellae are affected by the twinning of the host pigeonite. The thickness of the lamellae is < 200 nm.

REFERENCES

- Birle, J.D., Gibbs, G.V., Moore, P.B. and Smith, J.V., 1968, Crystal structures of natural olivines. *Am. Mineral.*, **53**, 807-824.
- Brearely, A.J. and Jones, R.H., 1998, Chondritic meteorites. In *Reviews in Mineralogy Vol. 36 Planetary Materials*, (ed. J. J. Papike), pp. Chapter 3 1-398. Mineralogical Society of America, Washington.
- McCoy, T.J., Keil, K., Clayton, R.N., Mayeda, T.K., Bogard, D.D., Garrison, D.H., Huss, G.R., Hutcheon, I.D. and Wieler, R., 1996, A petrologic, chemical and isotopic study of Monument Draw and comparison with other acaplucoites: evidence for formation by incipient partial melting. *Geochim. Cosmochim. Acta*, **60**, 2681-708.
- McCoy, T., Keil, K., Muenow, D.W., and Wilson, L., 1997a, Partial melting and melt migration in the acaplucoite-lodranite parent body. *Geochim. Cosmochim. Acta*, **61**, 639-50.
- McCoy, T.J., Keil, K., Clayton, R.N., Mayeda, T.K., Bogard, D.D., Garrison, D.H., Hutcheon, I.D. and Wieler, R., 1997b, A petrologic and isotopic study of lodranites: evidence for early formation as partial melt residues from heterogeneous precursors. *Geochim. Cosmochim. Acta*, **61**, 623-37.
- Morimoto, N. and Guven, N., 1970, Refinement of the crystal structure of pigeonite. *Am. Mineral.*, **55**, 1195-1209.
- Nakamura, T., Yada, T., Noguchi, T., Nakamura, Y., Takaoka, N., Terada, Y., Nakai, I., and Tanaka, M., 1999, X-ray diffraction analysis of individual interplanetary dust particles and Antarctic micrometeorites using synchrotron radiation. *Meteoritics*, **34**, A86.
- Nakamura, T., Nakamura, Y. and Tanaka, M., 2001a, Identification of anhydrous and hydrous interplanetary dust particles by X-ray diffraction analysis. in Photon Factory Activity Report 2000, Part A (Highlights and Facility Report #18), Section 6 Crystallography (ed. by Ohsumi K), *KEK Progress Report 2001-2*, 30-31.
- Nakamura, T., Noguchi, T., Yada, T., Nakamura, Y., and Takaoka, N., 2001b, Bulk mineralogy of individual micrometeorites determined by X-ray diffraction analysis and transmission electron microscopy. *Geochim. Cosmochim. Acta*, **65**, 4385-4397.
- Nakamura, T. and Noguchi, T., 2003, Mineralogy of 100-mg test samples for Muses C mission. in The First Open Competition for the MUSES-C Asteroidal Sample Preliminary Examination Team (eds. by Kushiro, I., Fujiwara, A., and Yano, H.) *ISAS report SP No. 16*, 103-120.
- Nakamura, T., Noguchi, T., Zolensky, M.E., and Tanaka, M., 2003, Noble-gas signatures and mineralogy of the carbonate-rich lithology of the Tagish Lake carbonaceous chondrite: Evidence for an accretionary breccia, *Earth and Planetary Science Letters* **207**, 83-101.
- Nakashima, D., Nakamura, T., and Noguchi, T., 2003, Formation history of CI-like phyllosilicate-rich clasts in the Tsukuba meteorite inferred from mineralogy and noble gas signatures. *Earth and Planetary Science Letters*, **212**, 321-336.
- Noguchi, T., Fujino, K., and Momoi, H., 1992, A transmission electron microscope study of exsolution lamellae of pyroxenes in ordinary chondrites. Papers presented to the 17th Symposium on Antarctic Meteorites. 89-91. National Institute of Polar Research, Tokyo.
- Noguchi, T. and Nakamura, T., 2000, Mineralogy of Antarctic micrometeorites recovered from the Dome Fuji Station. *Antarctic Meteorite Research*, **13**, 285-301.
- Noguchi, T., Nakamura, T., and Nozaki, W., 2002, Mineralogy of phyllosilicate-rich micrometeorites and comparison with Tagish

Lake and Sayama meteorites. *Earth and Planetary Science Letters*, **202**, 229-246.

Prewitt, C.T., Sueno, S. and Papike, J.J., 1976, The crystal structures of high albite and monalbite at high temperatures. *Am. Mineral.*, **61**, 1213-1225.

Tokonami, M., Nishiguchi, K. and Morimoto, N., 1972, Crystal structure of a monoclinic pyrrhotite (Fe₇S₈). *Am. Mineral.*, **57**, 1066-1080.

Toraya, H., 1998, Weighting Scheme for the Minimization Function in Rietveld Refinement. *J. Appl. Cryst.*, **31**, 333-343.

Appendix:
back-scattered electron images,
chemical compositions,
diagrams for olivine and low- and high-Ca pyroxene, and
synchrotron X-ray diffraction patterns

Abbreviations

tr: troilite

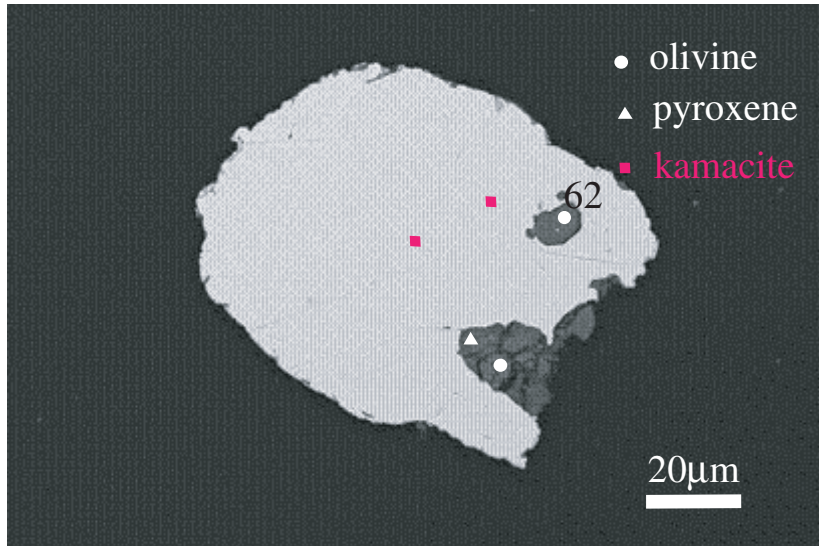
kam: kamacite

ol: olivine

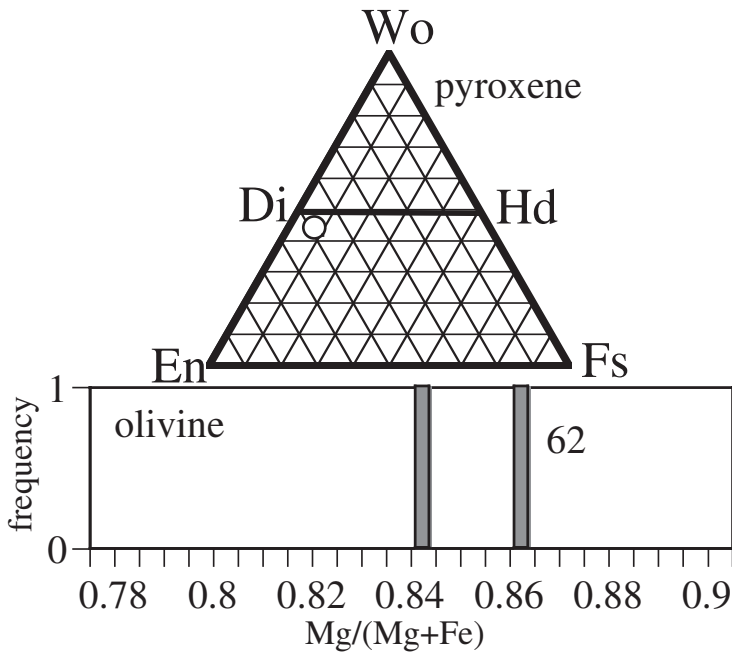
low-Ca px: low-Ca pyroxene

high-Ca px: high-Ca pyroxene

2AC1

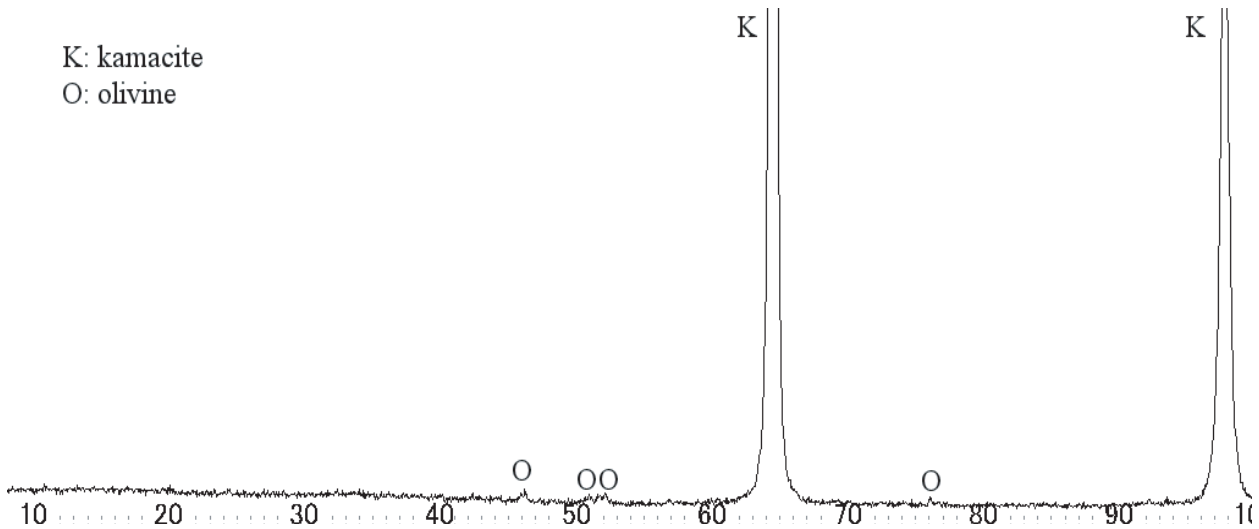


wt %	tr	kam
Ni		6.2
Fe		93.5
Mn		0.1
Co		0.3
Cr		0.0
S		0.0
P		0.0
Total		100.1

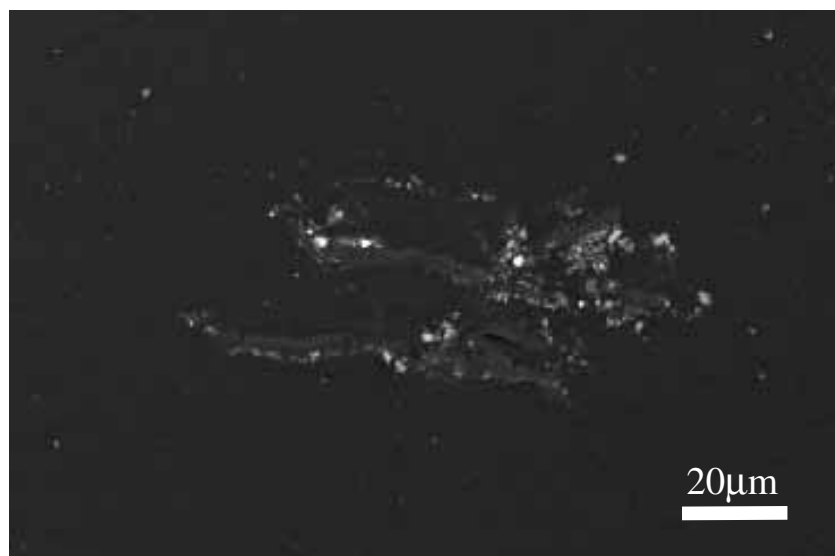


wt%	ol	low-Ca px	high-Ca px
SiO ₂	39.5		51.1
TiO ₂	0.0		1.0
Al ₂ O ₃	0.0		4.6
FeO	13.0		4.7
MnO	0.5		0.3
MgO	46.5		16.0
CaO	0.0		20.1
Na ₂ O	0.0		1.1
K ₂ O	0.0		0.0
Cr ₂ O ₃	0.0		1.9
NiO	0.0		0.1
P ₂ O ₅	0.0		0.0
SO ₃	0.0		0.0
total	99.5		101.0

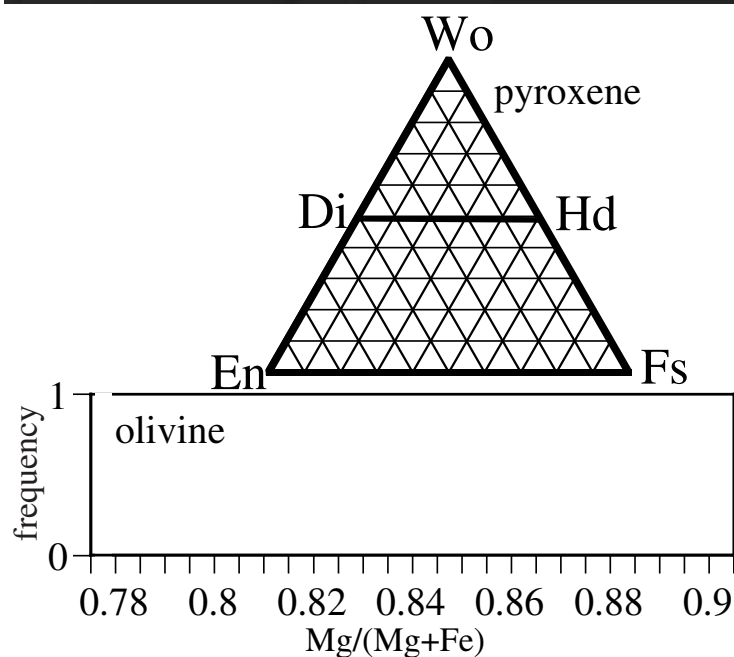
K: kamacite
O: olivine



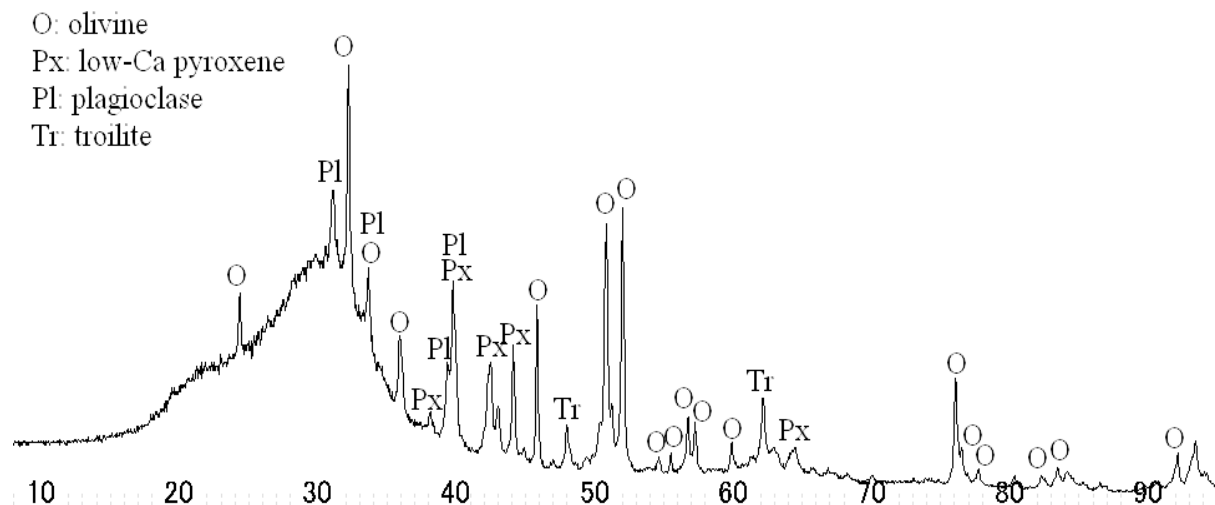
2AC2



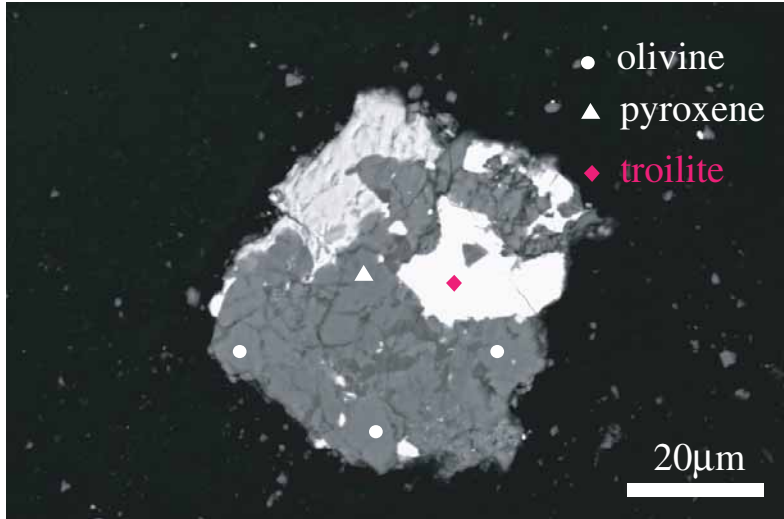
wt %	tr	kam
Ni		
Fe		
Mn		
Co		
Cr		
S		
P		
Total		



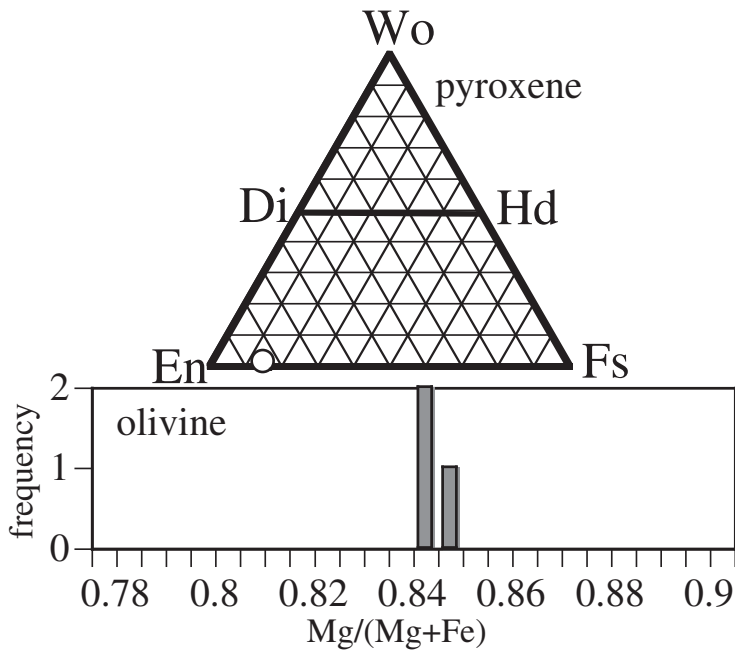
wt%	ol	low-Ca px	high-Ca px
SiO ₂			
TiO ₂			
Al ₂ O ₃			
FeO			
MnO			
MgO			
CaO			
Na ₂ O			
K ₂ O			
Cr ₂ O ₃			
NiO			
P ₂ O ₅			
SO ₃			
total			



2AC3

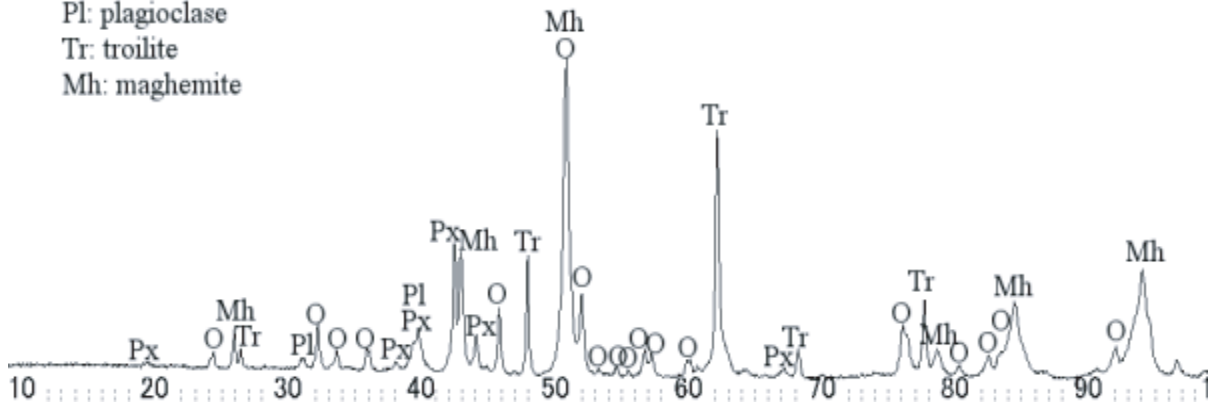


wt %	tr	kam
Ni	0.0	
Fe	62.8	
Mn	0.0	
Co	0.0	
Cr	0.7	
S	36.3	
P	0.0	
Total	99.9	

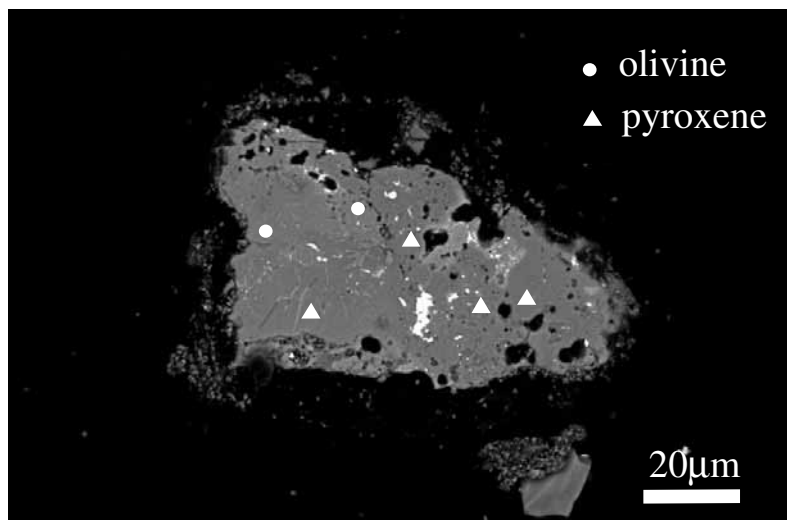


wt%	ol	low-Ca px	high-Ca px
SiO ₂	39.7	55.1	
TiO ₂	0.0	0.1	
Al ₂ O ₃	0.0	0.4	
FeO	14.9	9.7	
MnO	0.5	0.5	
MgO	45.7	31.2	
CaO	0.1	0.6	
Na ₂ O	0.0	0.2	
K ₂ O	0.0	0.0	
Cr ₂ O ₃	0.0	0.5	
NiO	0.0	0.0	
P ₂ O ₅	0.0	0.0	
SO ₃	0.0	0.0	
total	100.9	98.2	

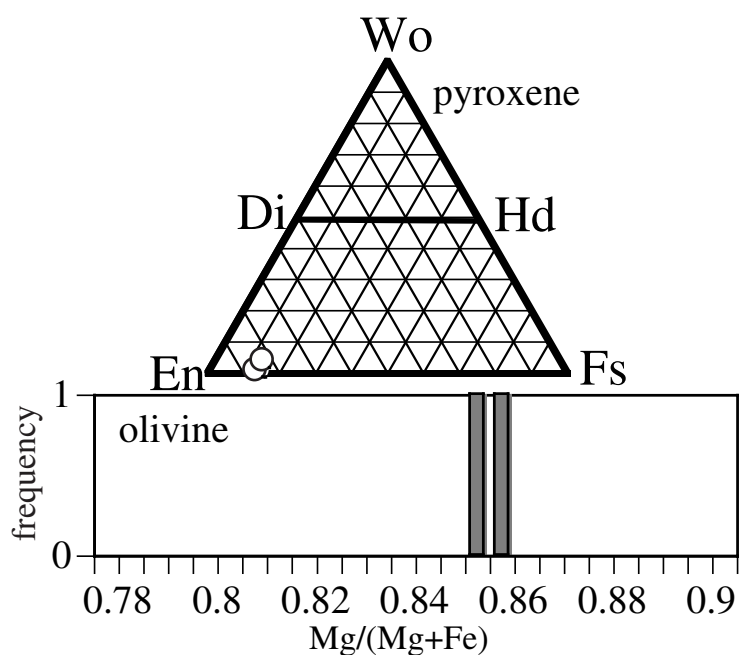
O: olivine
 Px: low-Ca pyroxene
 Pl: plagioclase
 Tr: troilite
 Mh: maghemite



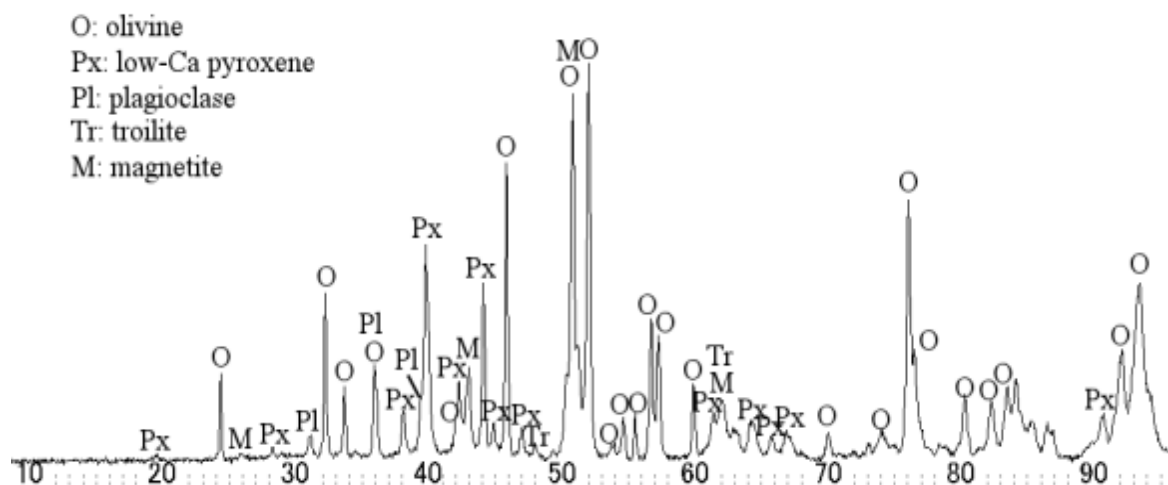
2AC4



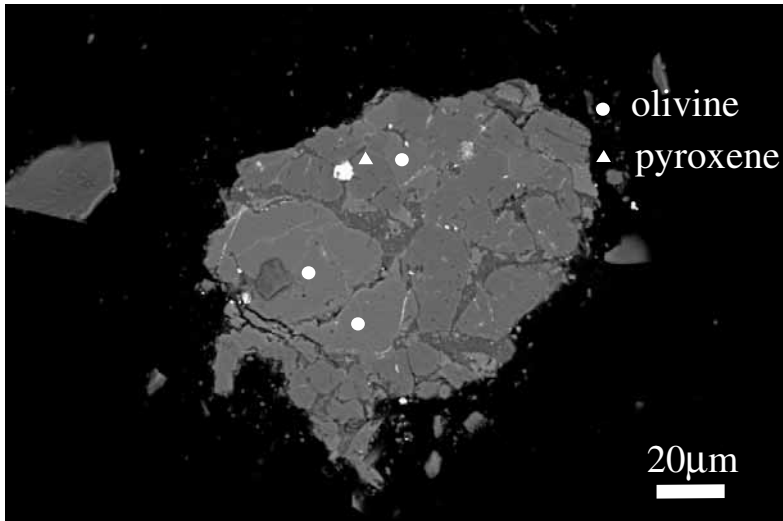
wt %	tr	kam
Ni		
Fe		
Mn		
Co		
Cr		
S		
P		
Total		



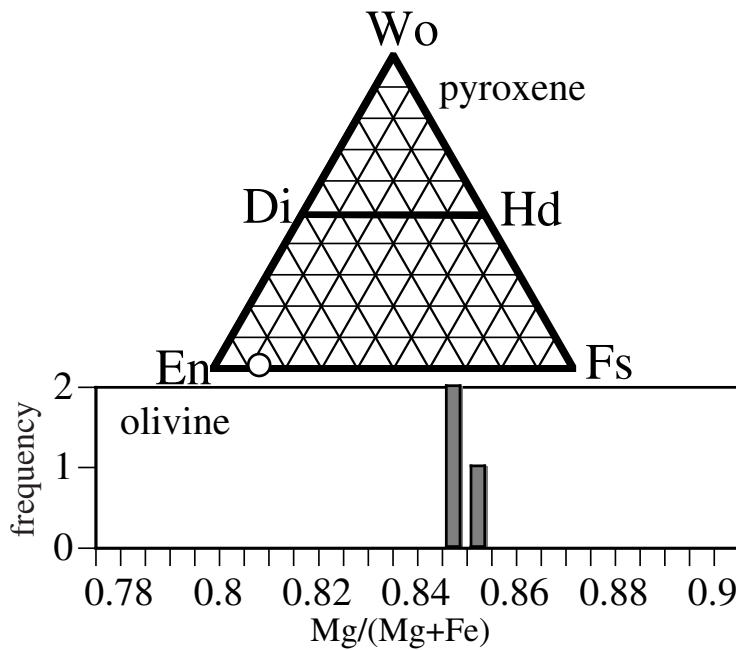
wt%	ol	low-Ca px	high-Ca px
SiO ₂	39.6	56.3	
TiO ₂	0.0	0.1	
Al ₂ O ₃	0.1	0.2	
FeO	14.0	8.9	
MnO	0.5	0.6	
MgO	45.6	32.5	
CaO	0.1	0.4	
Na ₂ O	0.4	0.1	
K ₂ O	0.0	0.0	
Cr ₂ O ₃	0.1	0.2	
NiO	0.0	0.0	
P ₂ O ₅	0.1	0.0	
SO ₃	0.1	0.1	
total	100.5	99.5	



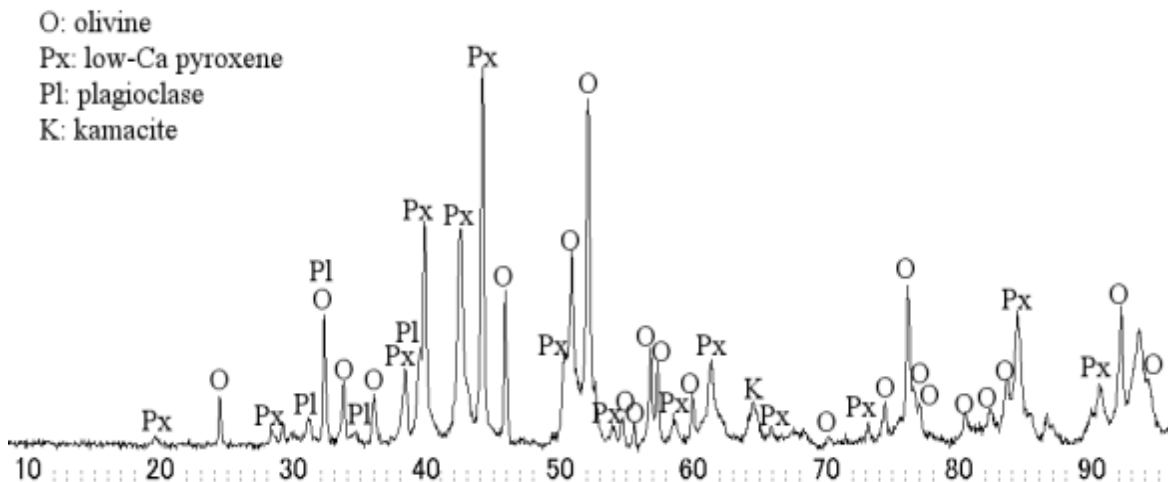
2AC5



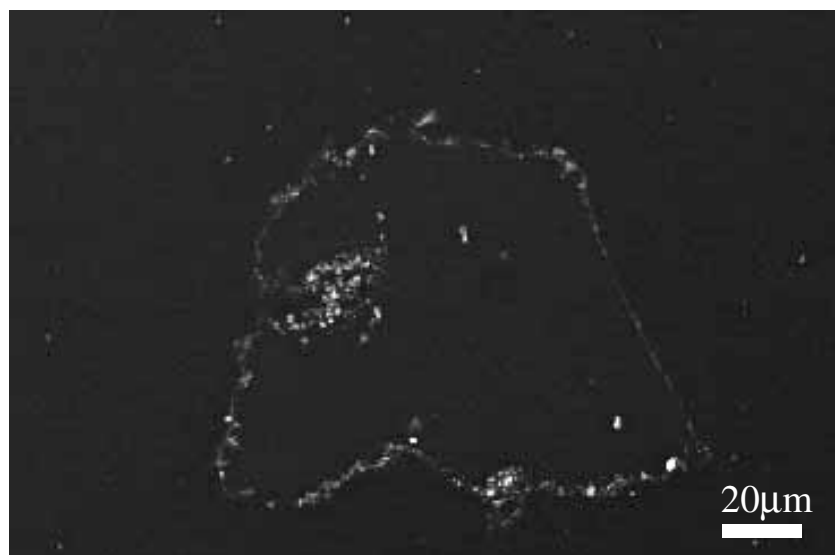
wt %	tr	kam
Ni		
Fe		
Mn		
Co		
Cr		
S		
P		
Total		



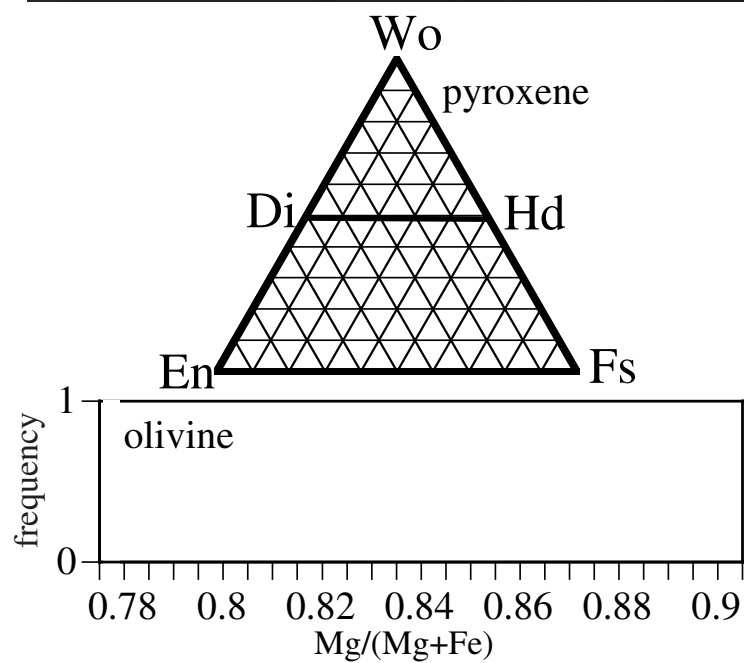
wt%	low-Ca high-Ca	
	ol	px
SiO ₂	39.6	57.3
TiO ₂	0.0	0.2
Al ₂ O ₃	0.0	0.3
FeO	14.9	9.0
MnO	0.5	0.5
MgO	46.0	33.2
CaO	0.0	0.4
Na ₂ O	0.0	0.0
K ₂ O	0.0	0.0
Cr ₂ O ₃	0.0	0.1
NiO	0.0	0.0
P ₂ O ₅	0.1	0.0
SO ₃	0.0	0.0
total	101.0	100.9



2AC6

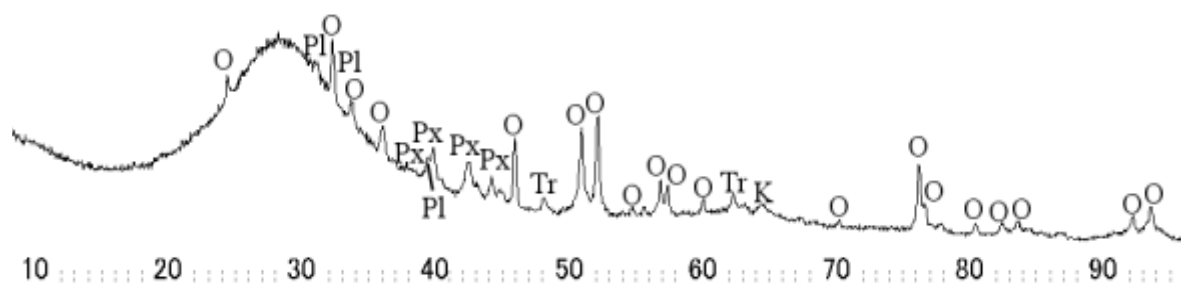


wt %	tr	kam
Ni		
Fe		
Mn		
Co		
Cr		
S		
P		
Total		



wt%	ol	low-Ca px	high-Ca px
SiO ₂			
TiO ₂			
Al ₂ O ₃			
FeO			
MnO			
MgO			
CaO			
Na ₂ O			
K ₂ O			
Cr ₂ O ₃			
NiO			
P ₂ O ₅			
SO ₃			
total			

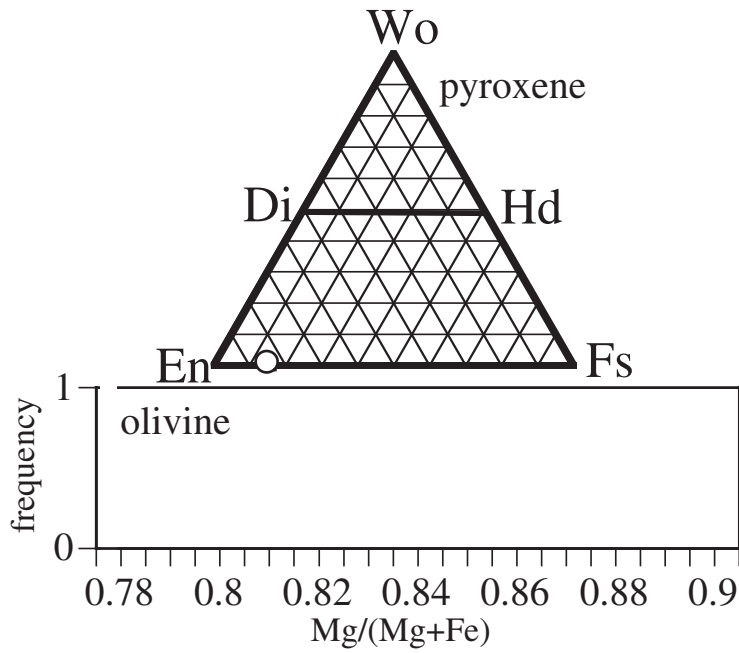
O: olivine
 Px: low-Ca pyroxene
 Pl: plagioclase
 Tr: troilite



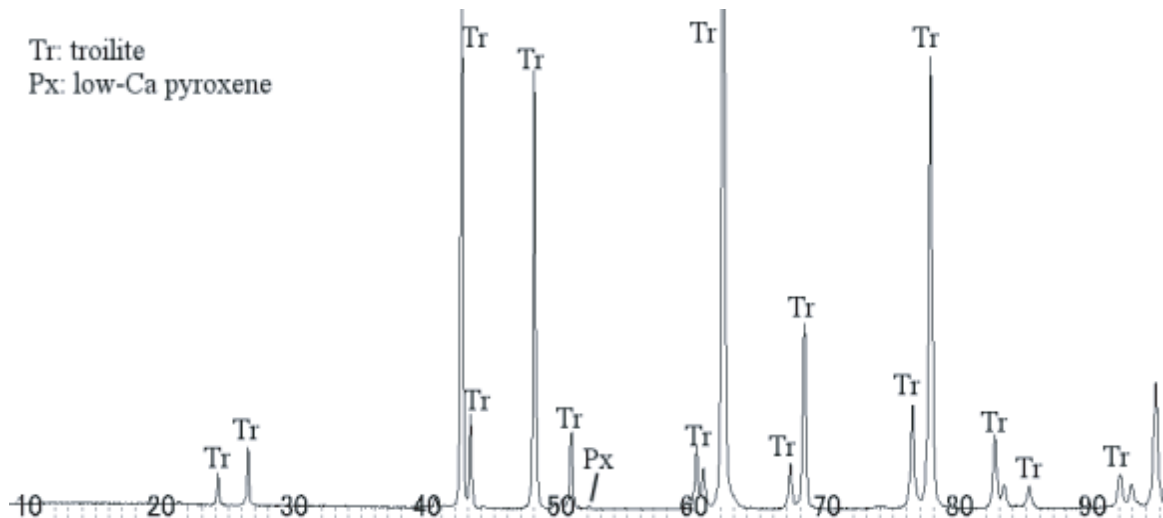
2AC7



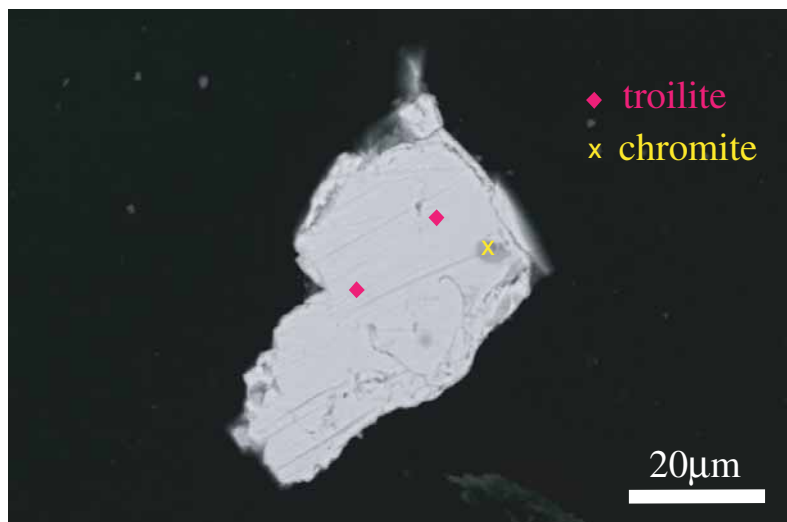
wt %	tr	kam
Ni	0.0	
Fe	63.5	
Mn	0.1	
Co	0.0	
Cr	0.0	
S	36.8	
P	0.0	
Total	100.5	



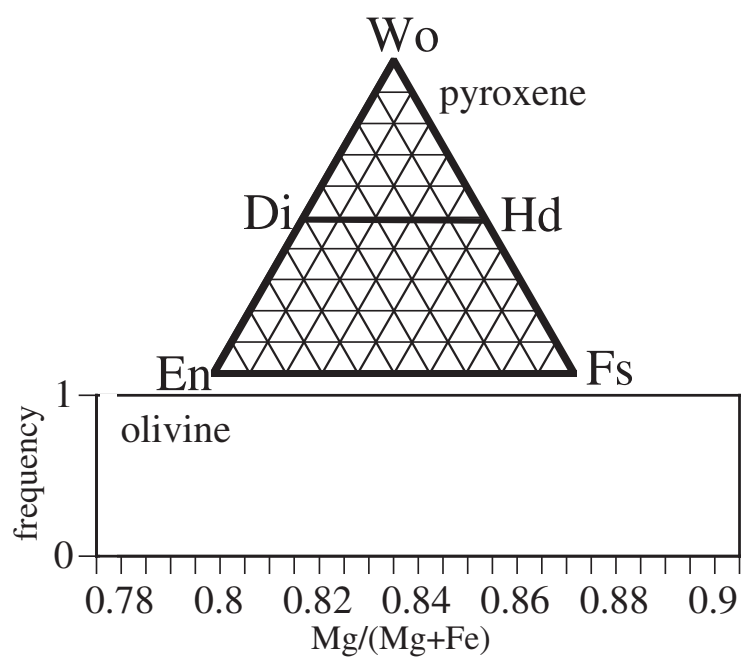
wt%	ol	low-Ca px	high-Ca px
SiO ₂		55.9	
TiO ₂		0.1	
Al ₂ O ₃		0.1	
FeO		10.2	
MnO		0.6	
MgO		32.3	
CaO		0.4	
Na ₂ O		0.1	
K ₂ O		0.0	
Cr ₂ O ₃		0.1	
NiO		0.0	
P ₂ O ₅		0.0	
SO ₃		0.1	
total		99.9	



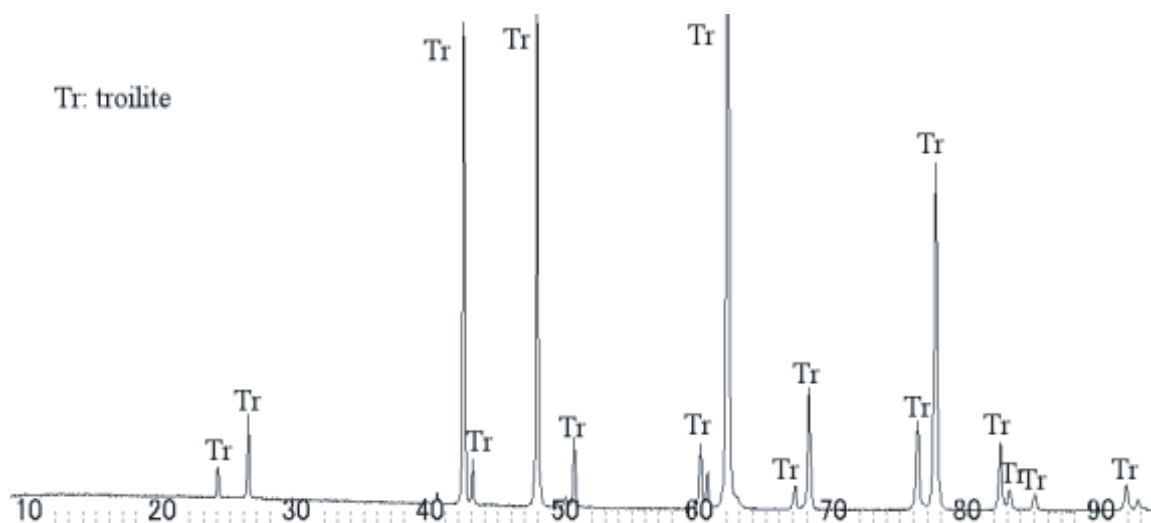
2AC8



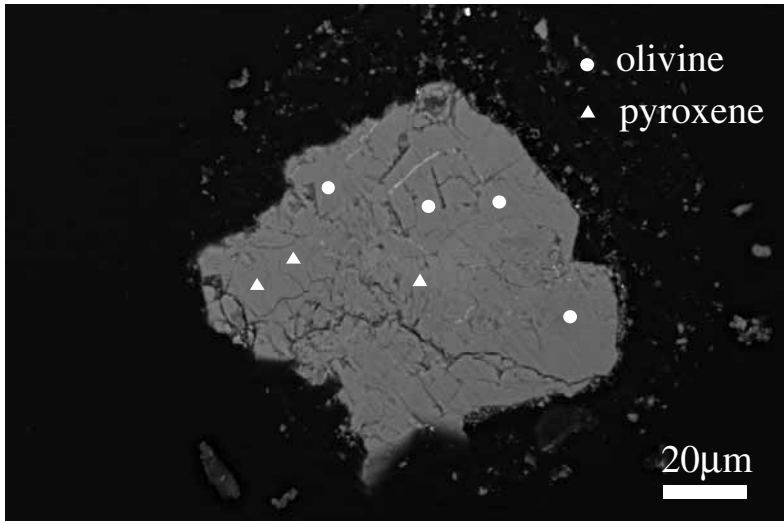
wt %	tr	kam
Ni	0.0	
Fe	62.6	
Mn	0.0	
Co	0.0	
Cr	0.0	
S	36.8	
P	0.0	
Total	99.4	



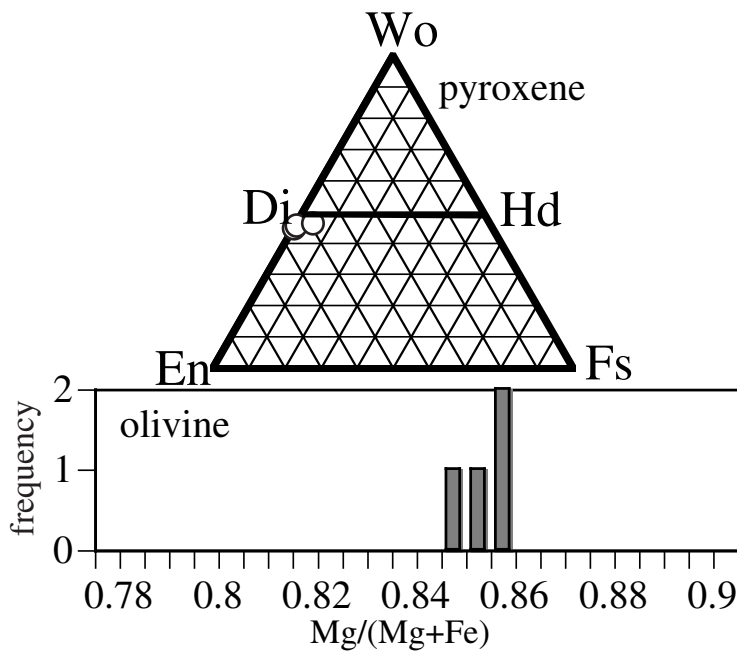
wt%	ol	low-Ca px	high-Ca px
SiO ₂			
TiO ₂			
Al ₂ O ₃			
FeO			
MnO			
MgO			
CaO			
Na ₂ O			
K ₂ O			
Cr ₂ O ₃			
NiO			
P ₂ O ₅			
SO ₃			
total			



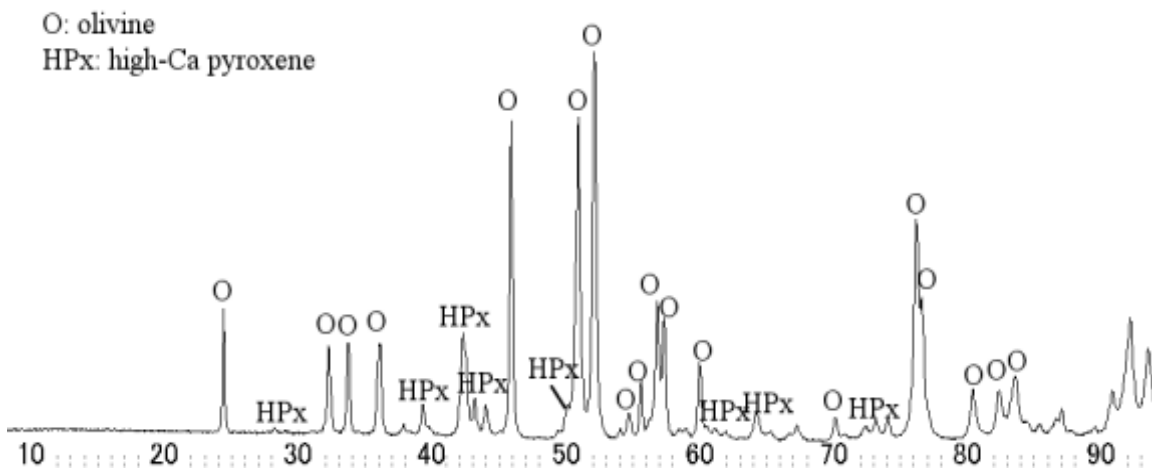
2AC9



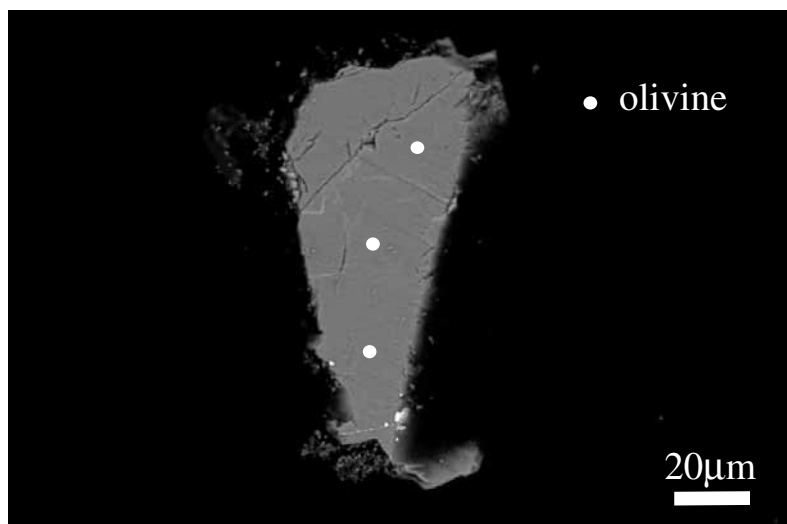
	wt %	tr	kam
Ni			
Fe			
Mn			
Co			
Cr			
S			
P			
Total			



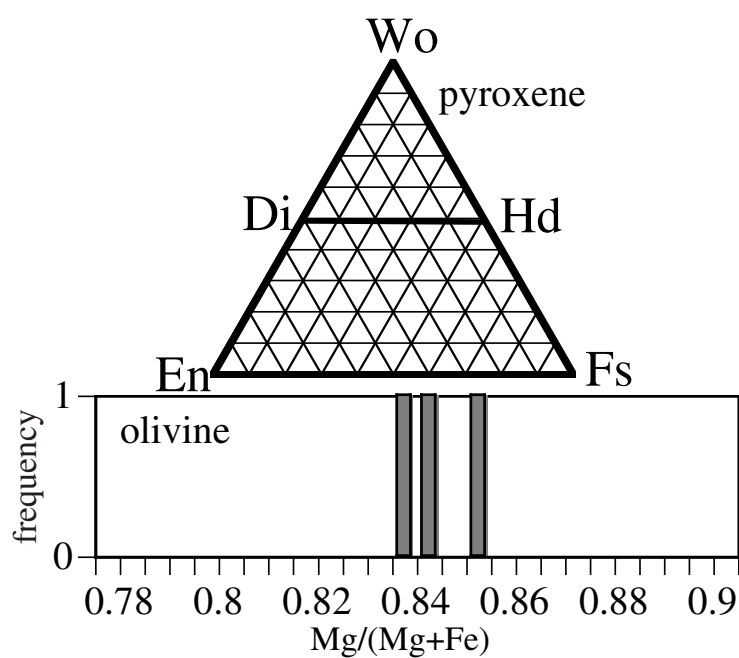
wt%	ol	low-Ca px	high-Ca px
SiO ₂	39.6		50.8
TiO ₂	0.0		1.4
Al ₂ O ₃	0.0		5.2
FeO	14.0		0.7
MnO	0.4		0.0
MgO	45.6		18.7
CaO	0.0		21.8
Na ₂ O	0.0		0.2
K ₂ O	0.0		0.0
Cr ₂ O ₃	0.0		0.9
NiO	0.1		0.0
P ₂ O ₅	0.0		0.0
SO ₃	0.0		0.0
total	99.8		99.6



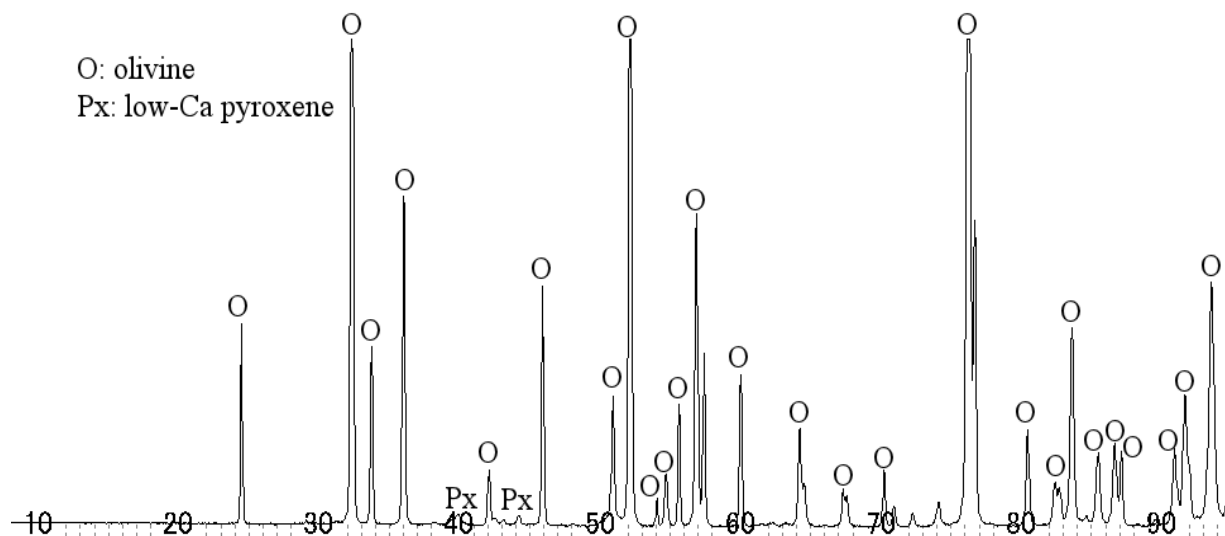
2AC10



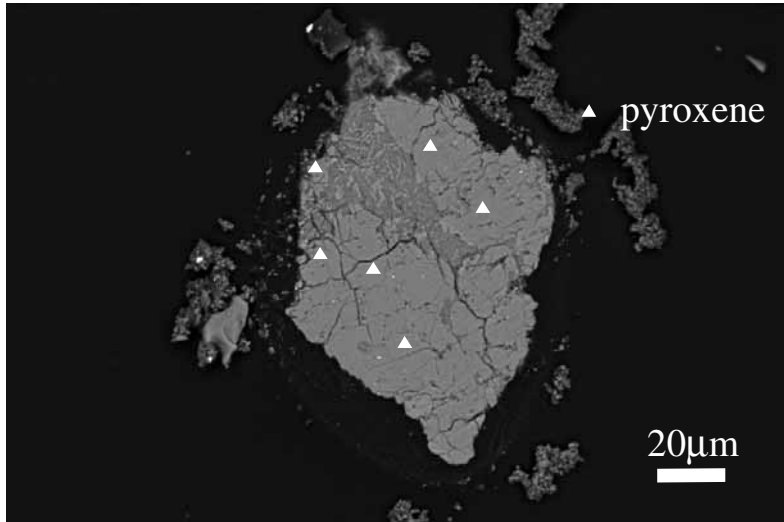
wt %	tr	kam
Ni		
Fe		
Mn		
Co		
Cr		
S		
P		
Total		



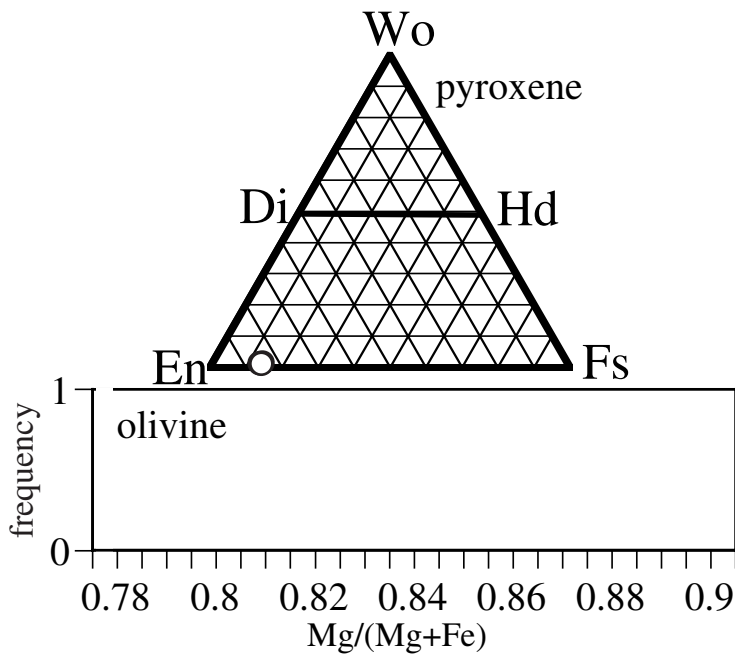
wt%	ol	low-Ca px	high-Ca px
SiO ₂	39.1		
TiO ₂	0.0		
Al ₂ O ₃	0.0		
FeO	14.8		
MnO	0.4		
MgO	44.8		
CaO	0.0		
Na ₂ O	0.0		
K ₂ O	0.0		
Cr ₂ O ₃	0.0		
NiO	0.0		
P ₂ O ₅	0.1		
SO ₃	0.0		
total	99.3		



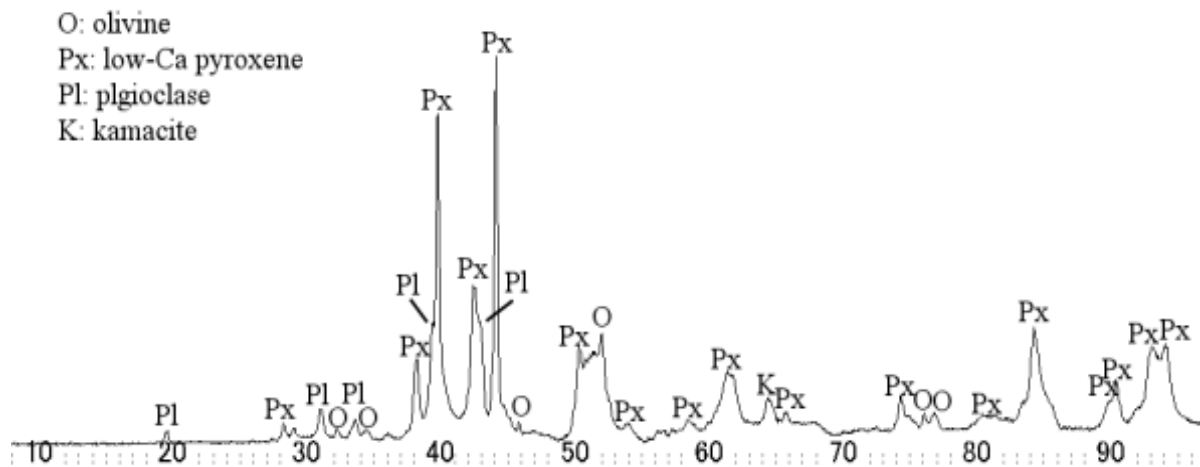
2AC11



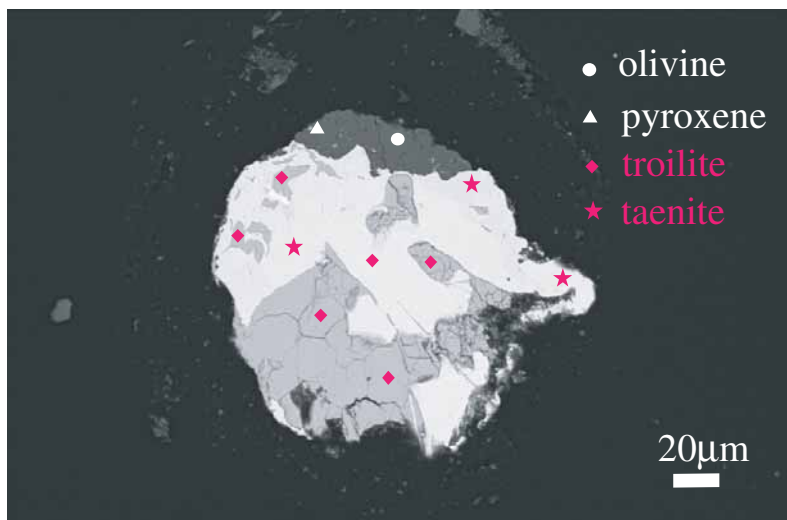
wt %	tr	kam
Ni		
Fe		
Mn		
Co		
Cr		
S		
P		
Total		



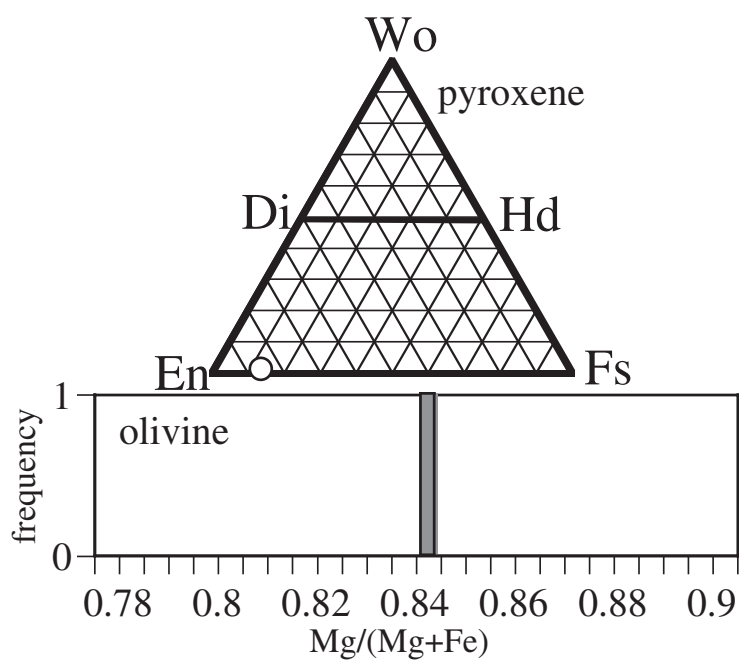
wt%	ol	low-Ca px	high-Ca px
SiO ₂		56.3	
TiO ₂		0.2	
Al ₂ O ₃		0.1	
FeO		9.8	
MnO		0.5	
MgO		32.4	
CaO		0.4	
Na ₂ O		0.0	
K ₂ O		0.0	
Cr ₂ O ₃		0.2	
NiO		0.0	
P ₂ O ₅		0.1	
SO ₃		0.0	
total		100.0	



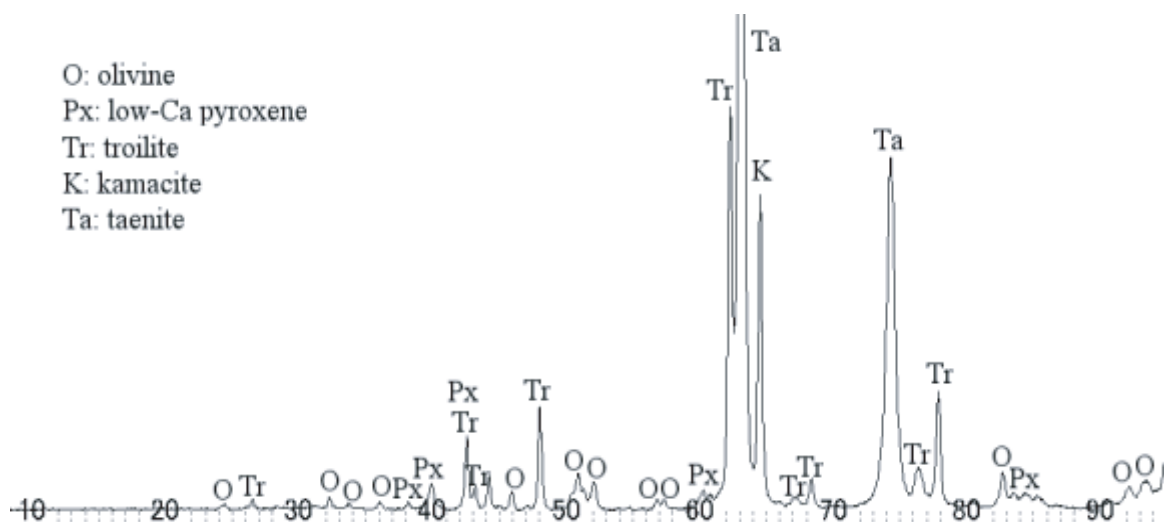
2AC12



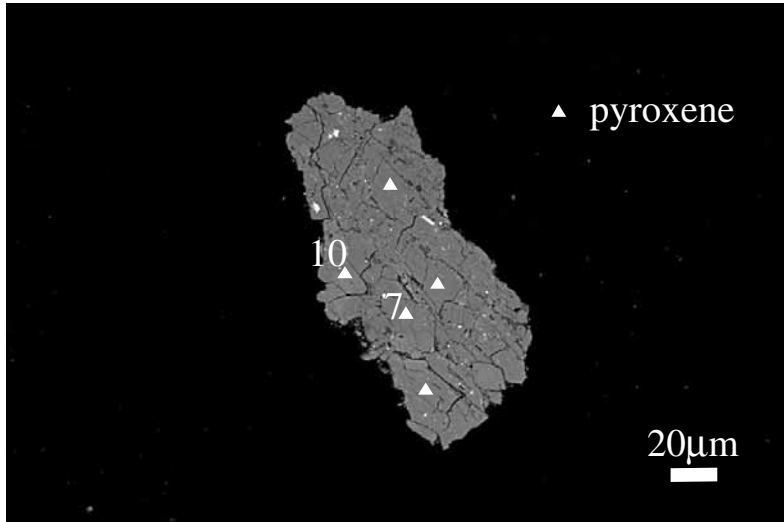
wt %	tr	tae
Ni	0.9	50.6
Fe	62.9	49.4
Mn	0.0	0.0
Co	0.0	0.1
Cr	0.0	0.0
S	36.0	0.0
P	0.0	0.0
Total	99.9	100.2



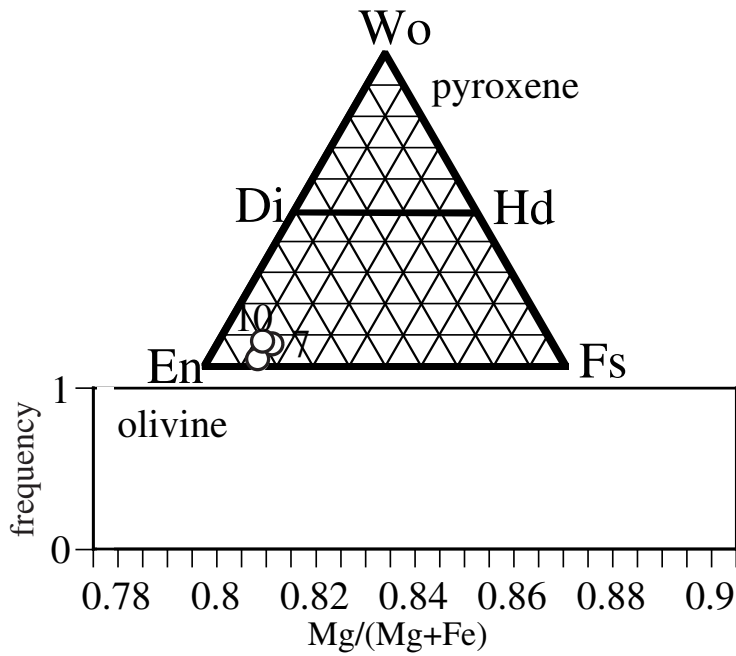
wt%	ol	low-Ca px	high-Ca px
SiO ₂	39.1	57.0	
TiO ₂	0.0	0.2	
Al ₂ O ₃	0.0	0.2	
FeO	15.4	9.5	
MnO	0.5	0.5	
MgO	45.2	32.9	
CaO	0.0	0.4	
Na ₂ O	0.0	0.1	
K ₂ O	0.0	0.0	
Cr ₂ O ₃	0.1	0.1	
NiO	0.1	0.0	
P ₂ O ₅	0.0	0.0	
SO ₃	0.1	0.1	
total	100.6	100.8	



2AC13

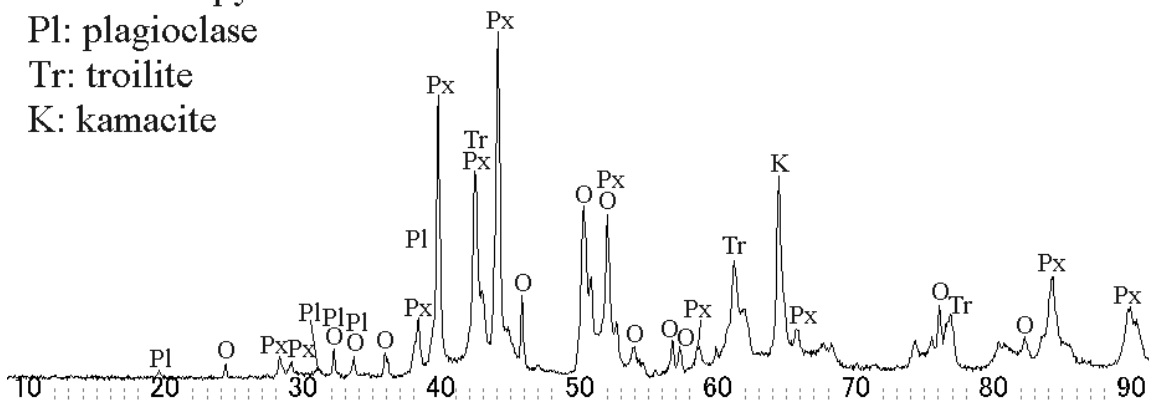


wt %	tr	kam
Ni		
Fe		
Mn		
Co		
Cr		
S		
P		
Total		

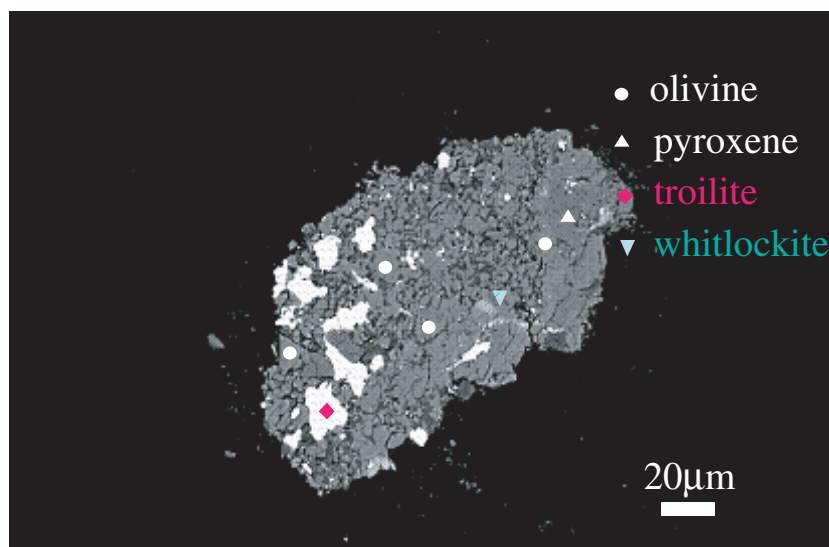


wt%	ol	low-Ca high-Ca	
		px	px
SiO ₂		55.8	54.2
TiO ₂		0.2	0.1
Al ₂ O ₃		0.4	1.2
FeO		9.6	10.4
MnO		0.7	0.4
MgO		31.7	28.7
CaO		0.9	3.4
Na ₂ O		0.1	0.1
K ₂ O		0.0	0.0
Cr ₂ O ₃		0.2	0.5
NiO		0.0	0.0
P ₂ O ₅		0.1	0.1
SO ₃		0.0	0.0
total		99.5	99.1

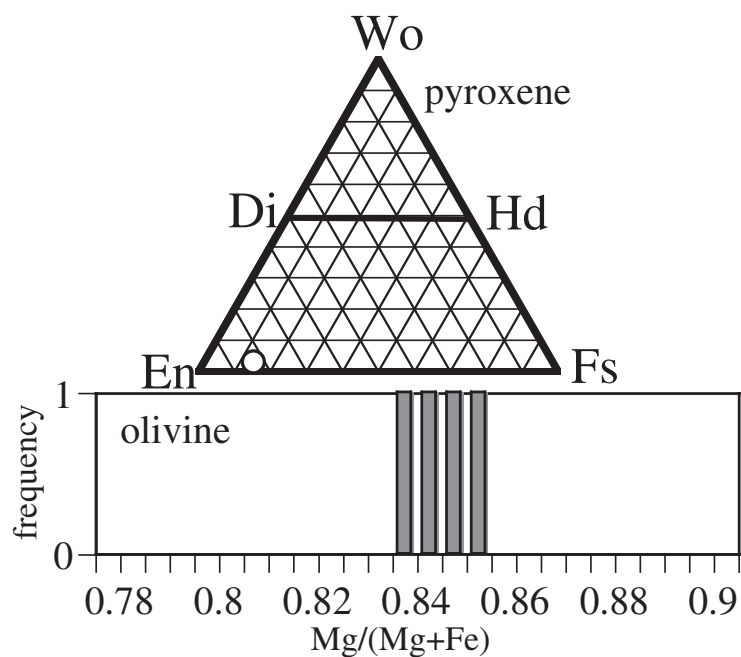
O: olivine
 Px: low Ca pyroxene
 Pl: plagioclase
 Tr: troilite
 K: kamacite



2AC14



wt %	tr	kam
Ni	0.0	
Fe	63.1	
Mn	0.0	
Co	0.0	
Cr	0.0	
S	37.7	
P	0.0	
Total	100.8	



wt%	ol	low-Ca px	high-Ca px
SiO ₂	39.3	55.8	
TiO ₂	0.0	0.4	
Al ₂ O ₃	0.1	0.7	
FeO	14.0	9.9	
MnO	0.6	0.6	
MgO	45.2	32.0	
CaO	0.1	1.3	
Na ₂ O	0.2	0.1	
K ₂ O	0.0	0.0	
Cr ₂ O ₃	0.1	0.4	
NiO	0.0	0.0	
P ₂ O ₅	0.3	0.0	
SO ₃	0.0	0.0	
total	99.8	101.2	

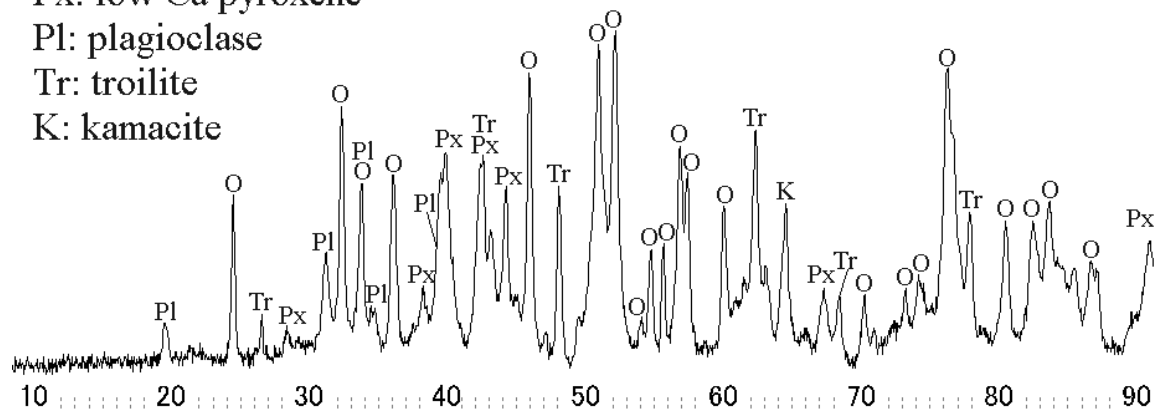
O: olivine

Px: low Ca pyroxene

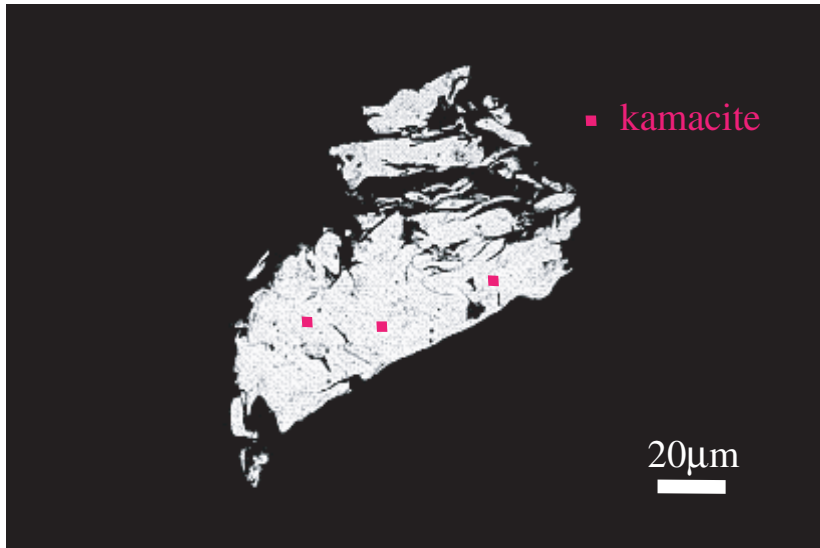
Pl: plagioclase

Tr: troilite

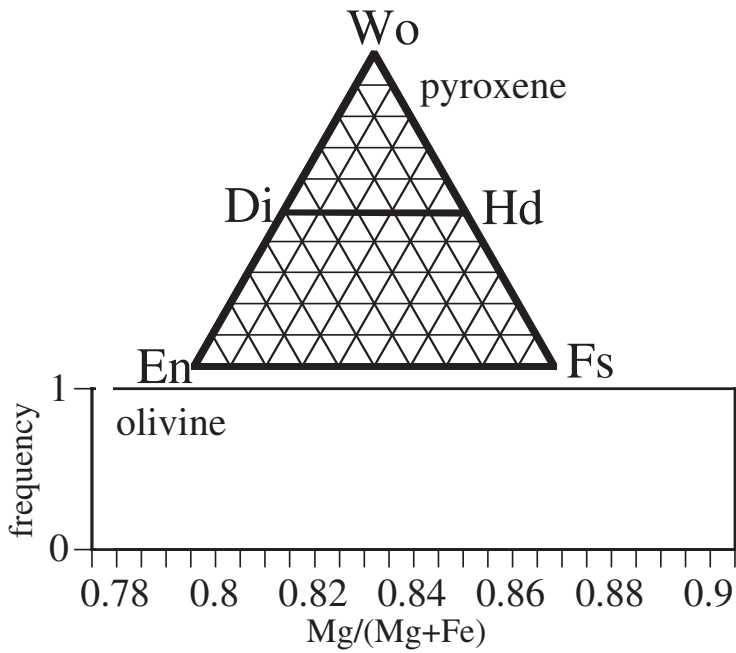
K: kamacite



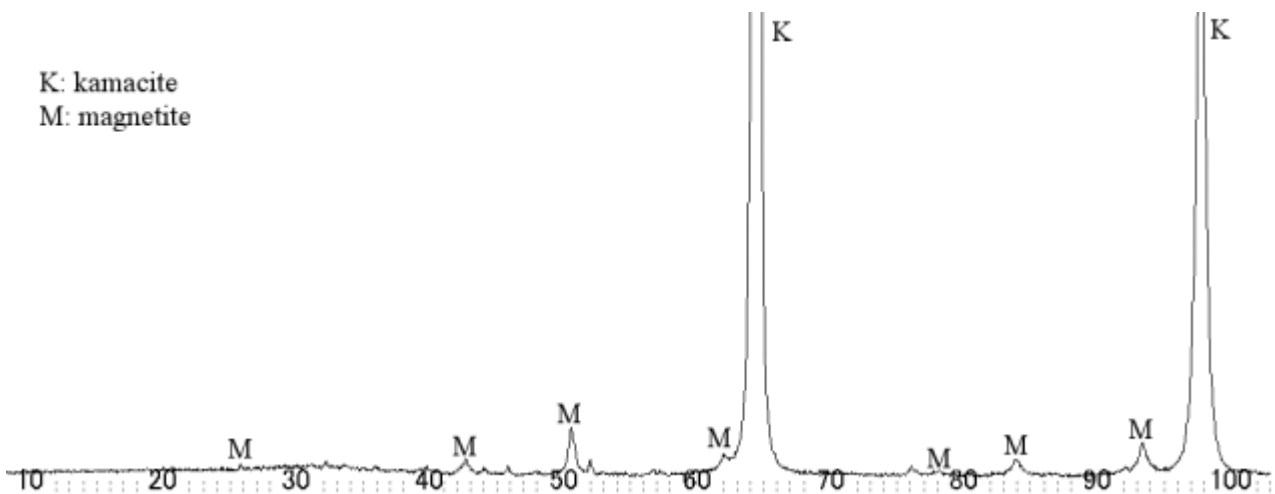
2AC15



wt %	tr	kam
Ni		0.1
Fe		99.1
Mn		0.9
Co		0.0
Cr		0.1
S		0.0
P		0.0
Total		100.2

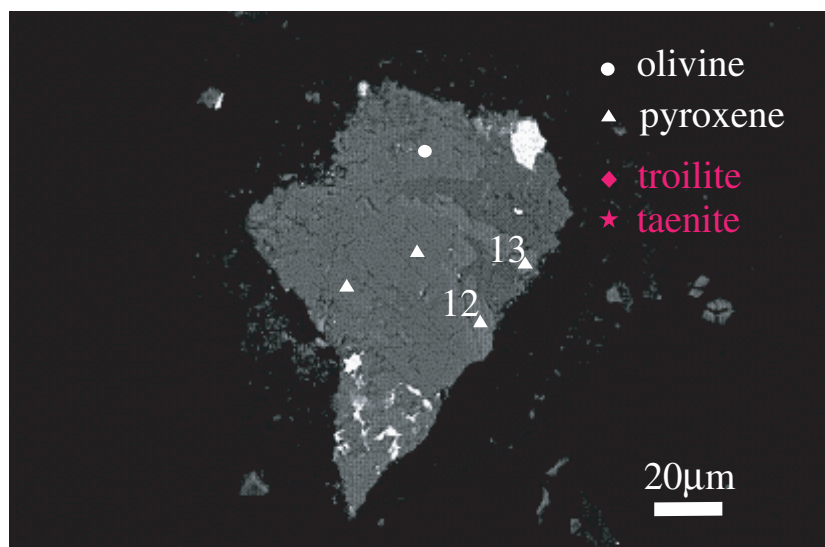


wt%	ol	low-Ca px	high-Ca px
SiO ₂			
TiO ₂			
Al ₂ O ₃			
FeO			
MnO			
MgO			
CaO			
Na ₂ O			
K ₂ O			
Cr ₂ O ₃			
NiO			
P ₂ O ₅			
SO ₃			
total			

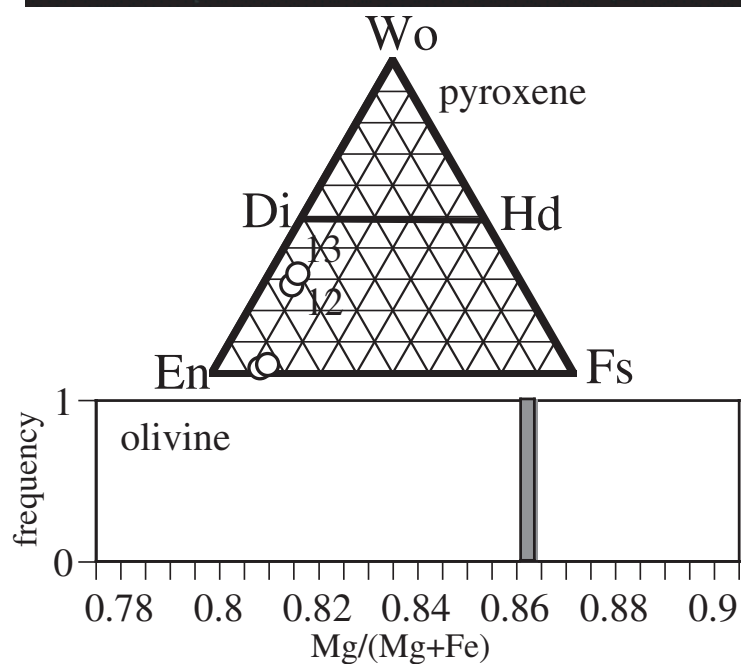


K: kamacite
M: magnetite

2AC16



wt %	tr	kam
Ni		
Fe		
Mn		
Co		
Cr		
S		
P		
Total		



wt%	ol	low-Ca px	high-Ca px
SiO ₂	40.5	56.4	54.0
TiO ₂	0.0	0.1	0.2
Al ₂ O ₃	0.0	0.2	1.1
FeO	13.3	9.7	5.4
MnO	0.5	0.5	0.3
MgO	45.6	30.8	22.2
CaO	0.1	1.2	13.5
Na ₂ O	0.0	0.1	0.6
K ₂ O	0.0	0.0	0.0
Cr ₂ O ₃	0.1	0.4	1.8
NiO	0.0	0.1	0.0
P ₂ O ₅	0.0	0.0	0.1
SO ₃	0.0	0.1	0.0
total	100.2	99.6	99.1

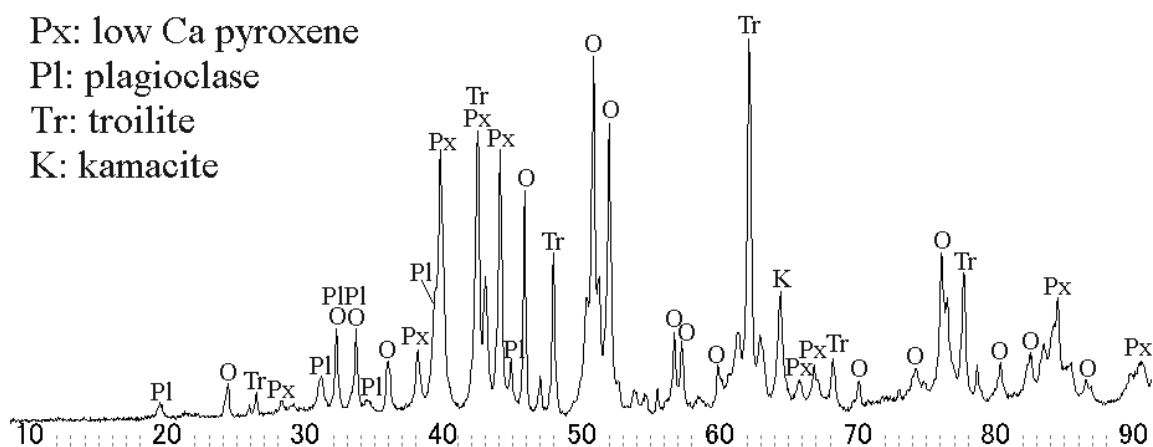
O: olivine

Px: low Ca pyroxene

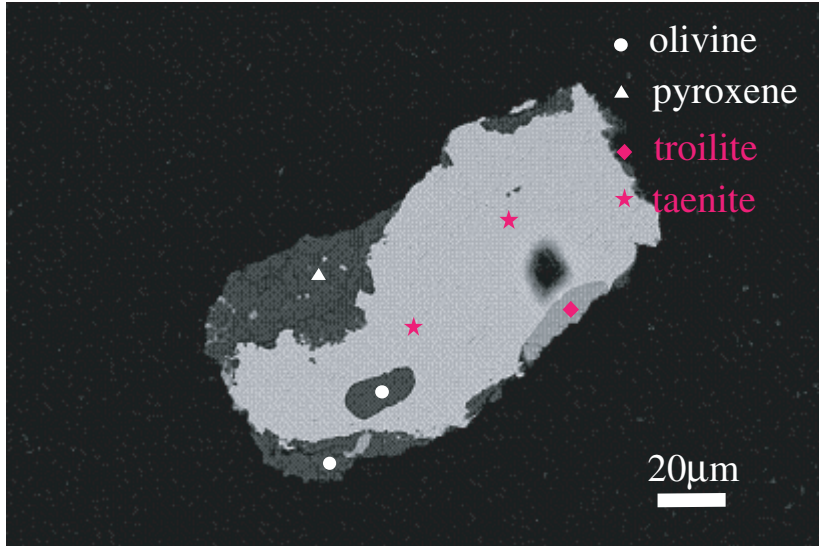
Pl: plagioclase

Tr: troilite

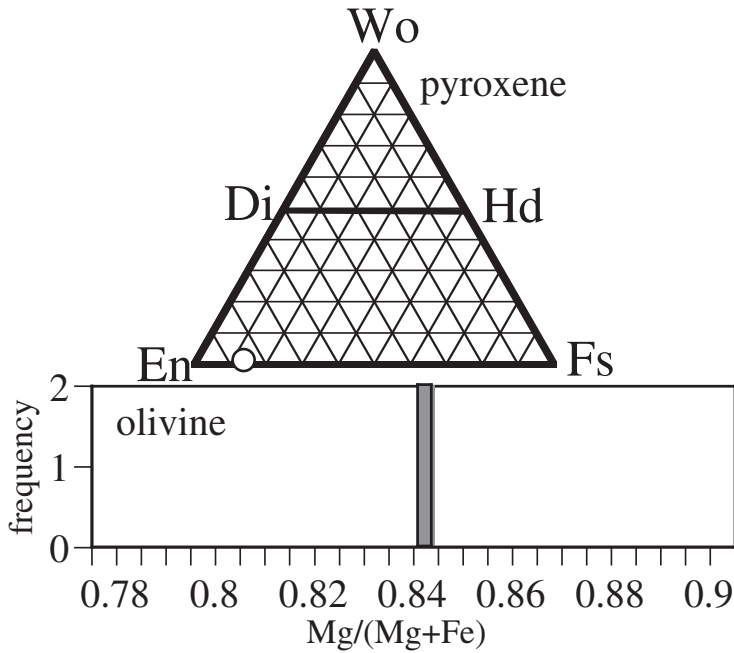
K: kamacite



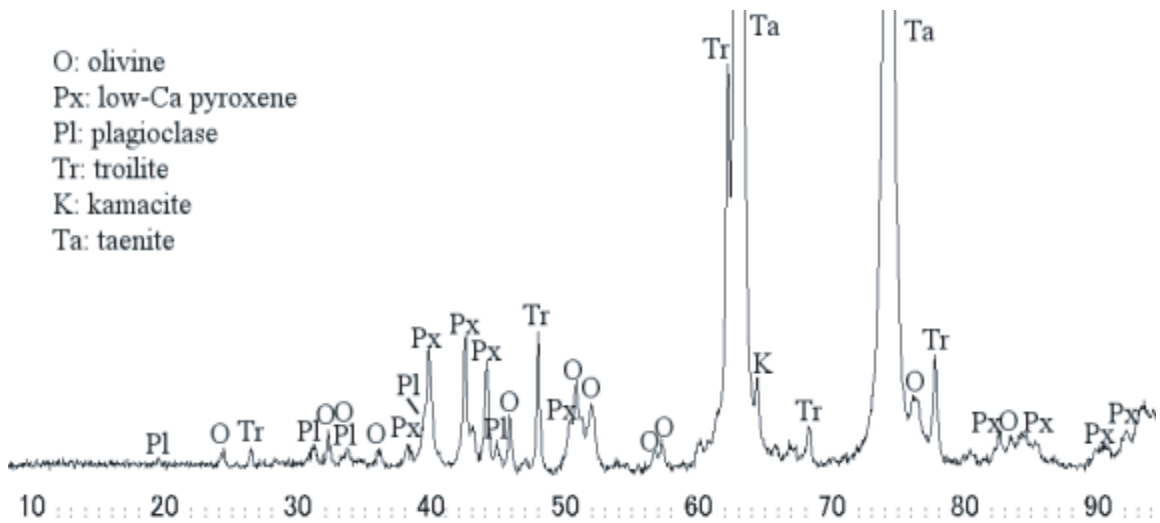
2AC17



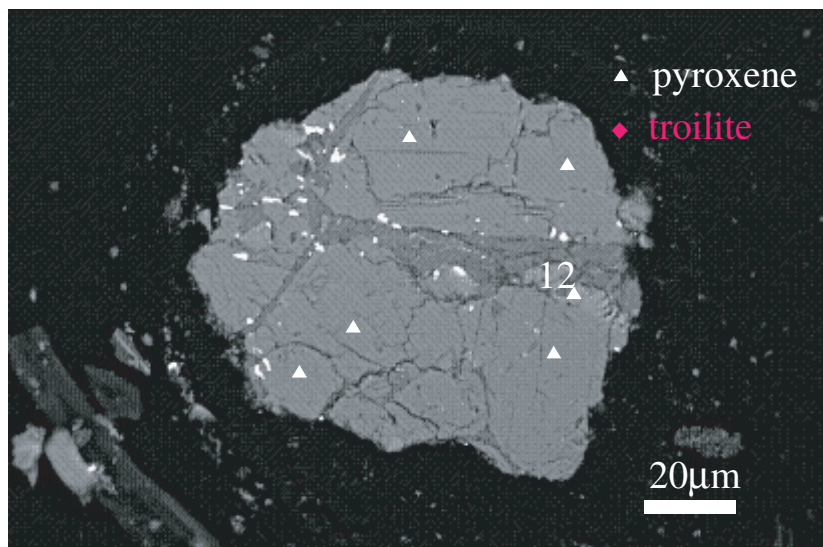
wt %	tr	tae
Ni	0.9	50.2
Fe	62.2	50.0
Mn	0.0	0.0
Co	0.0	0.1
Cr	0.0	0.0
S	37.1	0.0
P	0.0	0.0
Total	100.3	100.2



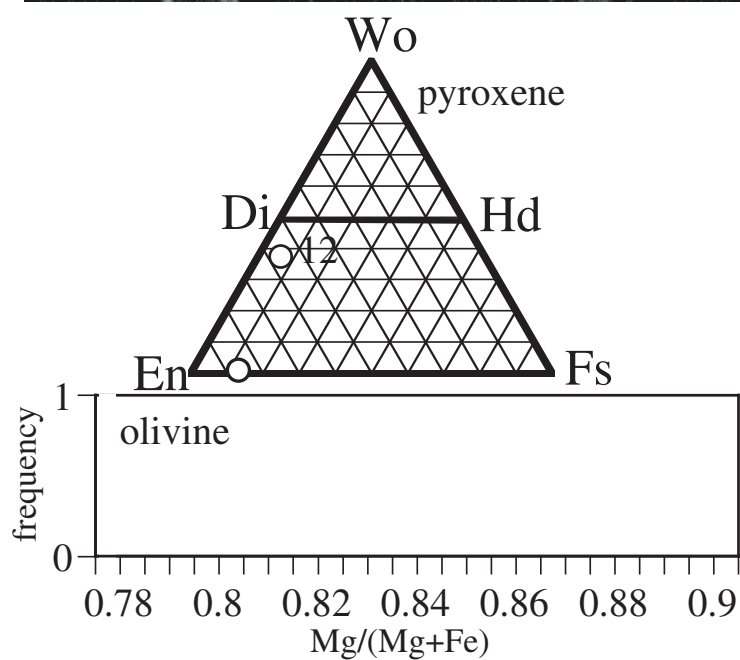
wt%	ol	low-Ca px	high-Ca px
SiO ₂	39.6	56.2	
TiO ₂	0.0	0.3	
Al ₂ O ₃	0.0	0.2	
FeO	15.4	9.2	
MnO	0.5	0.7	
MgO	45.3	32.2	
CaO	0.0	0.4	
Na ₂ O	0.0	0.1	
K ₂ O	0.0	0.0	
Cr ₂ O ₃	0.0	0.2	
NiO	0.2	0.0	
P ₂ O ₅	0.1	0.0	
SO ₃	0.0	0.0	
total	101.2	99.4	



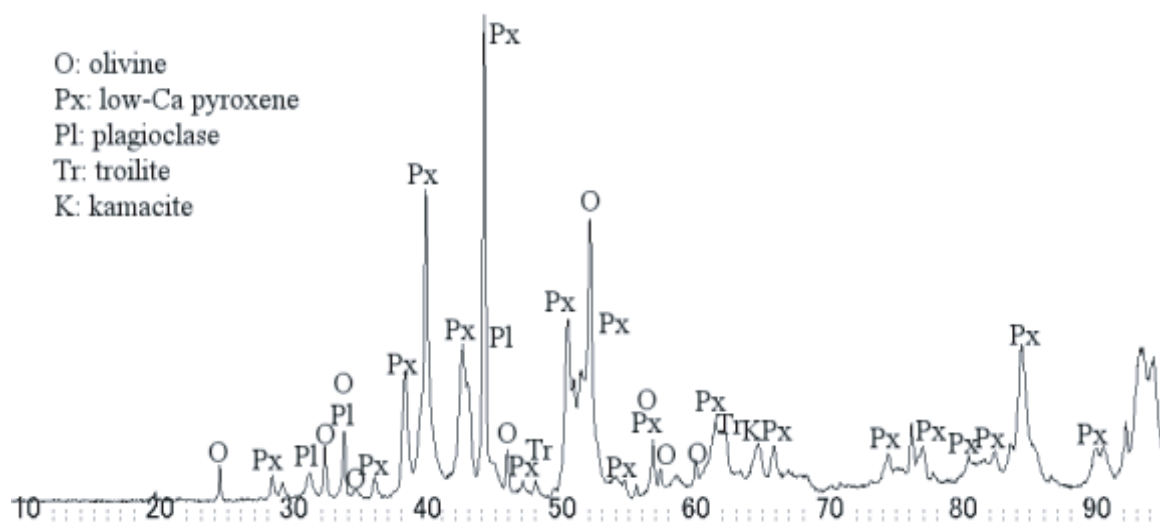
2AC18



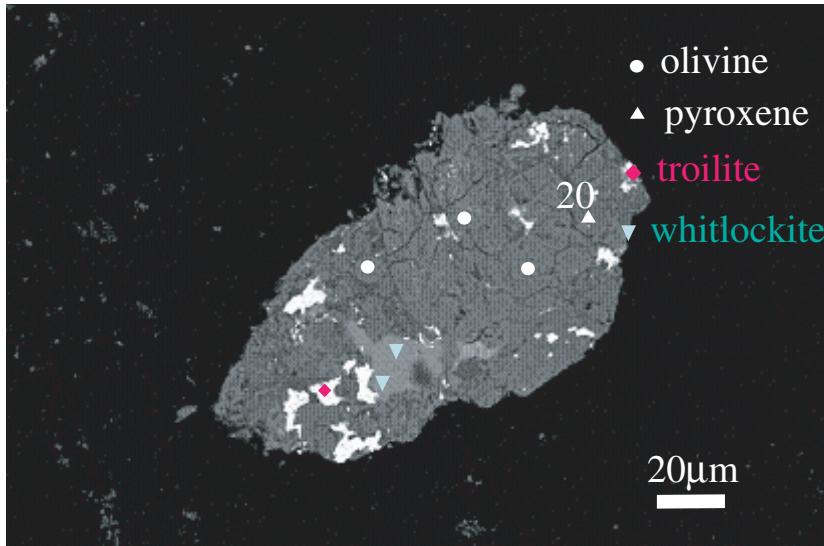
wt %	tr	kam
Ni		
Fe		
Mn		
Co		
Cr		
S		
P		
Total		



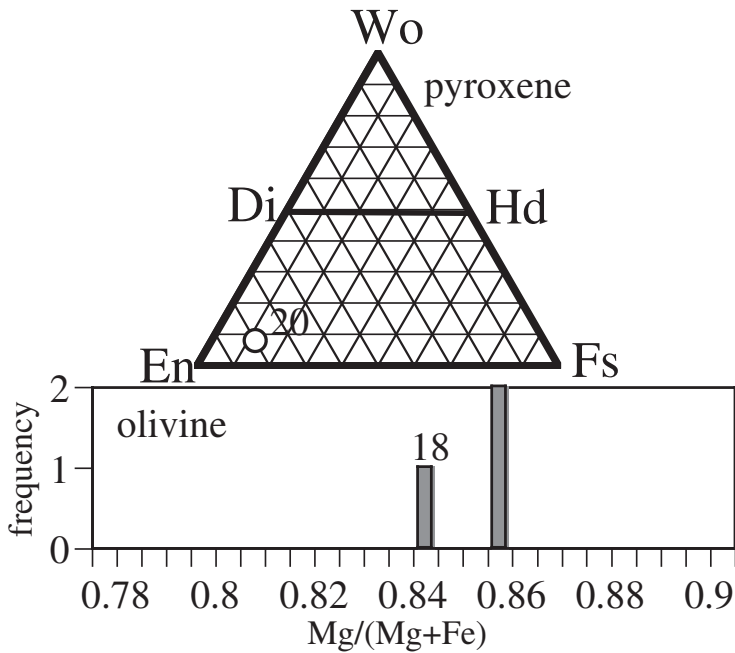
wt%	ol	low-Ca px	high-Ca px
SiO ₂		56.4	53.0
TiO ₂		0.1	0.5
Al ₂ O ₃		0.1	3.4
FeO		9.1	4.3
MnO		0.4	0.5
MgO		32.7	19.4
CaO		0.2	17.7
Na ₂ O		0.0	0.6
K ₂ O		0.0	0.0
Cr ₂ O ₃		0.1	1.7
NiO		0.0	0.0
P ₂ O ₅		0.0	0.0
SO ₃		0.0	0.0
total		99.3	101.2



2AC19

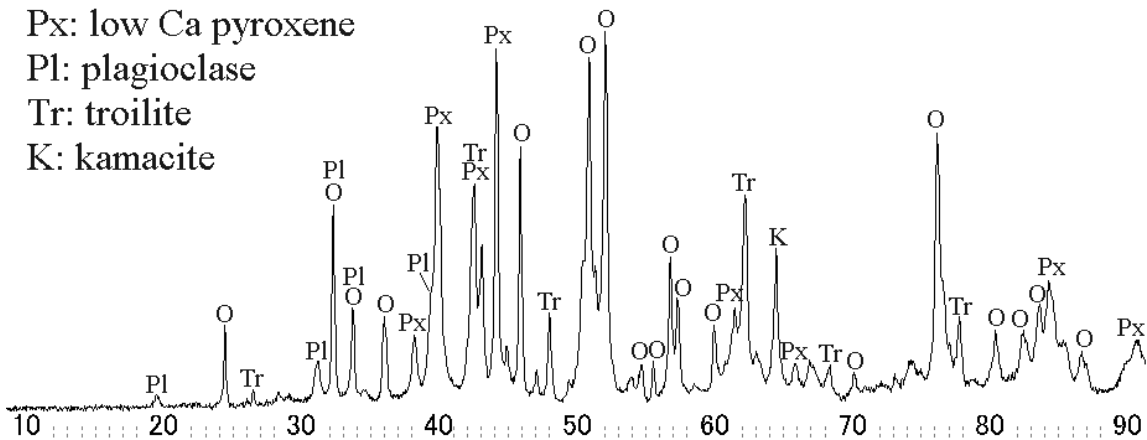


wt %	tr	kam
Ni	0.0	
Fe	63.6	
Mn	0.0	
Co	0.0	
Cr	0.1	
S	37.0	
P	0.0	
Total	100.6	

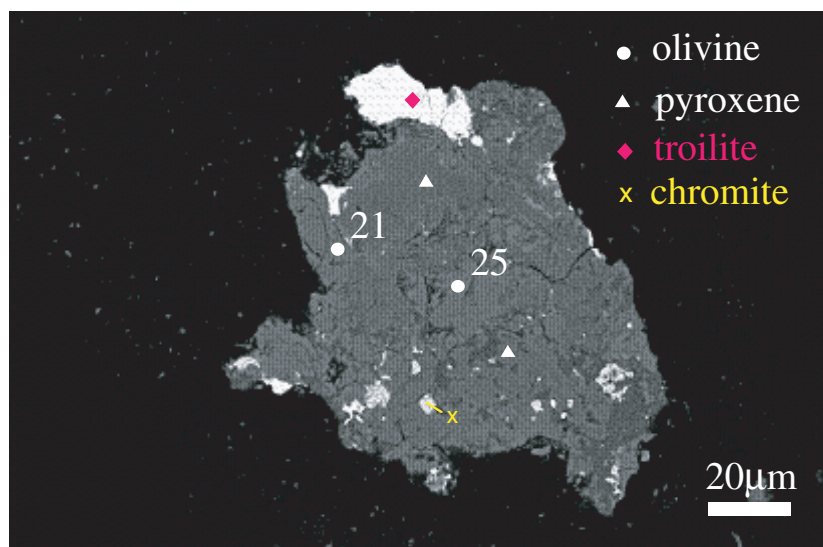


wt%	ol	low-Ca px	high-Ca px
SiO ₂	39.8		57.0
TiO ₂	0.0		0.2
Al ₂ O ₃	0.0		1.8
FeO	13.6		8.1
MnO	0.5		0.4
MgO	45.6		28.4
CaO	0.1		3.7
Na ₂ O	0.0		0.6
K ₂ O	0.0		0.0
Cr ₂ O ₃	0.0		0.2
NiO	0.0		0.0
P ₂ O ₅	0.1		0.0
SO ₃	0.0		0.4
total	99.6		100.8

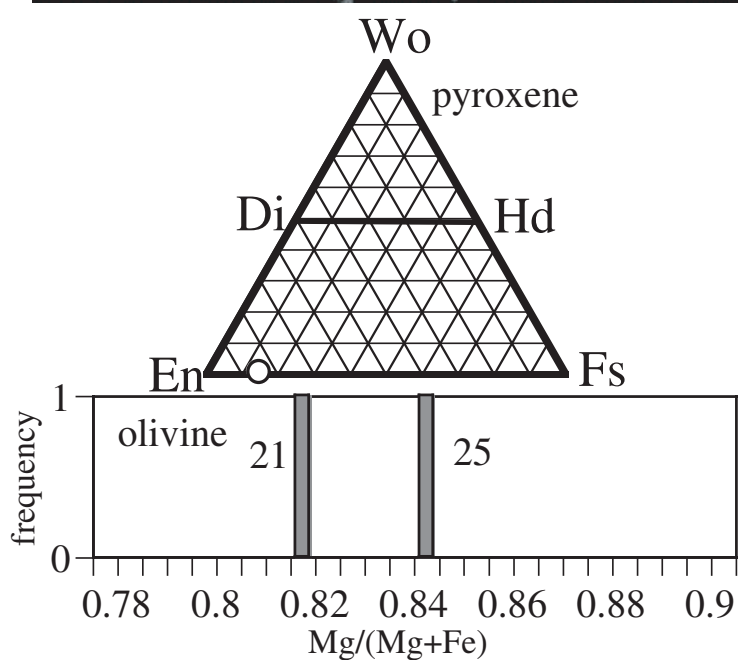
O: olivine
 Px: low Ca pyroxene
 Pl: plagioclase
 Tr: troilite
 K: kamacite



2AC20



wt %	tr	kam
Ni	0.0	
Fe	63.1	
Mn	0.0	
Co	0.0	
Cr	0.0	
S	37.4	
P	0.0	
Total	100.6	



wt%	ol	low-Ca px	high-Ca px
SiO ₂	39.4	56.2	
TiO ₂	0.0	0.1	
Al ₂ O ₃	0.0	0.1	
FeO	15.0	9.8	
MnO	0.5	0.5	
MgO	45.4	32.6	
CaO	0.0	0.5	
Na ₂ O	0.1	0.0	
K ₂ O	0.0	0.0	
Cr ₂ O ₃	0.0	0.2	
NiO	0.0	0.0	
P ₂ O ₅	0.0	0.0	
SO ₃	0.0	0.0	
total	100.4	100.0	

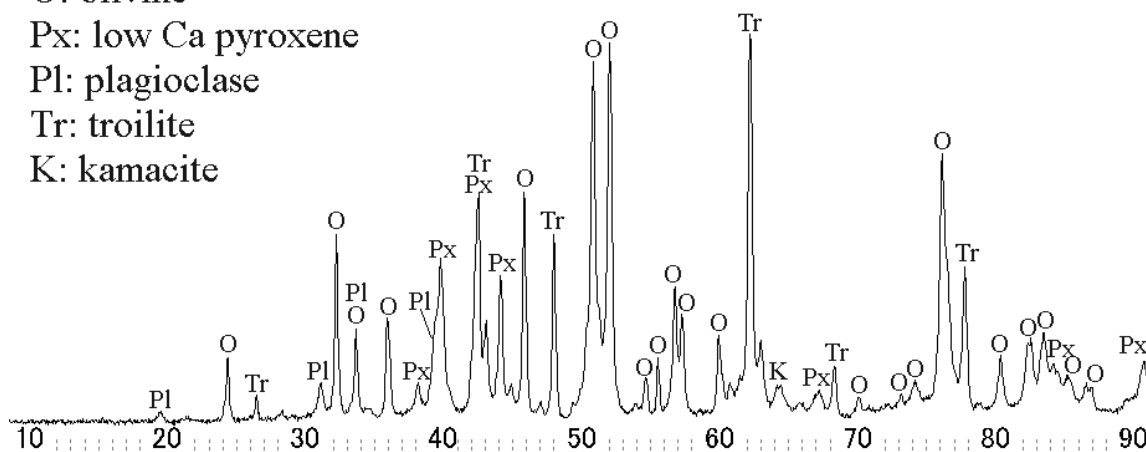
O: olivine

Px: low Ca pyroxene

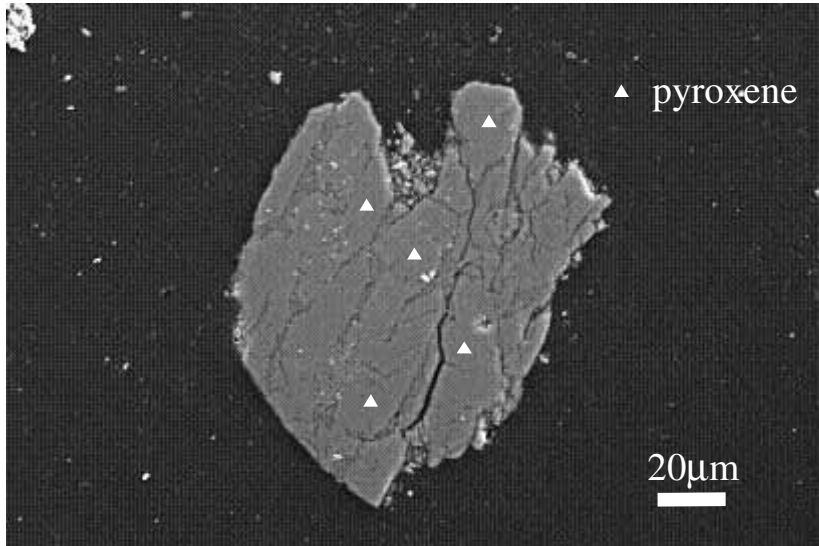
Pl: plagioclase

Tr: troilite

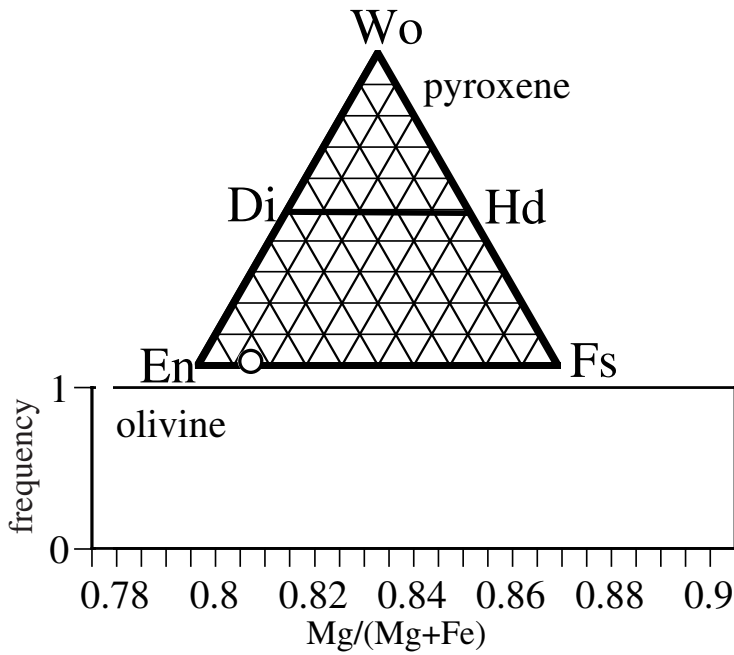
K: kamacite



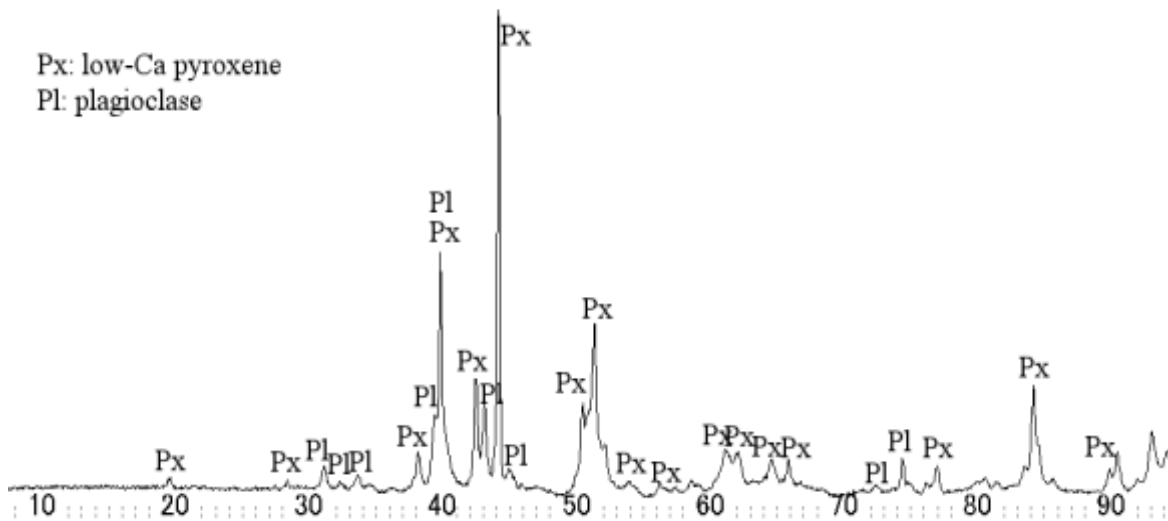
2AC21



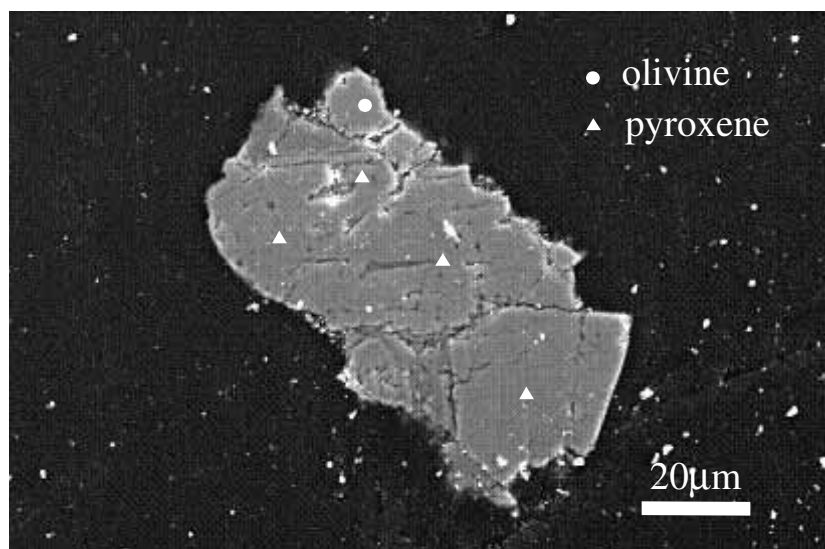
wt %	tr	kam
Ni		
Fe		
Mn		
Co		
Cr		
S		
P		
<hr/>		
Total		



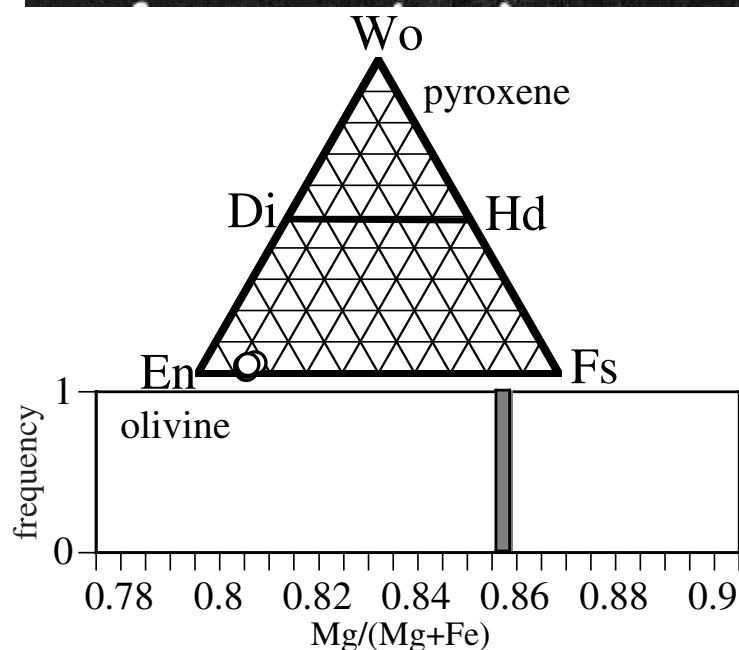
wt%	ol	low-Ca px	high-Ca px
SiO ₂		56.4	
TiO ₂		0.1	
Al ₂ O ₃		0.2	
FeO		9.6	
MnO		0.5	
MgO		32.1	
CaO		0.5	
Na ₂ O		0.0	
K ₂ O		0.0	
Cr ₂ O ₃		0.1	
NiO		0.0	
P ₂ O ₅		0.1	
SO ₃		0.0	
<hr/>			
total		99.6	



2AC22



wt %	tr	kam
Ni		
Fe		
Mn		
Co		
Cr		
S		
P		
Total		



wt%	ol	low-Ca px	high-Ca px
SiO ₂	39.5	56.4	
TiO ₂	0.0	0.1	
Al ₂ O ₃	0.0	0.6	
FeO	13.6	8.7	
MnO	0.5	0.5	
MgO	45.2	32.2	
CaO	0.0	0.9	
Na ₂ O	0.0	0.0	
K ₂ O	0.0	0.0	
Cr ₂ O ₃	0.0	0.4	
NiO	0.0	0.0	
P ₂ O ₅	0.0	0.0	
SO ₃	0.0	0.0	
total	99.0	99.8	

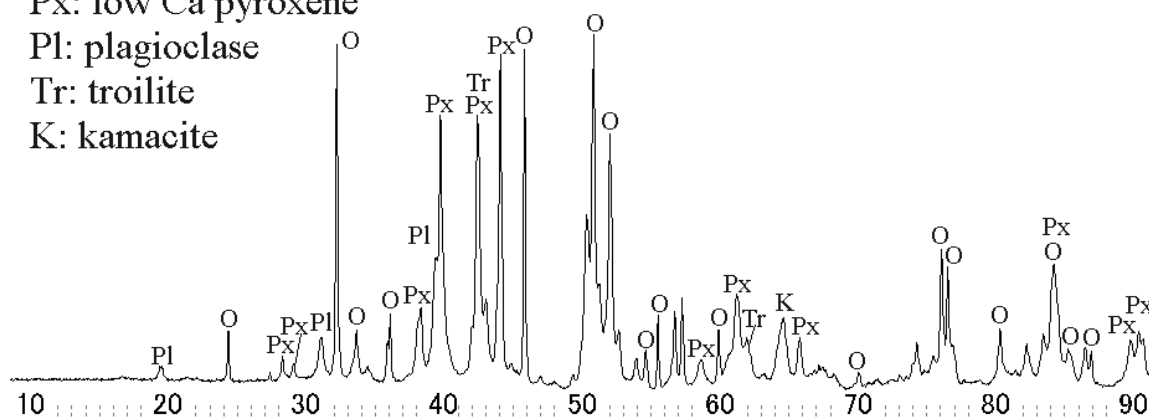
O: olivine

Px: low Ca pyroxene

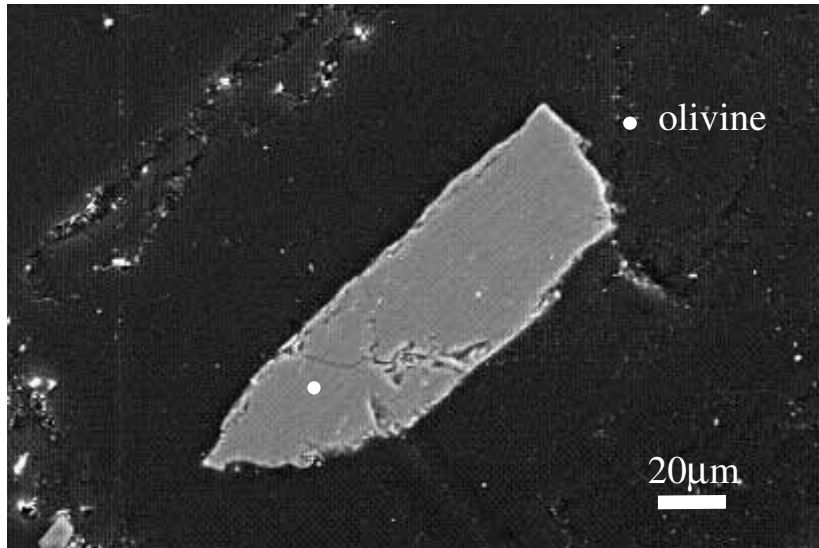
Pl: plagioclase

Tr: troilite

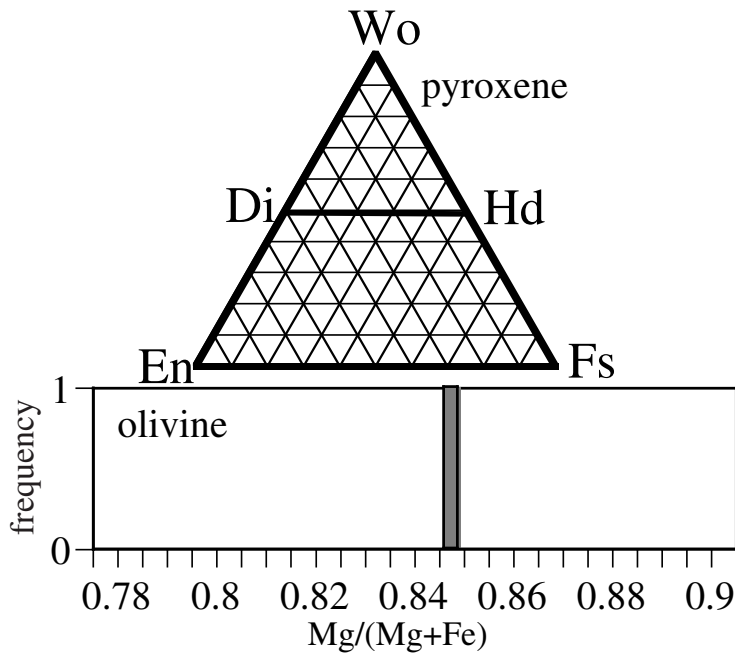
K: kamacite



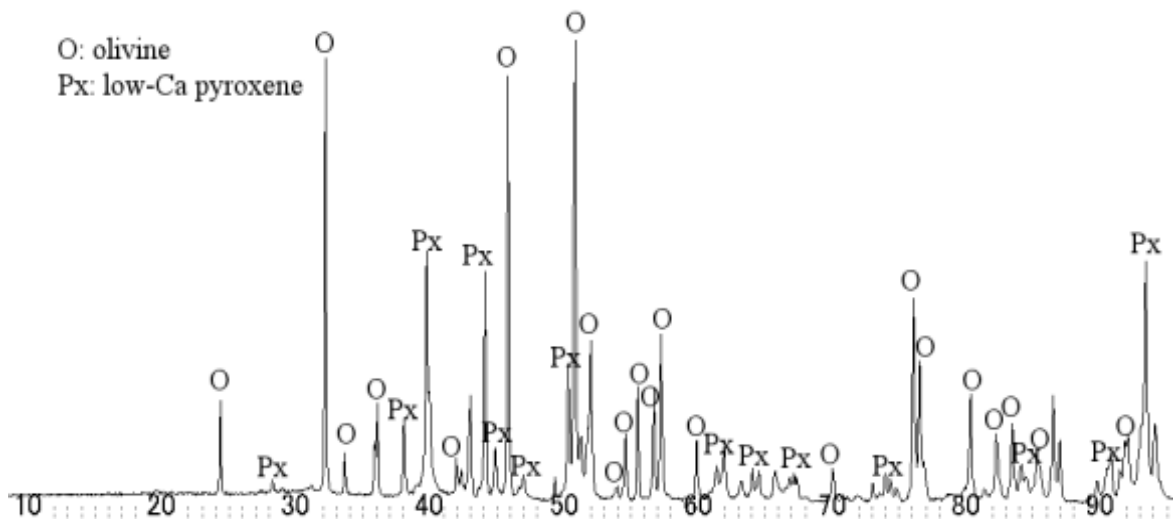
2AC23



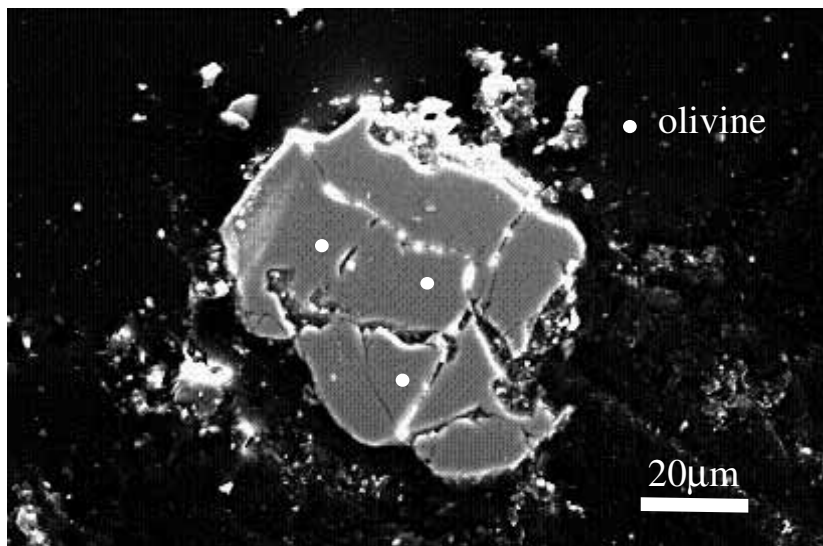
wt %	tr	kam
Ni		
Fe		
Mn		
Co		
Cr		
S		
P		
<hr/>		
Total		



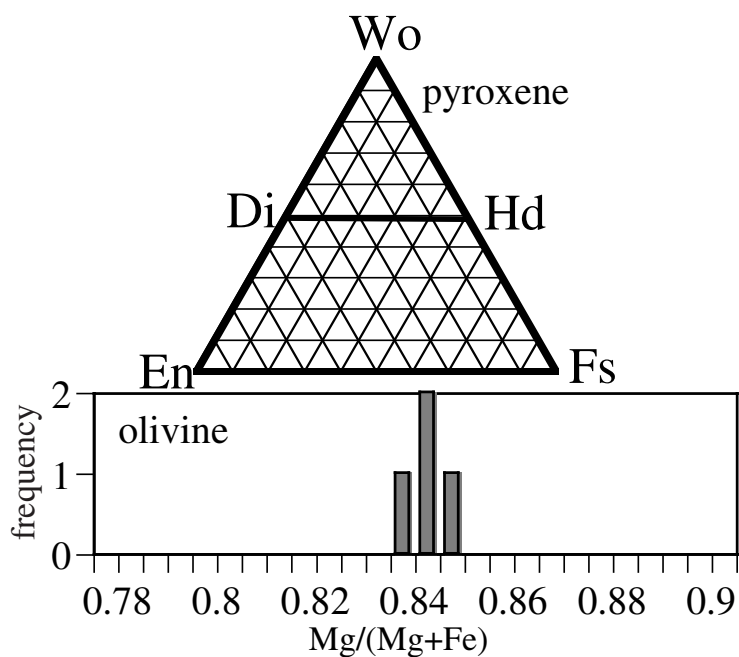
wt%	ol	low-Ca px	high-Ca px
SiO ₂	41.3		
TiO ₂	0.0		
Al ₂ O ₃	0.0		
FeO	14.2		
MnO	0.6		
MgO	44.4		
CaO	0.1		
Na ₂ O	0.0		
K ₂ O	0.0		
Cr ₂ O ₃	0.0		
NiO	0.0		
P ₂ O ₅	0.0		
SO ₃	0.0		
<hr/>			
total	100.6		



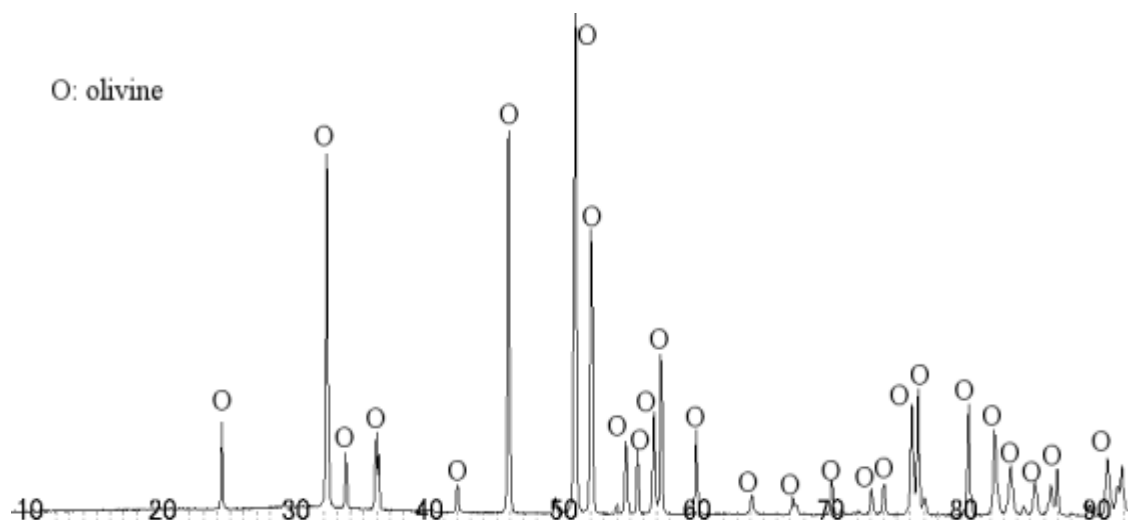
2AC24



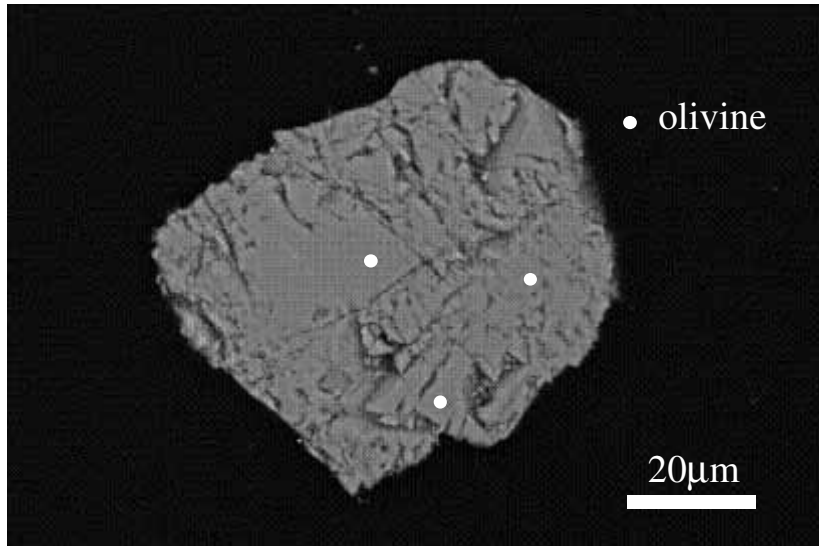
wt %	tr	kam
Ni		
Fe		
Mn		
Co		
Cr		
S		
P		
Total		



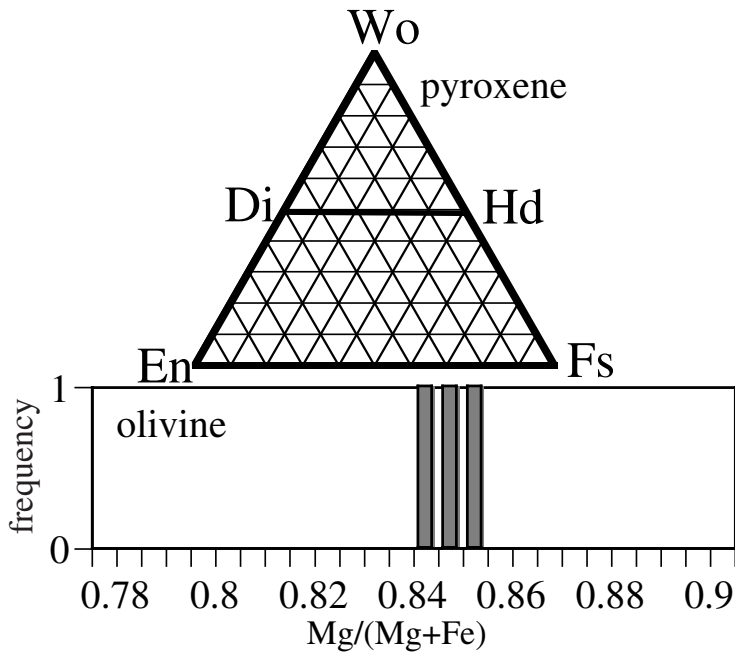
wt%	ol	low-Ca px	high-Ca px
SiO ₂	39.7		
TiO ₂	0.0		
Al ₂ O ₃	0.0		
FeO	14.9		
MnO	0.5		
MgO	45.2		
CaO	0.0		
Na ₂ O	0.0		
K ₂ O	0.0		
Cr ₂ O ₃	0.0		
NiO	0.0		
P ₂ O ₅	0.0		
SO ₃	0.0		
total	100.4		



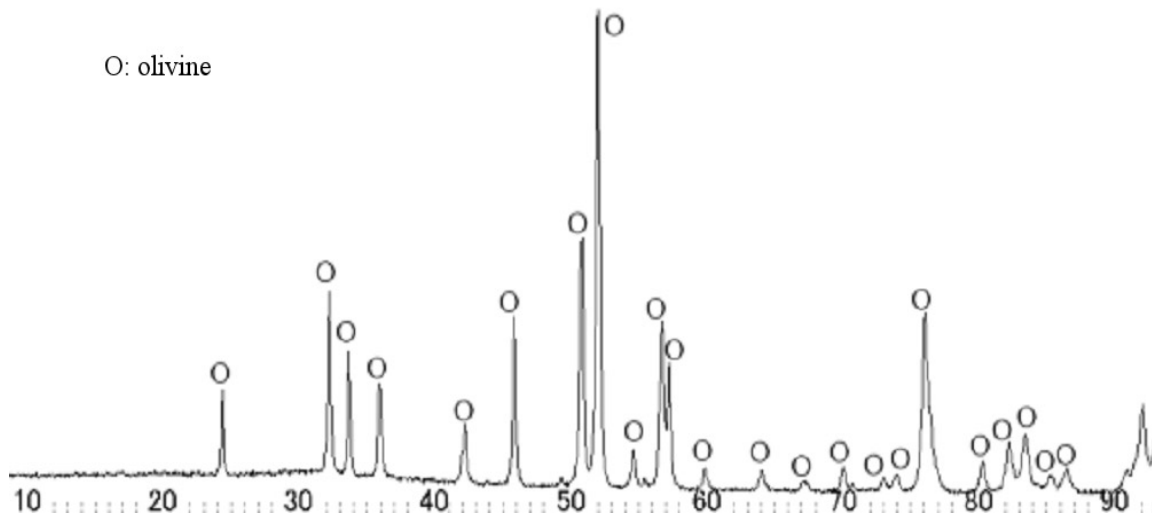
2AC25



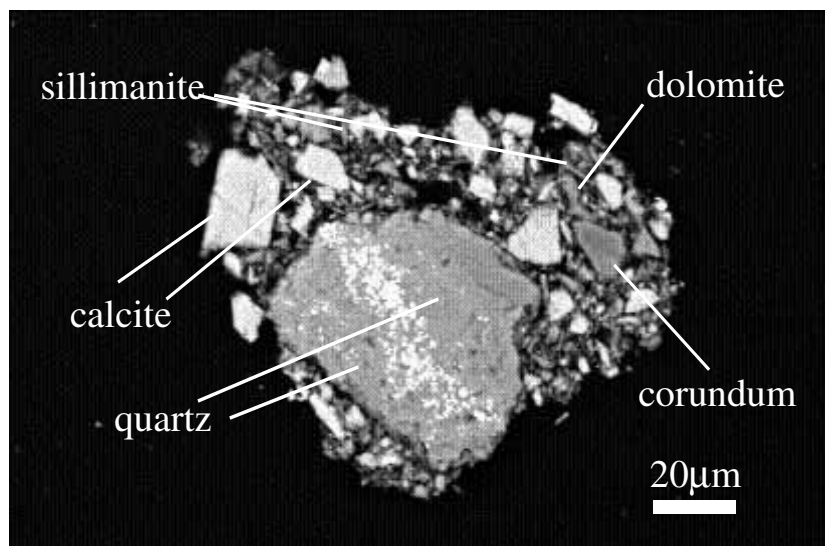
wt %	tr	kam
Ni		
Fe		
Mn		
Co		
Cr		
S		
P		
<hr/>		
Total		



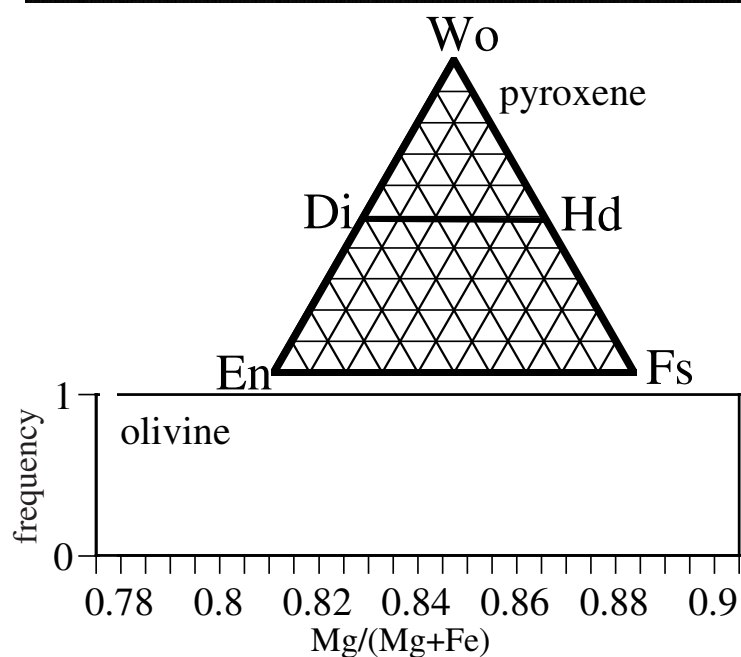
wt%	ol	low-Ca px	high-Ca px
SiO ₂	39.5		
TiO ₂	0.0		
Al ₂ O ₃	0.0		
FeO	14.7		
MnO	0.4		
MgO	44.9		
CaO	0.1		
Na ₂ O	0.0		
K ₂ O	0.0		
Cr ₂ O ₃	0.0		
NiO	0.0		
P ₂ O ₅	0.1		
SO ₃	0.0		
<hr/>			
total	99.7		



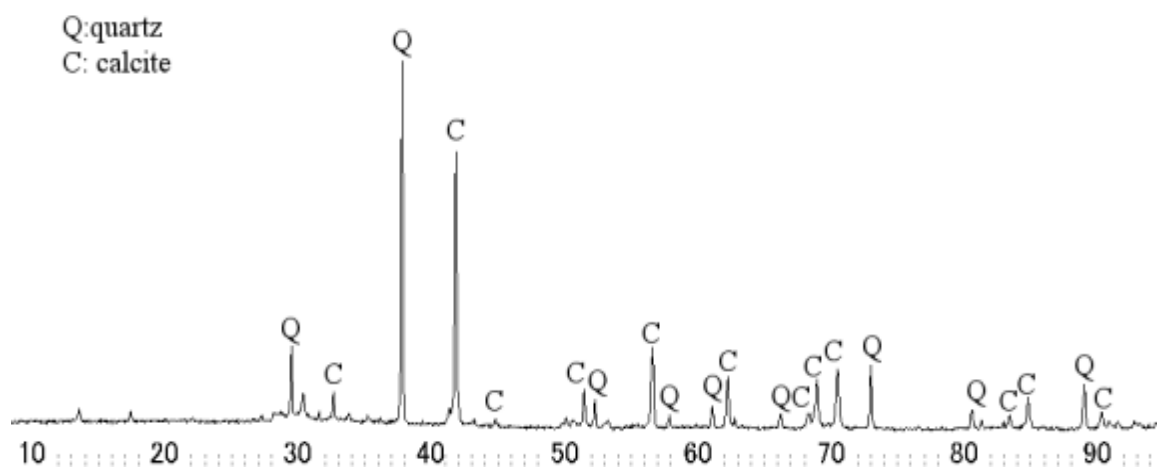
2AC26



wt %	tr	kam
Ni		
Fe		
Mn		
Co		
Cr		
S		
P		
<hr/>		
Total		

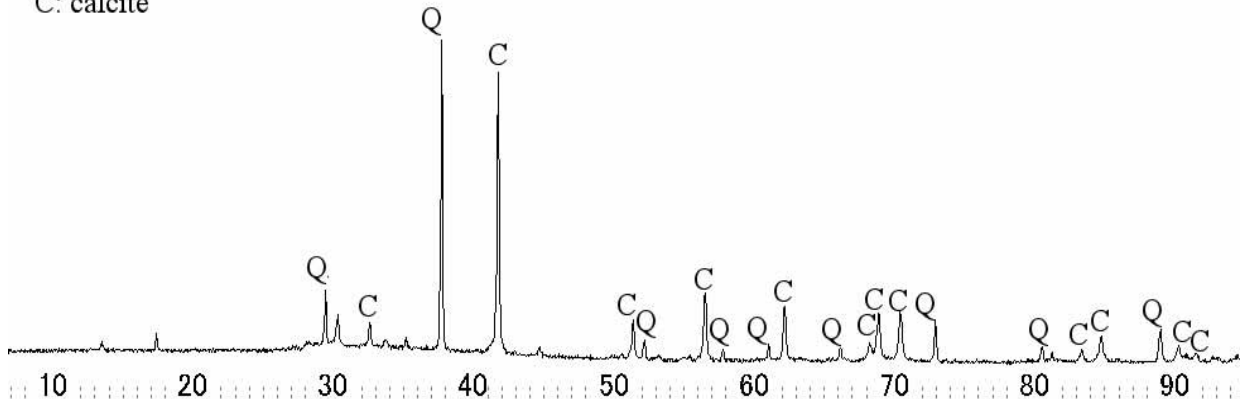


wt%	ol	low-Ca px	high-Ca px
SiO ₂			
TiO ₂			
Al ₂ O ₃			
FeO			
MnO			
MgO			
CaO			
Na ₂ O			
K ₂ O			
Cr ₂ O ₃			
NiO			
P ₂ O ₅			
SO ₃			
<hr/>			
total			



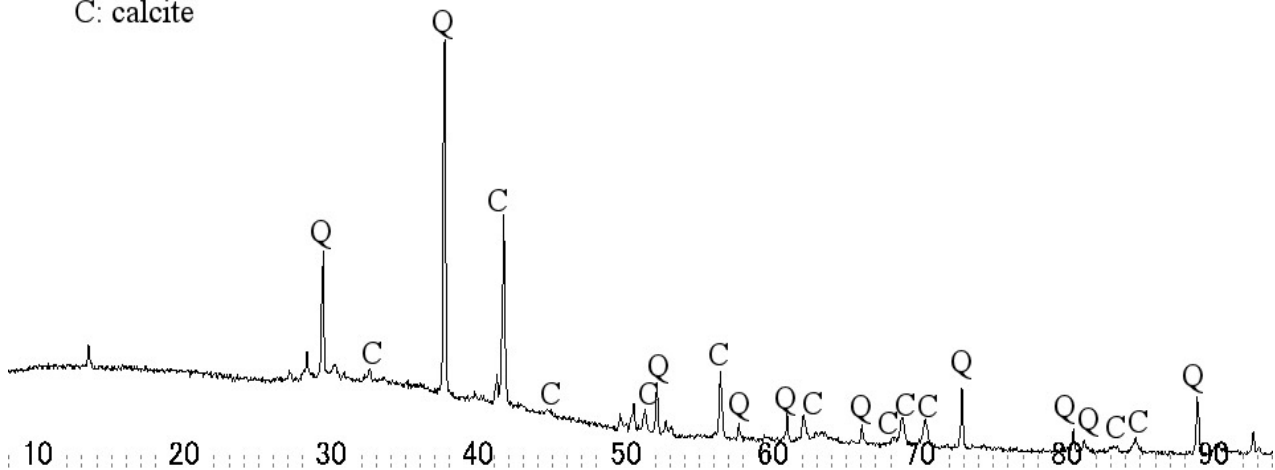
2AC27

Q: quartz
C: calcite



2AC28

Q: quartz
C: calcite



2AF1

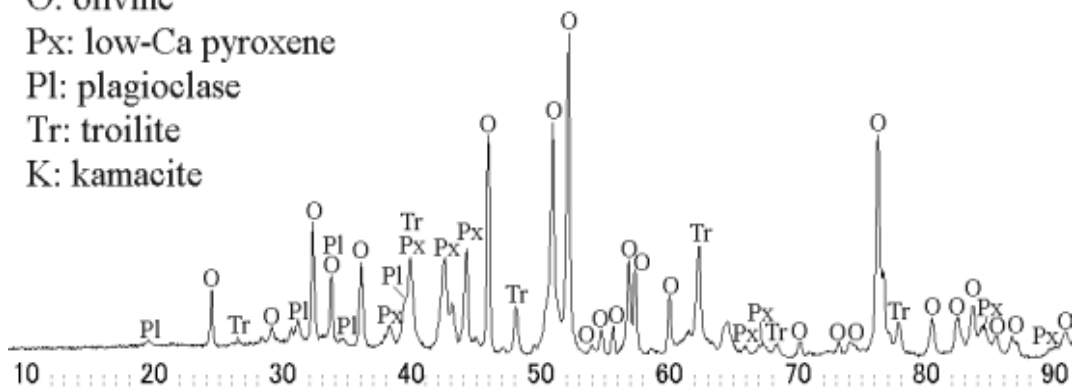
O: olivine

Px: low-Ca pyroxene

Pl: plagioclase

Tr: troilite

K: kamacite



2AF2

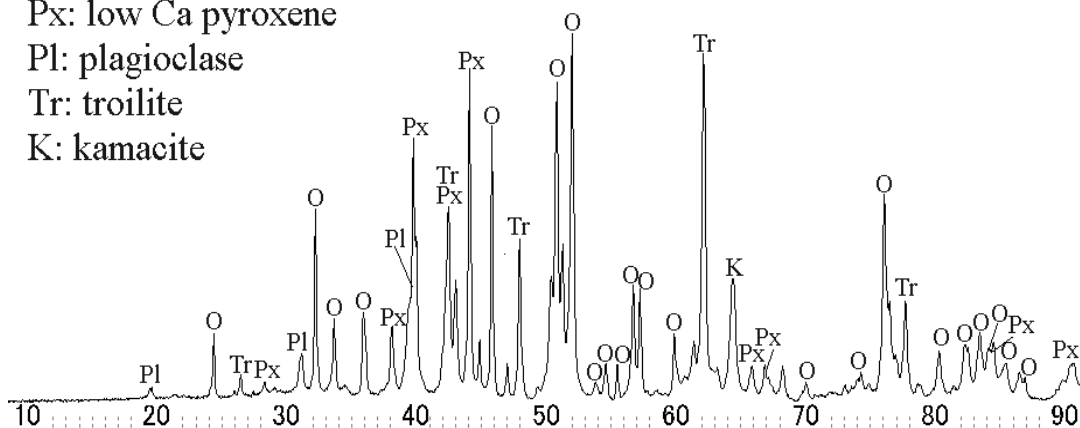
O: olivine

Px: low Ca pyroxene

Pl: plagioclase

Tr: troilite

K: kamacite



2AF3

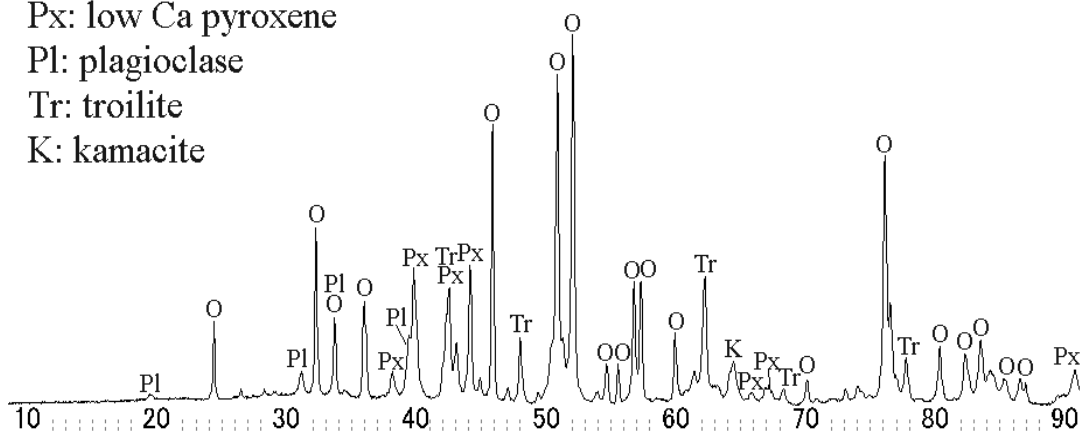
O: olivine

Px: low Ca pyroxene

Pl: plagioclase

Tr: troilite

K: kamacite



SEM and EPMA analyses did not performed on these samples.

2AF4

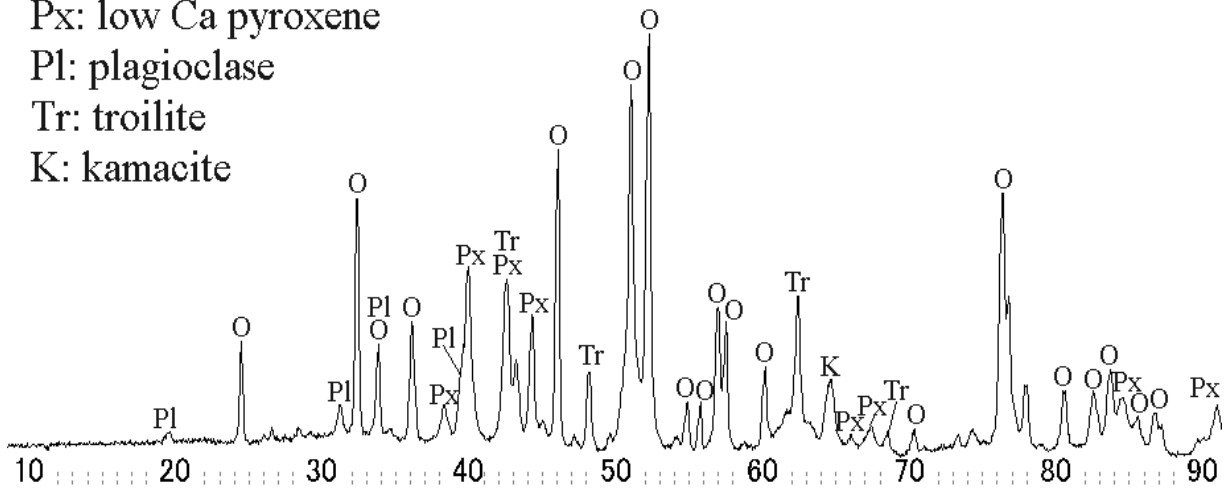
O: olivine

Px: low Ca pyroxene

Pl: plagioclase

Tr: troilite

K: kamacite



2AF5

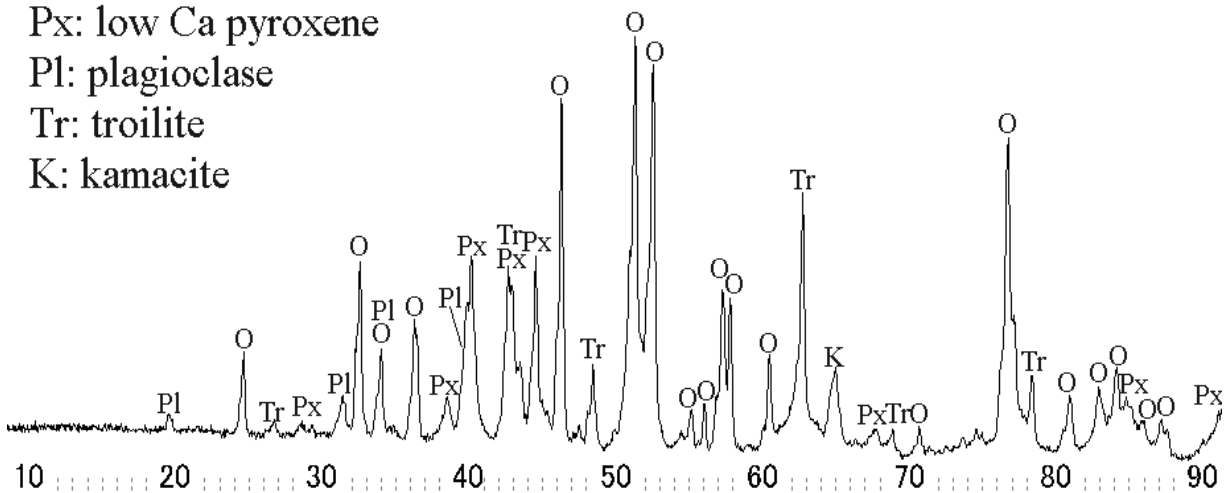
O: olivine

Px: low Ca pyroxene

Pl: plagioclase

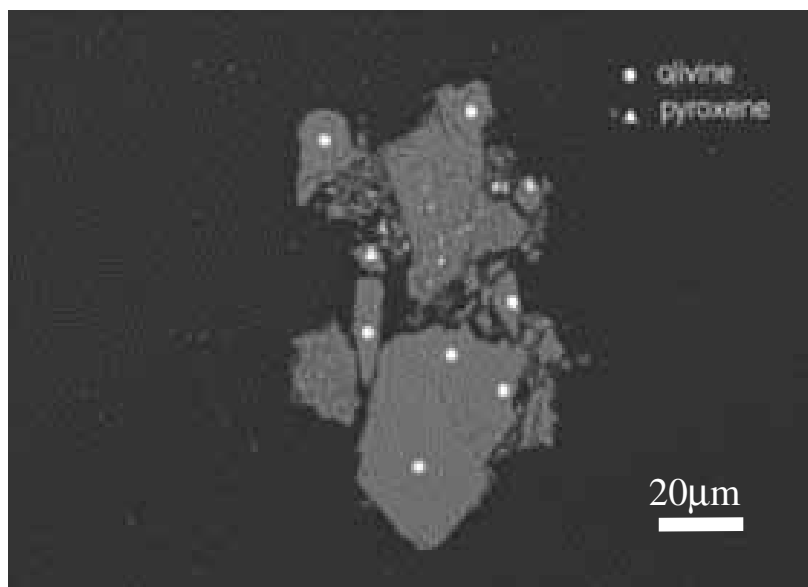
Tr: troilite

K: kamacite

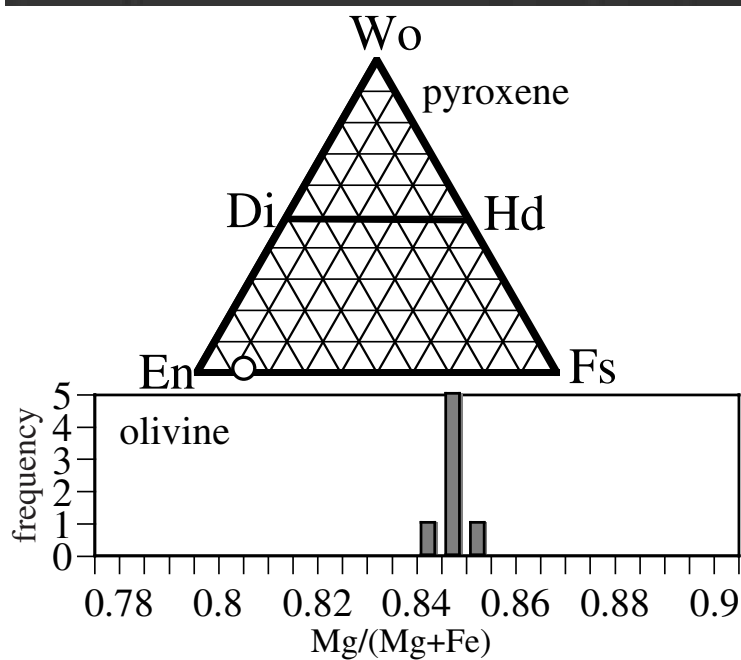


SEM and EPMA analyses did not performed on these samples.

2AF6

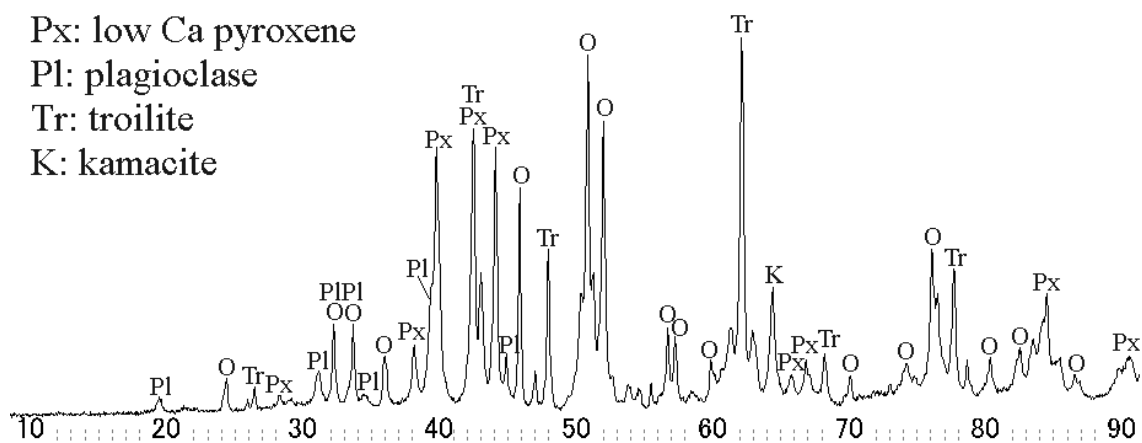


wt %	tr	kam
Ni		
Fe		
Mn		
Co		
Cr		
S		
P		
Total		

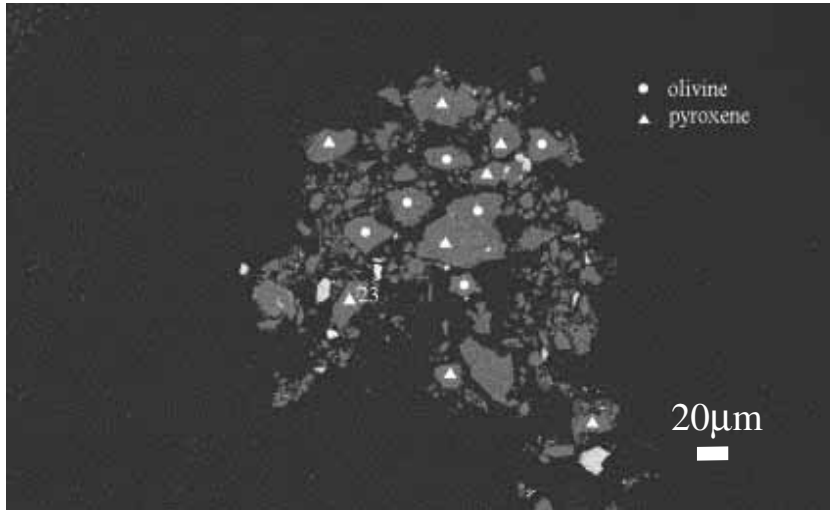


wt%	ol	low-Ca px	high-Ca px
SiO ₂	39.4	56.2	
TiO ₂	0.0	0.1	
Al ₂ O ₃	0.0	0.2	
FeO	15.1	8.7	
MnO	0.4	0.6	
MgO	45.3	32.2	
CaO	0.1	0.5	
Na ₂ O	0.0	0.2	
K ₂ O	0.0	0.0	
Cr ₂ O ₃	0.1	0.2	
NiO	0.1	0.0	
P ₂ O ₅	0.1	0.0	
SO ₃	0.0	0.1	
total	100.5	99.0	

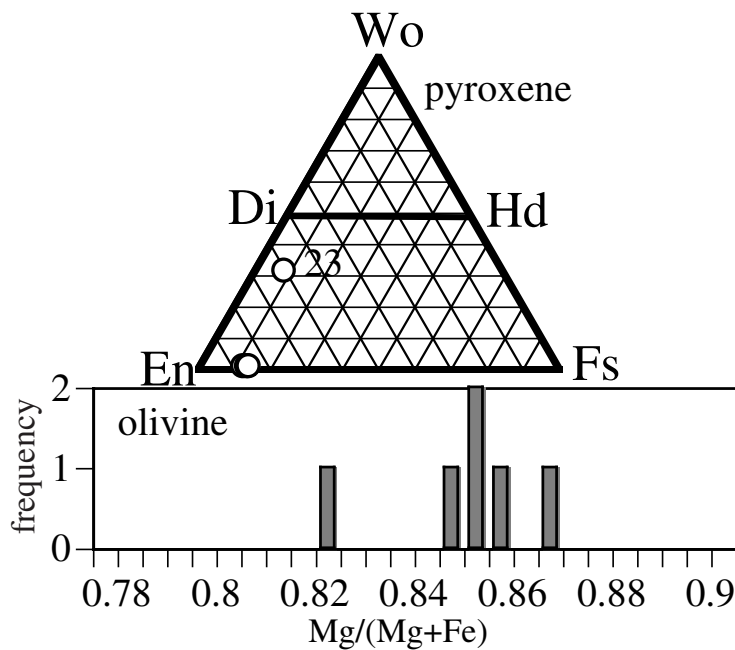
O: olivine
 Px: low Ca pyroxene
 Pl: plagioclase
 Tr: troilite
 K: kamacite



2AF7

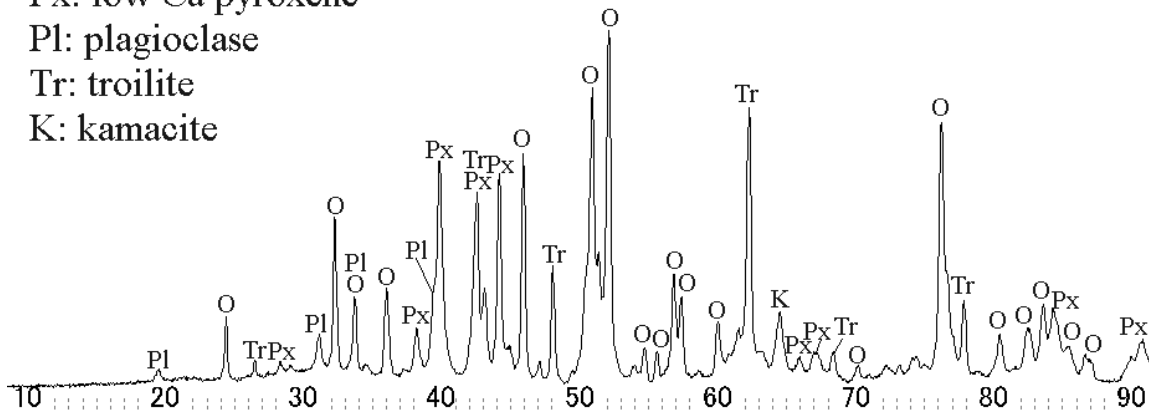


	wt %	tr	kam
Ni			
Fe			
Mn			
Co			
Cr			
S			
P			
Total			

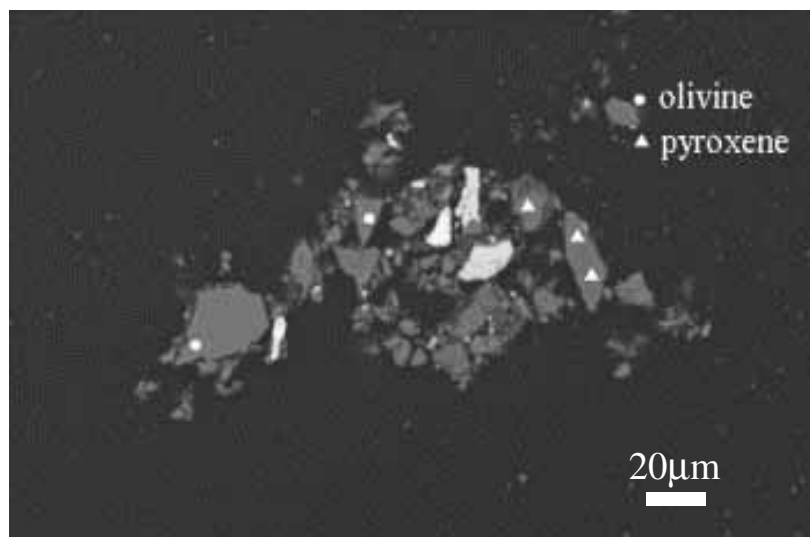


wt%	ol	low-Ca px	high-Ca px
SiO ₂	39.6	56.3	53.6
TiO ₂	0.0	0.1	0.2
Al ₂ O ₃	0.0	0.3	1.2
FeO	14.1	9.7	5.3
MnO	0.4	0.5	0.3
MgO	45.7	32.5	20.9
CaO	0.1	0.7	15.2
Na ₂ O	0.1	0.0	0.6
K ₂ O	0.0	0.0	0.0
Cr ₂ O ₃	0.0	0.1	0.6
NiO	0.0	0.0	0.0
P ₂ O ₅	0.1	0.0	0.0
SO ₃	0.0	0.0	1.3
total	100.0	100.3	99.2

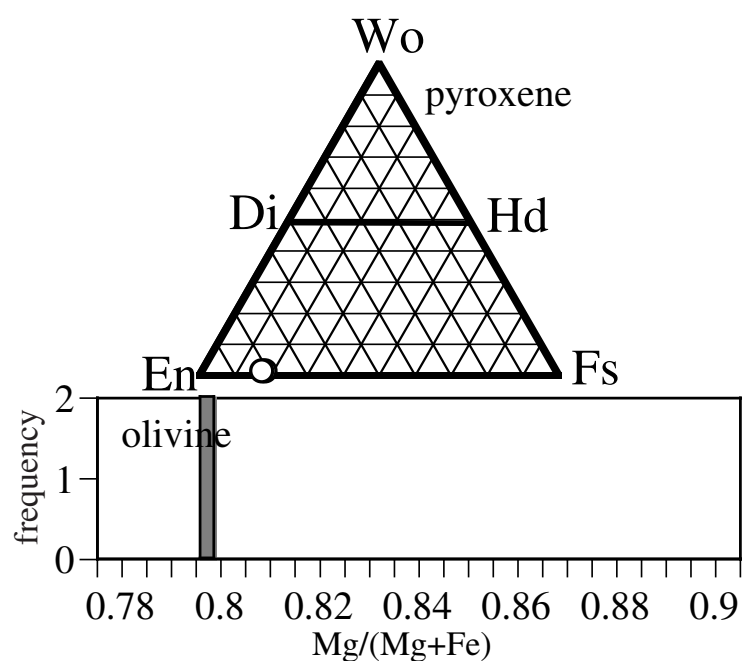
O: olivine
 Px: low Ca pyroxene
 Pl: plagioclase
 Tr: troilite
 K: kamacite



2AF8

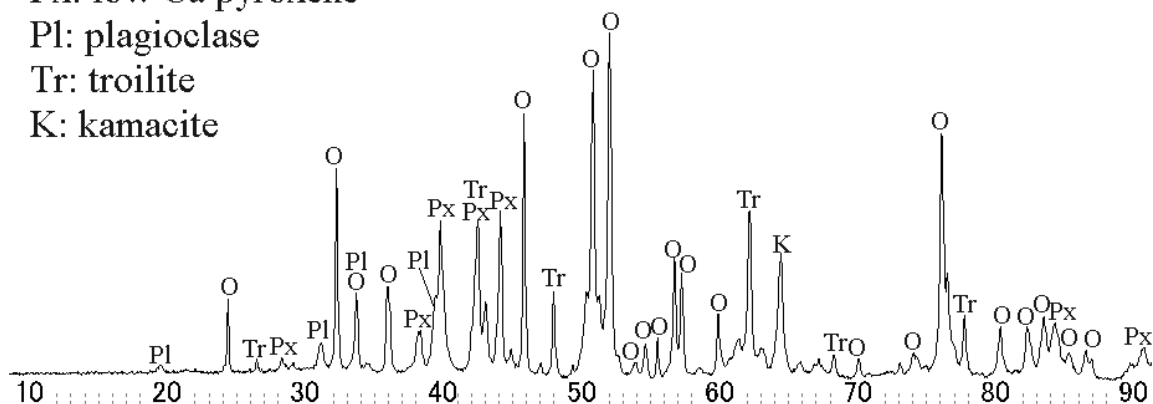


wt %	tr	kam
Ni		
Fe		
Mn		
Co		
Cr		
S		
P		
Total		

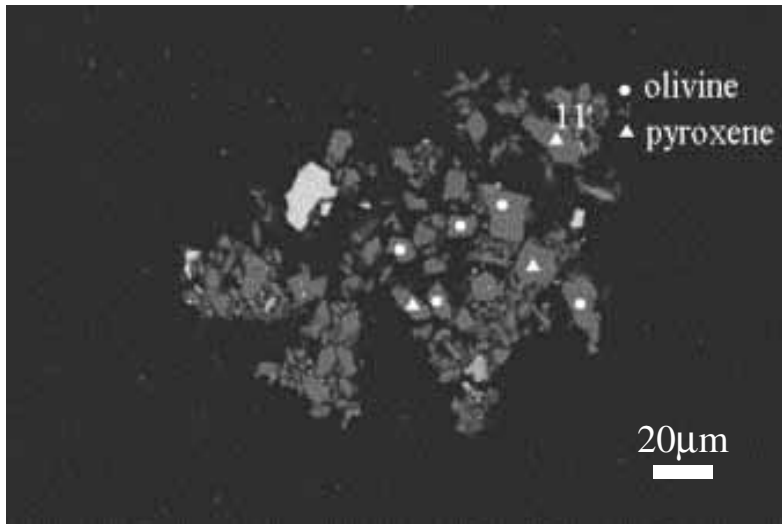


wt%	ol	low-Ca px	high-Ca px
SiO ₂	40.7	57.2	
TiO ₂	0.0	0.2	
Al ₂ O ₃	0.0	0.3	
FeO	18.0	11.5	
MnO	0.6	0.8	
MgO	40.2	28.4	
CaO	0.0	0.5	
Na ₂ O	0.1	0.0	
K ₂ O	0.0	0.0	
Cr ₂ O ₃	0.1	0.2	
NiO	0.0	0.0	
P ₂ O ₅	0.0	0.0	
SO ₃	0.0	0.0	
total	99.7	99.0	

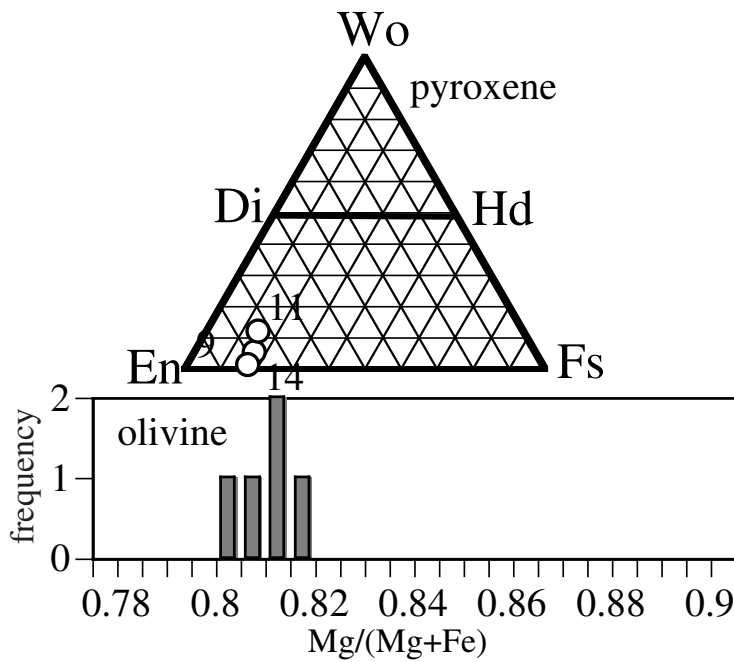
O: olivine
 Px: low Ca pyroxene
 Pl: plagioclase
 Tr: troilite
 K: kamacite



2AF9

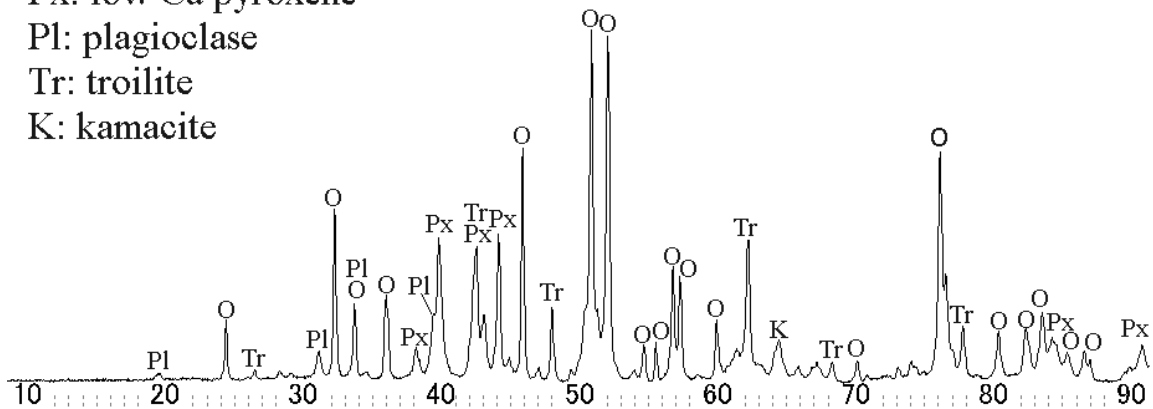


wt %	tr	kam
Ni		
Fe		
Mn		
Co		
Cr		
S		
P		
Total		

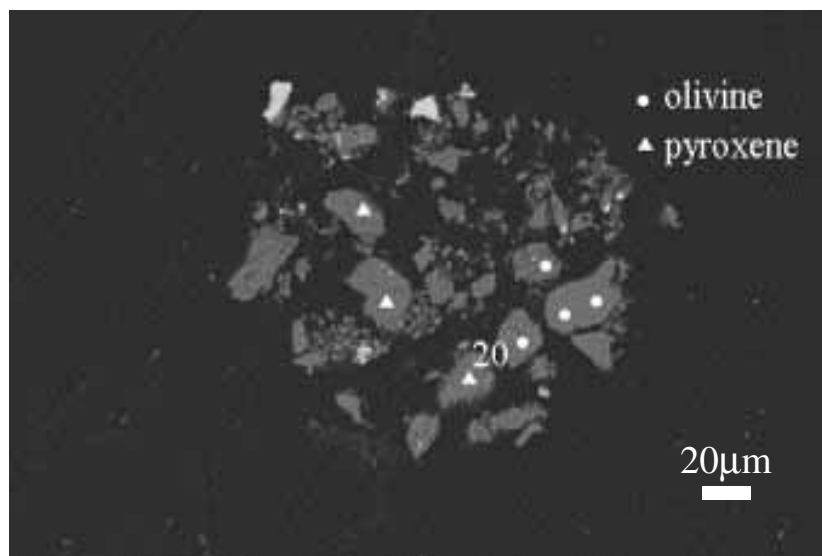


wt%	ol	low-Ca px	high-Ca px
SiO ₂	41.5	57.0	59.3
TiO ₂	0.0	0.1	0.1
Al ₂ O ₃	0.0	0.5	1.1
FeO	16.7	10.8	9.1
MnO	0.6	0.5	0.5
MgO	41.4	27.4	24.5
CaO	0.1	2.4	5.5
Na ₂ O	0.2	0.1	0.5
K ₂ O	0.0	0.0	0.0
Cr ₂ O ₃	0.0	0.2	0.3
NiO	0.0	0.0	0.0
P ₂ O ₅	0.0	0.1	0.1
SO ₃	0.0	0.0	0.1
total	100.6	99.1	101.1

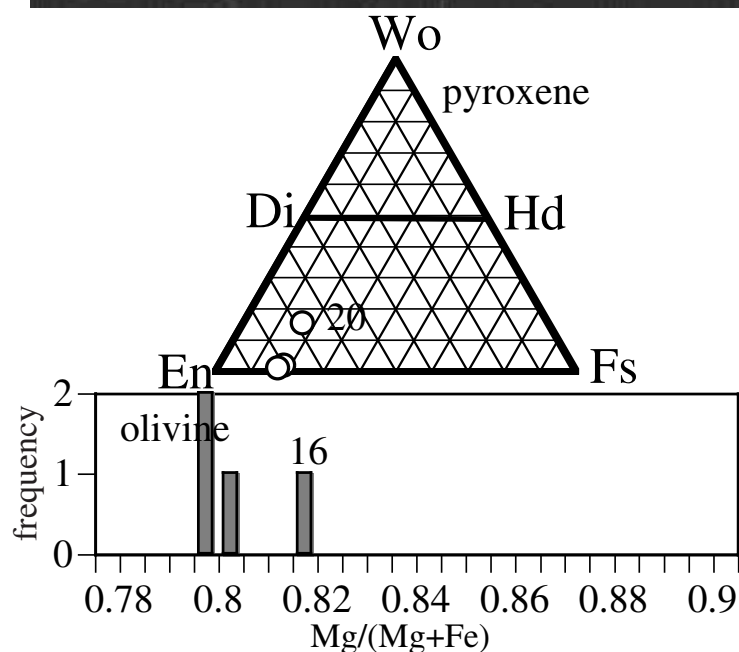
O: olivine
 Px: low Ca pyroxene
 Pl: plagioclase
 Tr: troilite
 K: kamacite



2AF10



wt %	tr	kam
Ni		
Fe		
Mn		
Co		
Cr		
S		
P		
Total		



wt%	ol	low-Ca px	high-Ca px
SiO ₂	41.6	56.9	56.4
TiO ₂	0.0	0.1	0.2
Al ₂ O ₃	0.0	0.2	0.9
FeO	16.5	11.5	10.6
MnO	0.5	0.6	0.6
MgO	41.0	28.7	23.7
CaO	0.0	0.8	7.3
Na ₂ O	0.0	0.2	0.3
K ₂ O	0.0	0.0	0.0
Cr ₂ O ₃	0.0	0.2	1.0
NiO	0.0	0.0	0.0
P ₂ O ₅	0.0	0.0	0.0
SO ₃	0.0	0.0	0.0
total	99.7	99.3	100.8

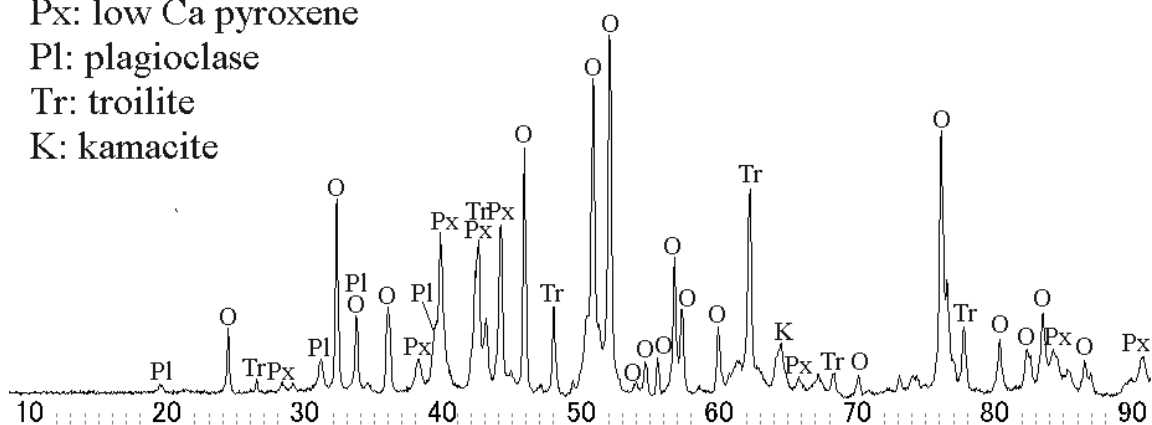
O: olivine

Px: low Ca pyroxene

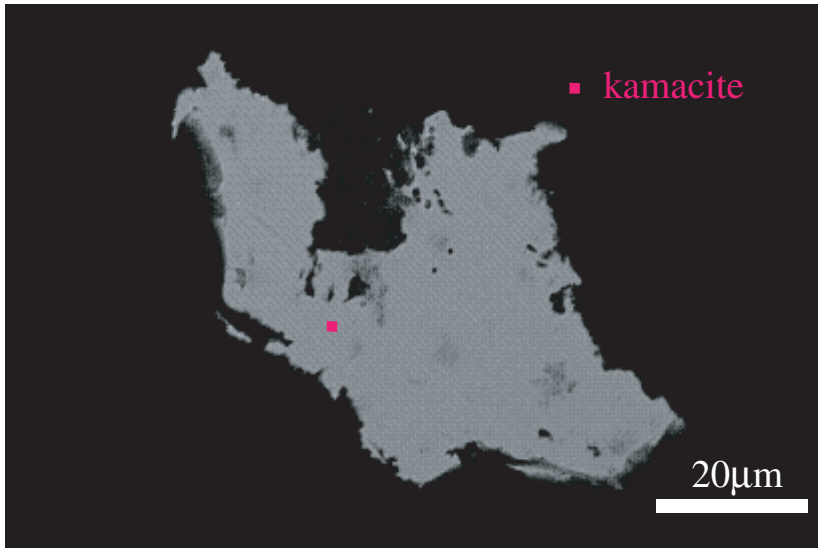
Pl: plagioclase

Tr: troilite

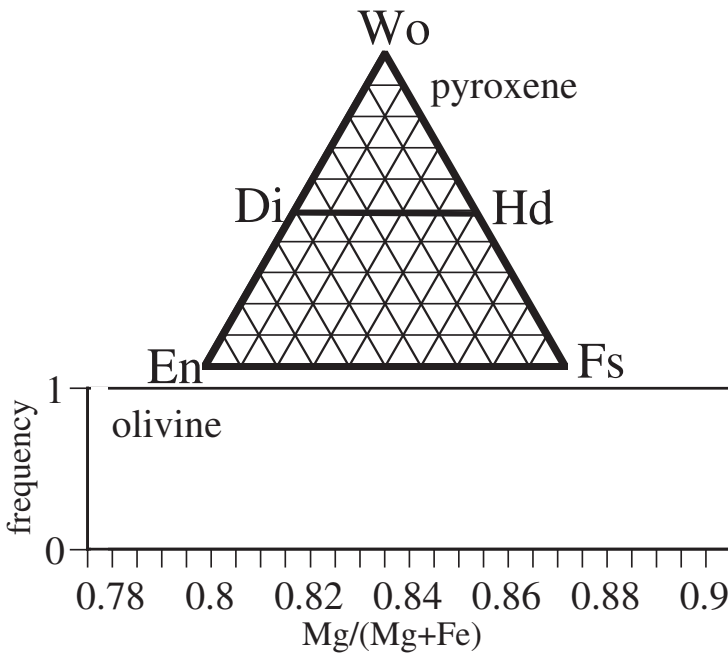
K: kamacite



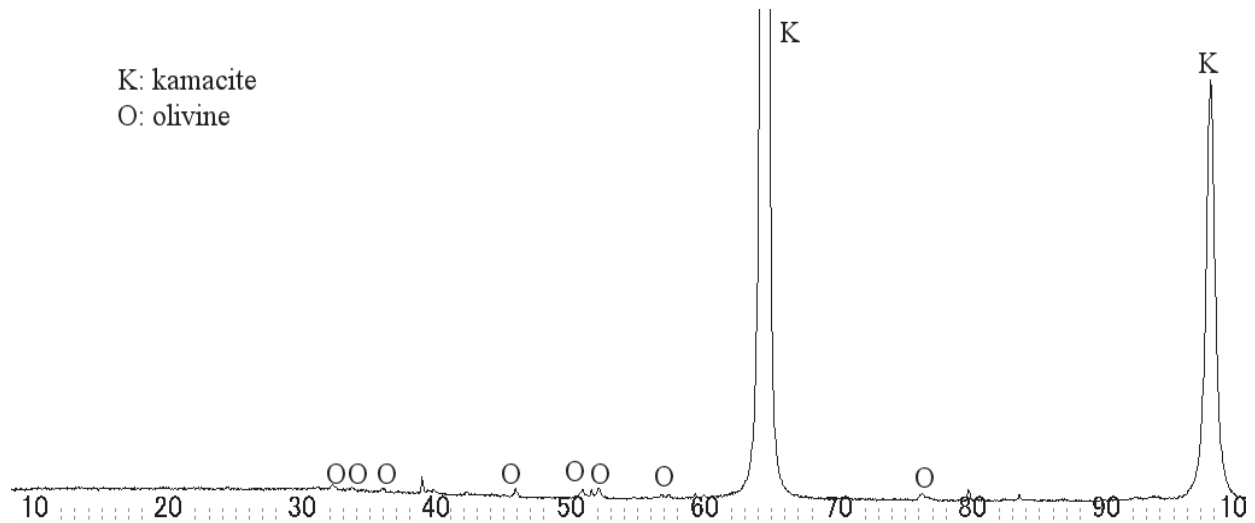
2BC1



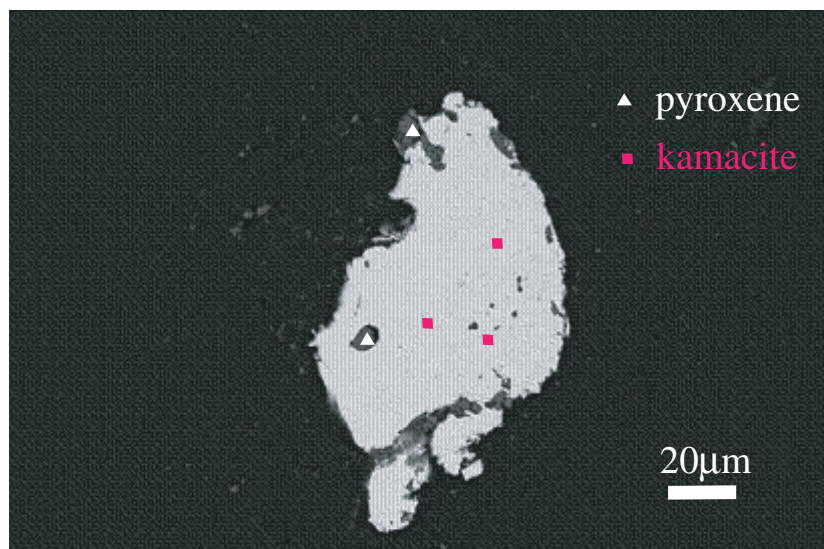
wt %	tr	kam
Ni		5.2
Fe		94.4
Mn		0.0
Co		0.4
Cr		0.0
S		0.0
P		0.0
Total		100.1



wt%	ol	low-Ca px	high-Ca px
SiO ₂			
TiO ₂			
Al ₂ O ₃			
FeO			
MnO			
MgO			
CaO			
Na ₂ O			
K ₂ O			
Cr ₂ O ₃			
NiO			
P ₂ O ₅			
SO ₃			
total			

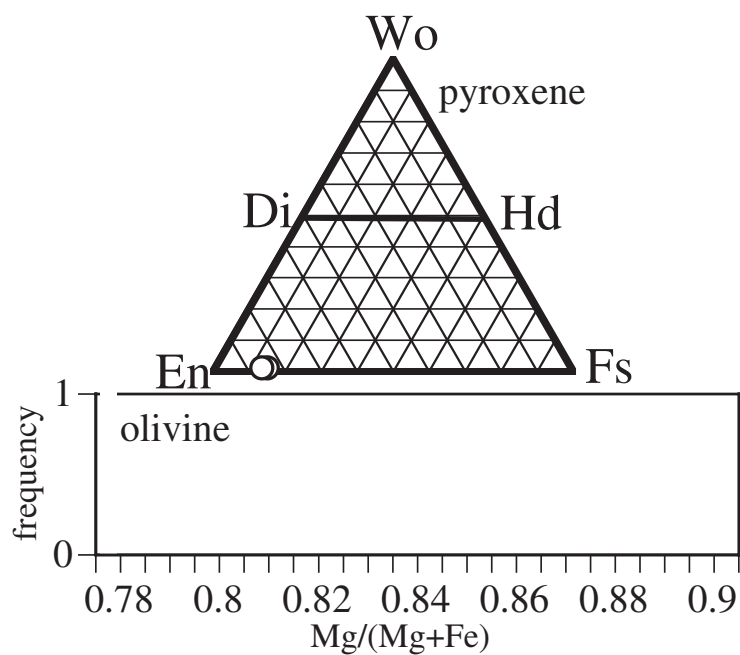


2BC2



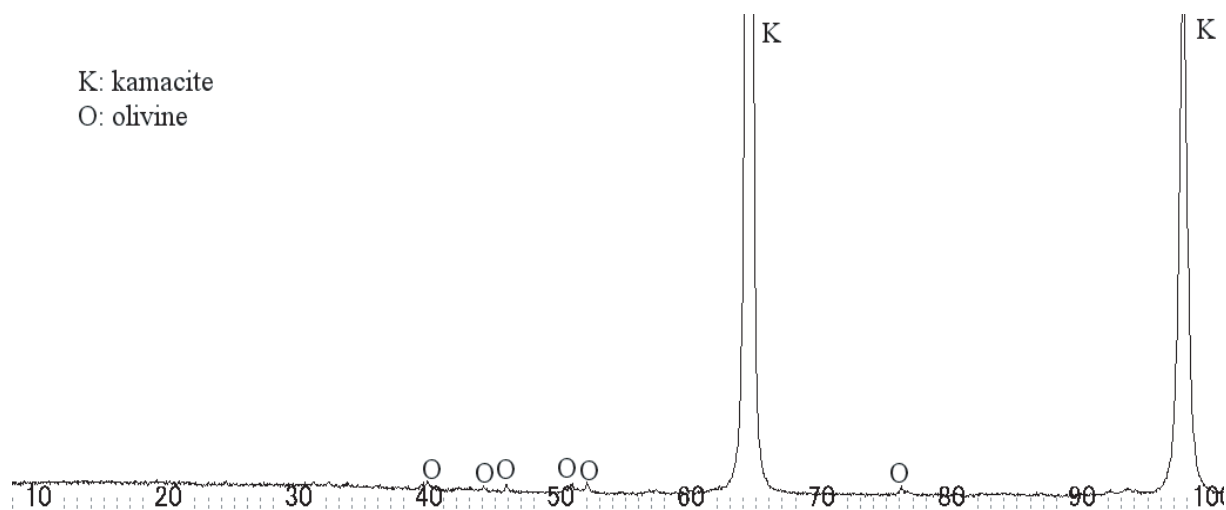
2BC2

wt %	tr	kam
Ni		5.2
Fe		94.2
Mn		0.0
Co		0.4
Cr		0.0
S		0.0
P		0.0
Total		100.0

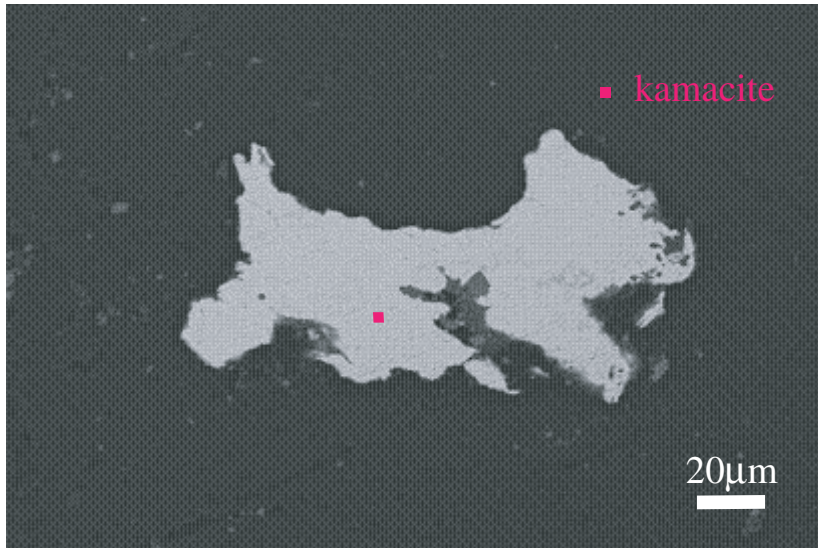


wt%	ol	low-Ca px	high-Ca px
SiO ₂		56.8	
TiO ₂		0.1	
Al ₂ O ₃		0.1	
FeO		9.5	
MnO		0.5	
MgO		33.3	
CaO		0.4	
Na ₂ O		0.0	
K ₂ O		0.0	
Cr ₂ O ₃		0.1	
NiO		0.0	
P ₂ O ₅		0.0	
SO ₃		0.0	
total		100.8	

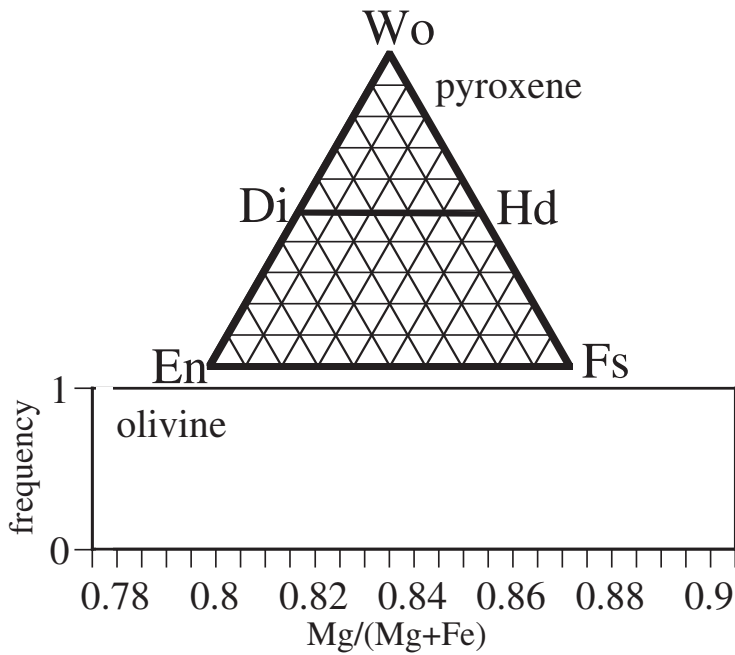
K: kamacite
O: olivine



2BC3

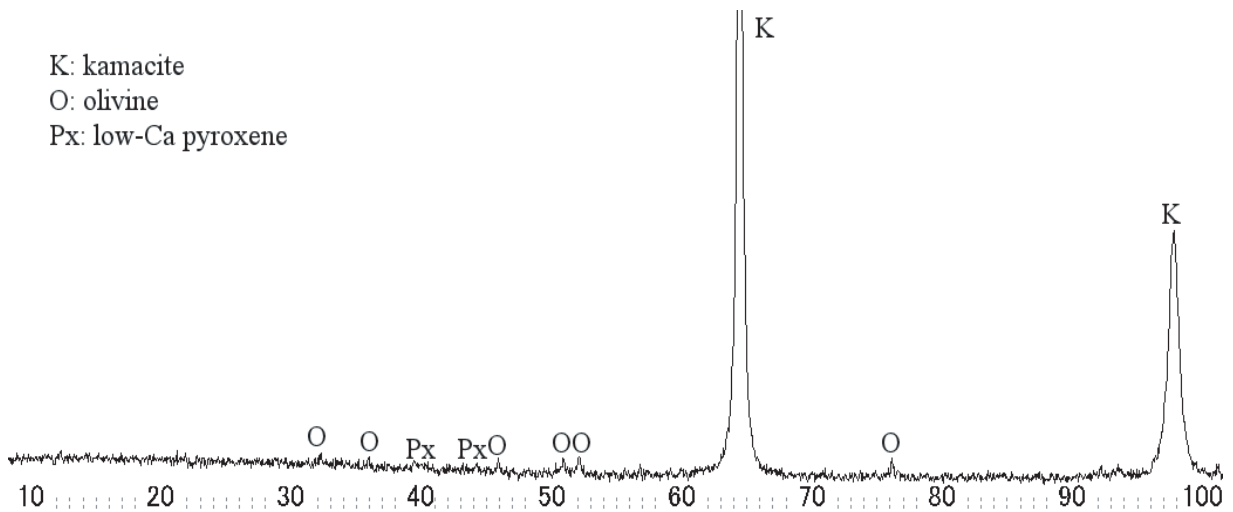


2BC3		
wt %	tr	kam
Ni		5.8
Fe		94.2
Mn		0.0
Co		0.4
Cr		0.0
S		0.0
P		0.0
Total		100.4

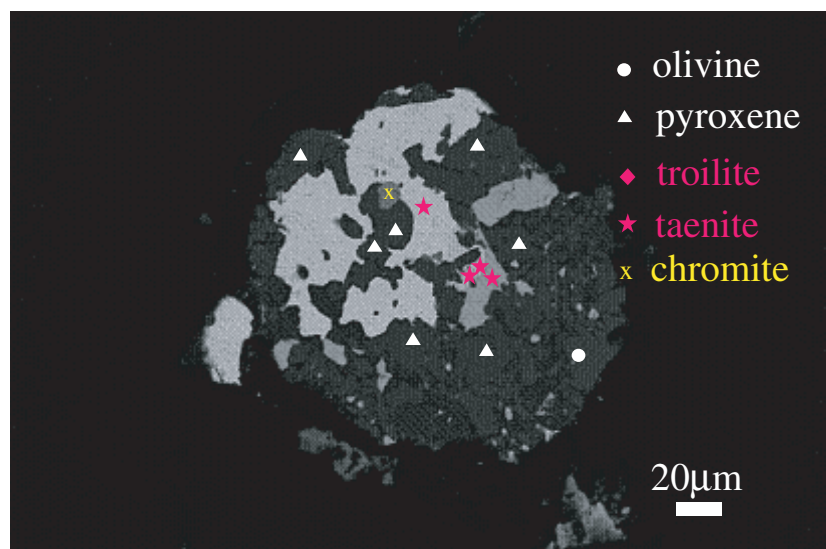


wt%	ol	low-Ca px	high-Ca px
SiO ₂			
TiO ₂			
Al ₂ O ₃			
FeO			
MnO			
MgO			
CaO			
Na ₂ O			
K ₂ O			
Cr ₂ O ₃			
NiO			
P ₂ O ₅			
SO ₃			
total			

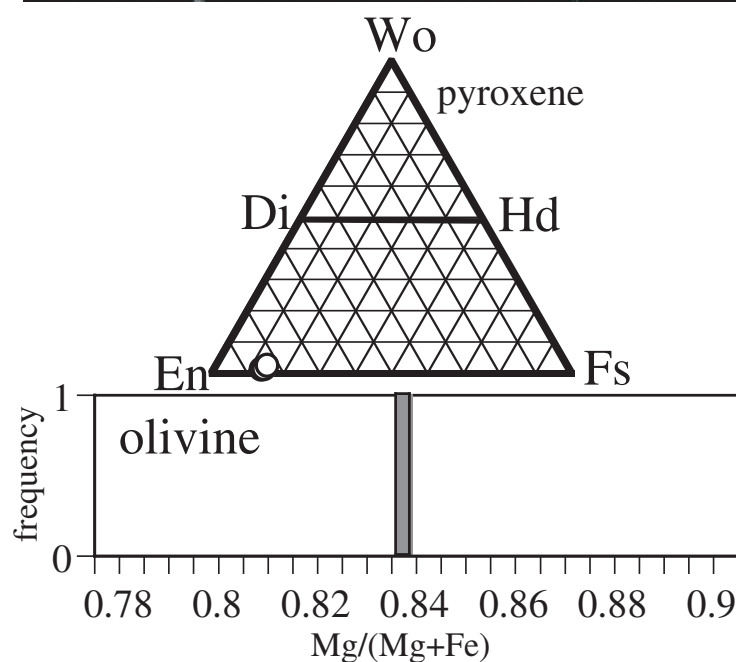
K: kamacite
 O: olivine
 Px: low-Ca pyroxene



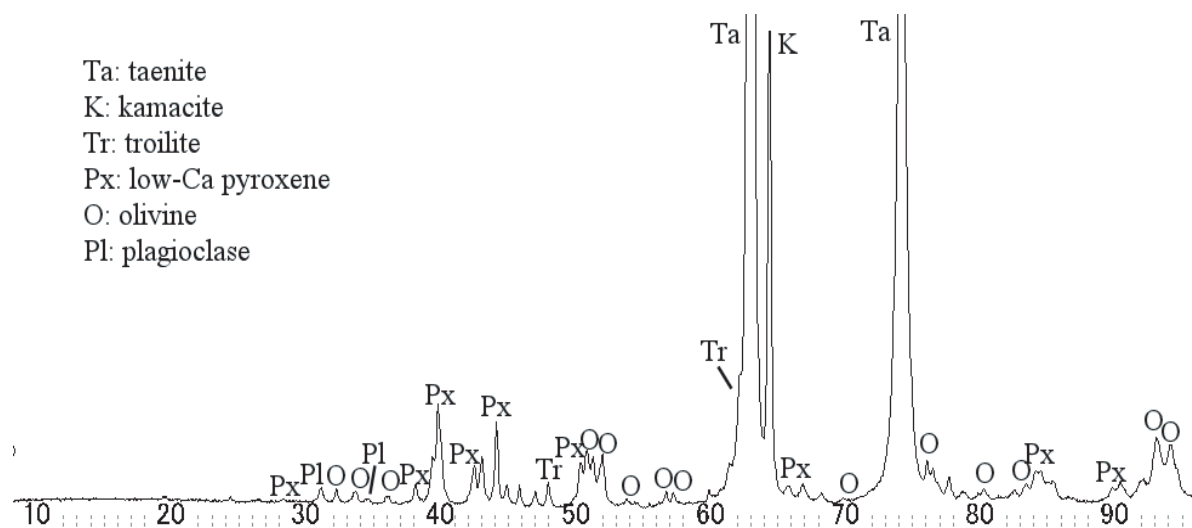
2BC4



wt %	tr	tae
Ni		49.9
Fe		50.1
Mn		0.0
Co		0.1
Cr		0.1
S		0.0
P		0.0
Total		100.2

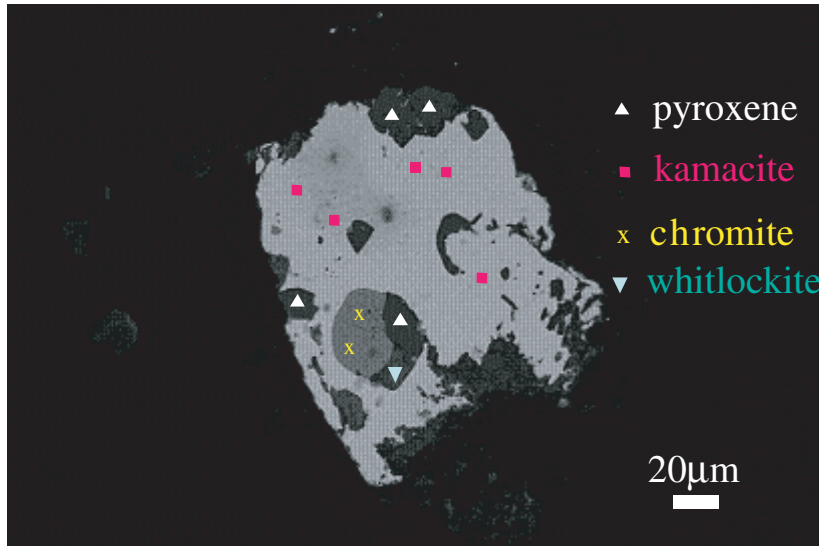


wt%	ol	low-Ca px	high-Ca px
SiO ₂	38.8	55.6	
TiO ₂	0.0	0.1	
Al ₂ O ₃	0.0	0.7	
FeO	15.2	9.9	
MnO	0.5	0.6	
MgO	44.3	31.1	
CaO	0.0	0.9	
Na ₂ O	0.0	0.4	
K ₂ O	0.0	0.0	
Cr ₂ O ₃	0.1	0.0	
NiO	0.1	0.4	
P ₂ O ₅	0.0	0.3	
SO ₃	0.0	0.0	
total	99.0	100.0	

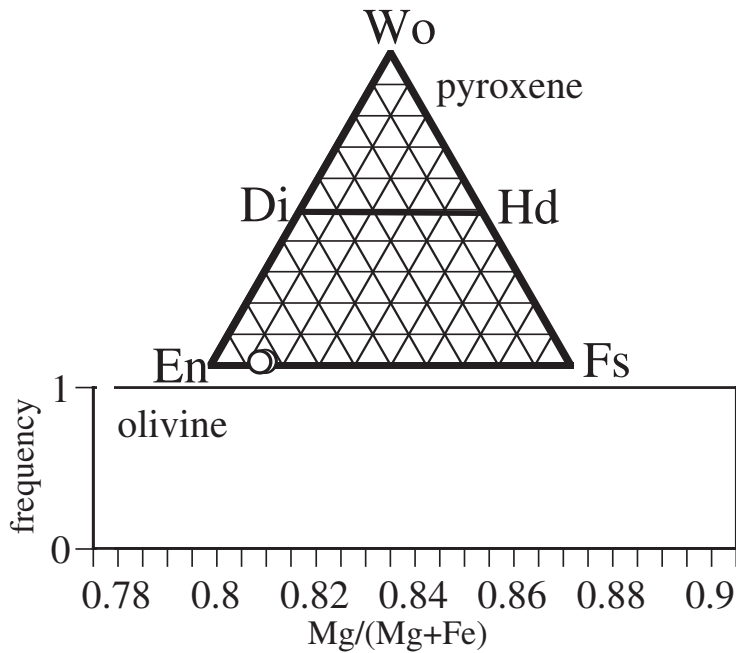


Ta: taenite
 K: kamacite
 Tr: troilite
 Px: low-Ca pyroxene
 O: olivine
 Pl: plagioclase

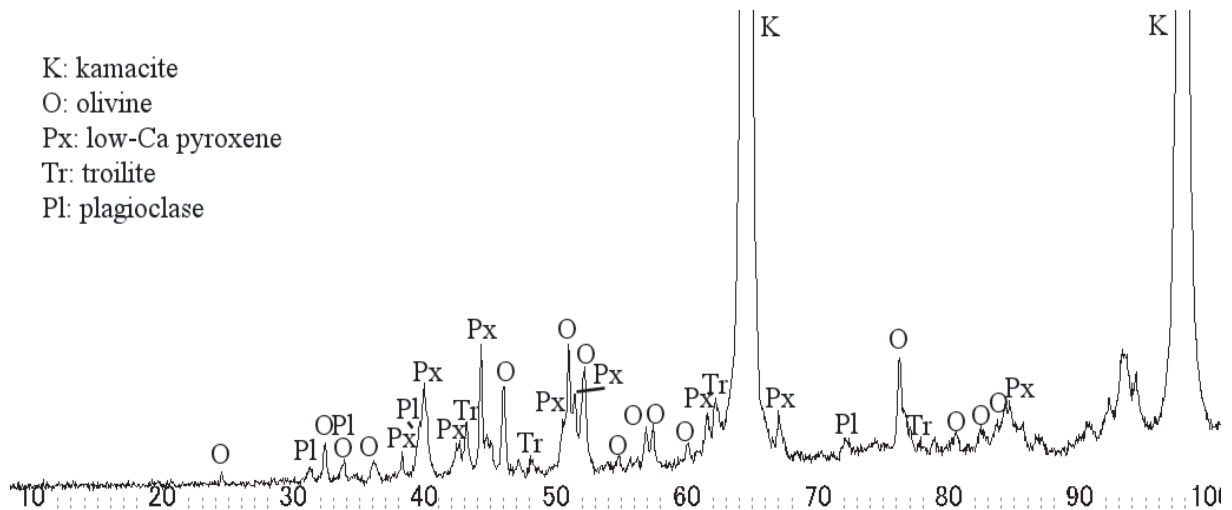
2BC5



wt %	tr	kam
Ni		4.8
Fe		94.0
Mn		0.0
Co		0.5
Cr		0.0
S		0.0
P		0.0
Total		99.4

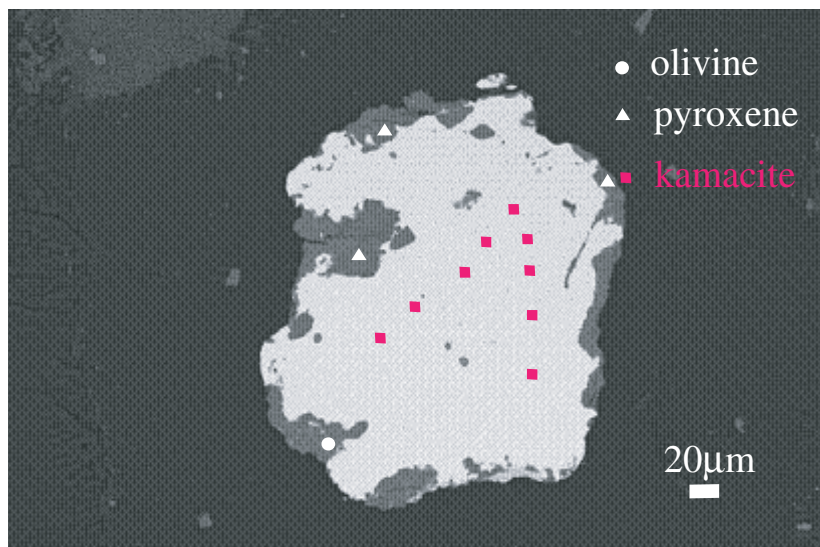


wt%	ol	low-Ca px	high-Ca px
SiO ₂		56.8	
TiO ₂		0.1	
Al ₂ O ₃		0.2	
FeO		10.1	
MnO		0.5	
MgO		32.3	
CaO		0.4	
Na ₂ O		0.1	
K ₂ O		0.0	
Cr ₂ O ₃		0.2	
NiO		0.0	
P ₂ O ₅		0.0	
SO ₃		0.1	
total		100.8	

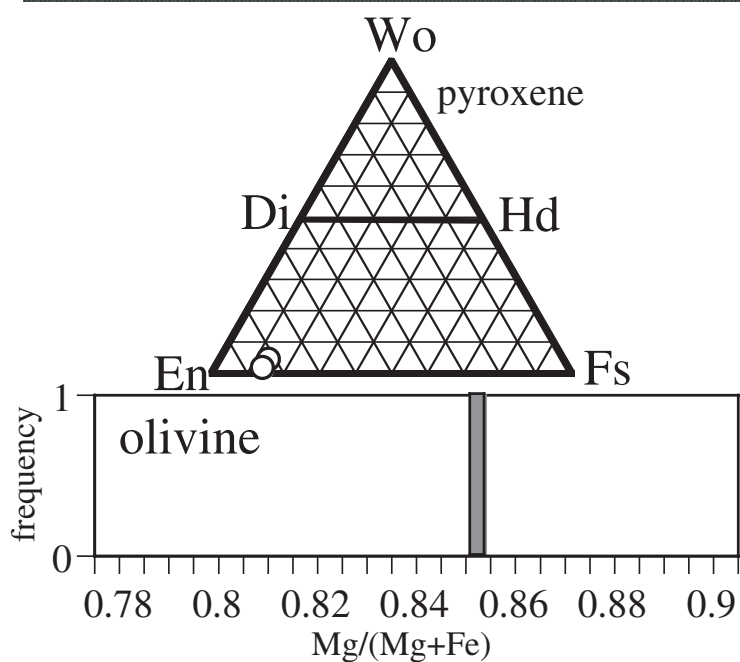


K: kamacite
 O: olivine
 Px: low-Ca pyroxene
 Tr: troilite
 Pl: plagioclase

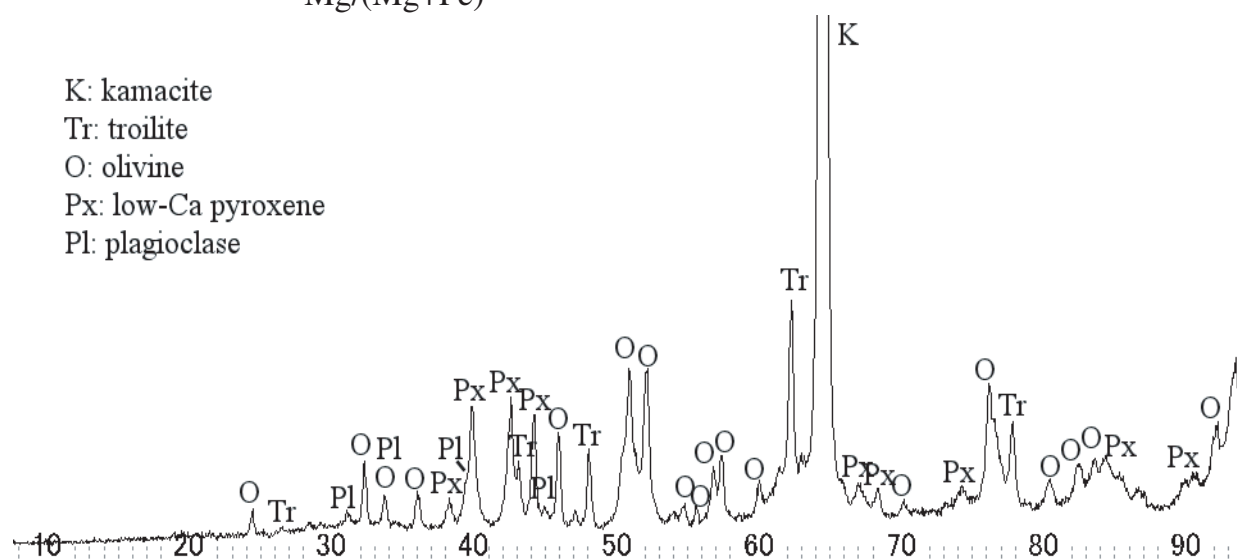
2BC6



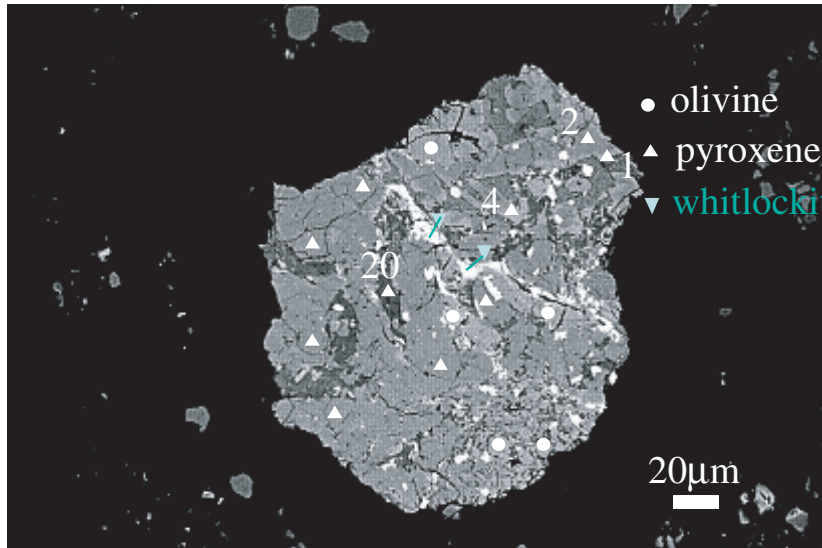
wt %	tr	kam
Ni		6.2
Fe		94.1
Mn		0.0
Co		0.3
Cr		0.0
S		0.0
P		0.0
Total		100.6



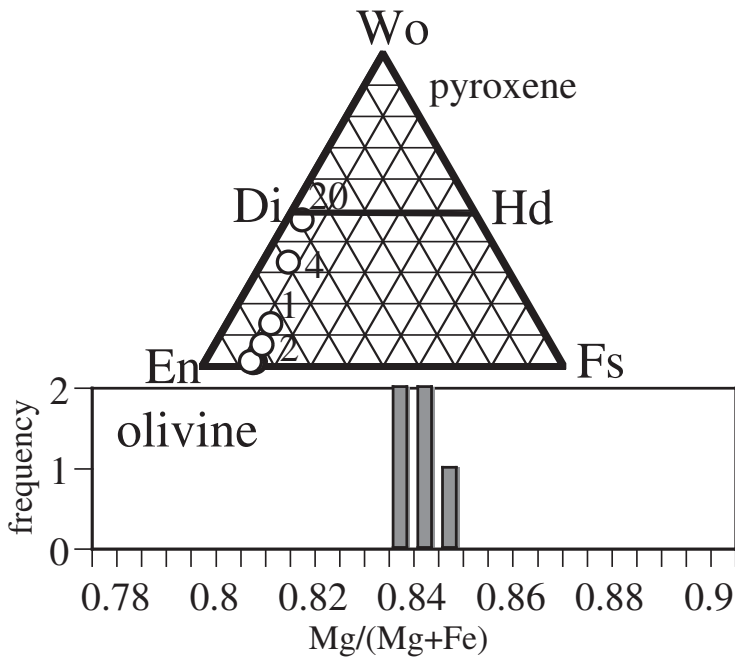
wt%	ol	low-Ca px	high-Ca px
SiO ₂	39.6	55.4	
TiO ₂	0.0	0.1	
Al ₂ O ₃	0.0	0.2	
FeO	13.8	9.8	
MnO	0.4	0.5	
MgO	45.4	31.2	
CaO	0.0	2.2	
Na ₂ O	0.0	0.0	
K ₂ O	0.0	0.0	
Cr ₂ O ₃	0.1	0.7	
NiO	0.0	0.0	
P ₂ O ₅	0.0	0.1	
SO ₃	0.0	0.0	
total	99.5	100.3	



2BC7

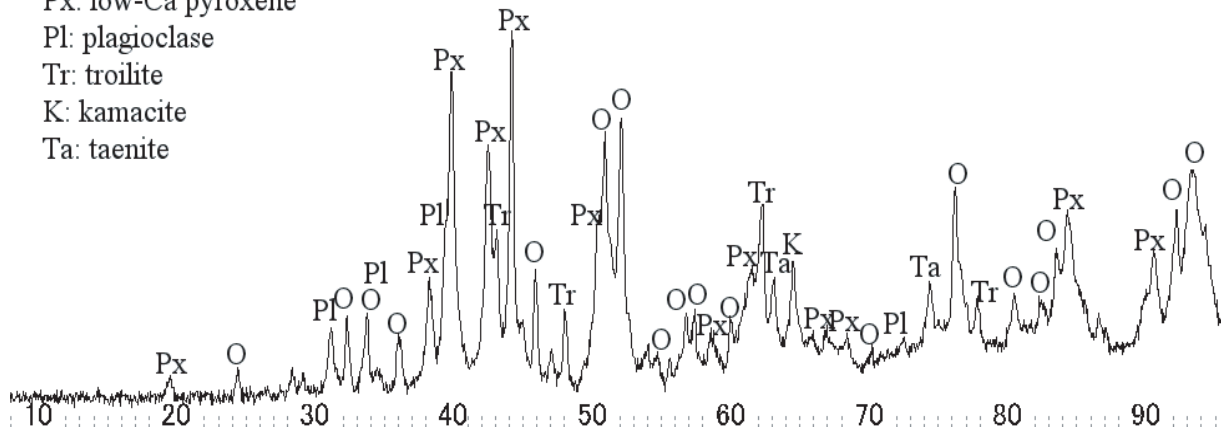


wt %	tr	kam
Ni		
Fe		
Mn		
Co		
Cr		
S		
P		
Total		

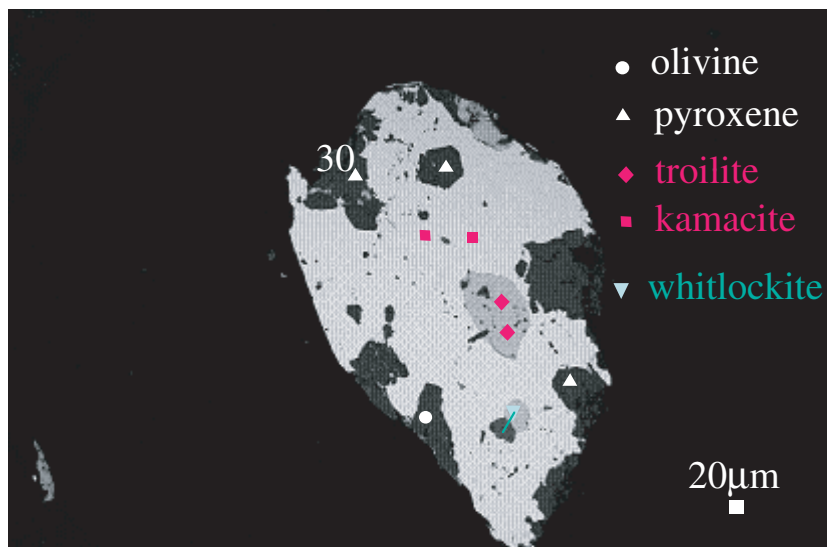


wt%	ol	low-Ca px	high-Ca px
SiO ₂	39.3	56.2	54.9
TiO ₂	0.0	0.1	0.2
Al ₂ O ₃	0.0	0.3	0.4
FeO	15.1	9.1	5.0
MnO	0.5	0.7	0.4
MgO	44.6	29.7	21.1
CaO	0.2	3.3	16.3
Na ₂ O	0.0	0.2	0.5
K ₂ O	0.0	0.0	0.0
Cr ₂ O ₃	0.0	0.6	0.7
NiO	0.0	0.0	0.0
P ₂ O ₅	0.2	0.0	0.1
SO ₃	0.0	0.0	0.0
total	100.0	100.1	99.6

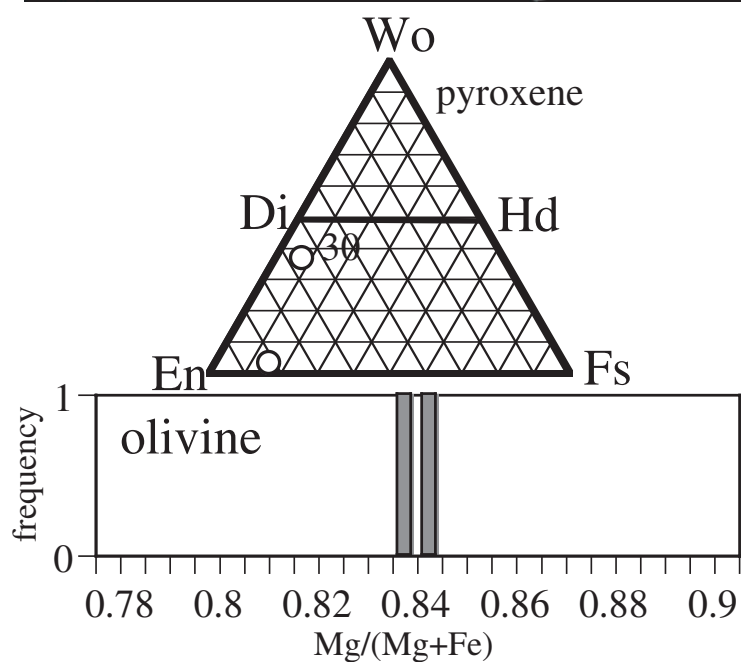
O: olivine
 Px: low-Ca pyroxene
 Pl: plagioclase
 Tr: troilite
 K: kamacite
 Ta: taenite



2BC8



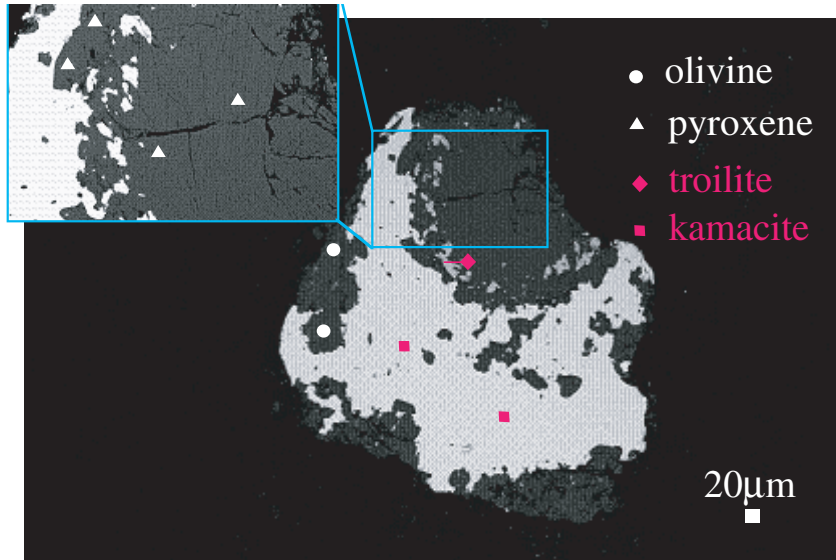
wt %	tr	kam
Ni	0.0	6.4
Fe	64.4	94.5
Mn	0.0	0.0
Co	0.0	0.4
Cr	0.0	0.0
S	36.3	0.0
P	0.0	0.0
Total	100.8	101.3



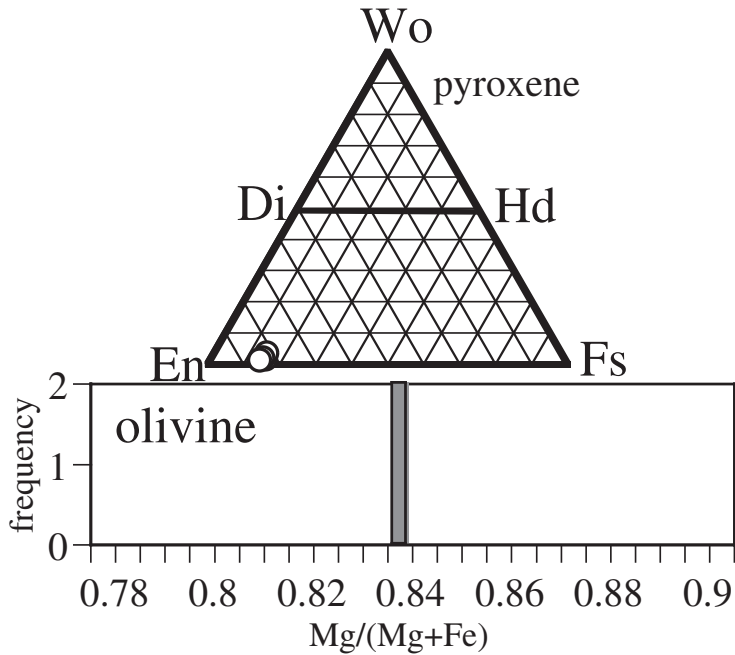
wt%	ol	low-Ca px	high-Ca px
SiO ₂	39.1	54.5	51.7
TiO ₂	0.1	0.1	0.9
Al ₂ O ₃	0.0	1.7	3.0
FeO	15.5	10.2	4.0
MnO	0.5	0.6	0.3
MgO	44.9	30.0	19.1
CaO	0.0	1.5	17.4
Na ₂ O	0.0	0.0	0.4
K ₂ O	0.0	0.0	0.0
Cr ₂ O ₃	0.1	0.8	0.7
NiO	0.0	0.0	0.0
P ₂ O ₅	0.0	0.0	0.0
SO ₃	0.0	0.0	0.0
total	100.3	99.6	98.6

No X-ray diffraction analysis was performed on this sample.

2BC9



wt %	tr	kam
Ni	0.1	6.2
Fe	59.6	94.4
Mn	0.0	0.0
Co	0.0	0.4
Cr	0.0	0.0
S	33.5	0.0
P	0.0	0.0
Total	93.3	101.0



wt%	ol	low-Ca px	high-Ca px
SiO ₂	39.4	56.7	
TiO ₂	0.0	0.1	
Al ₂ O ₃	0.0	0.3	
FeO	15.7	10.2	
MnO	0.5	0.6	
MgO	45.2	31.5	
CaO	0.0	0.8	
Na ₂ O	0.0	0.1	
K ₂ O	0.0	0.0	
Cr ₂ O ₃	0.0	0.1	
NiO	0.0	0.0	
P ₂ O ₅	0.0	0.0	
SO ₃	0.0	0.0	
total	100.9	100.4	

No X-ray diffraction analysis was performed on this sample.